QUANTIFYING THE HIERARCHICAL MESOSTRUCTURE OF FUSED DEPOSITION MODELED MATERIALS AND MEASURING THE EFFECT ON THE ELASTIC MECHANICAL RESPONSE

by

SVEN VOIGT

Submitted in partial fulfillment of the requirements

For the degree of Master of Science

Thesis Adviser: Dr. Jennifer Carter

Department of Materials Science and Engineering

CASE WESTERN RESERVE UNIVERSITY

January, 2018

Case Western Reserve University

We hereby approve the thesis[1] of

Sven Voigt

for the degree of

Master of Science

Dr. Jennifer Carter

Committee Chair, Adviser
Department of Materials Science and Engineering

Dr. James McGuffin-Cawley

Committee Member
Department of Materials Science and Engineering

Dr. Clare Rimnac

Committee Member
Department of Mechanical and Aerospace Engineering

Date of Defense   August 14, 2017

---

[1]We certify that written approval has been obtained for any proprietary material contained therein.

Table of Contents

List of Tables

List of Figures

Acknowledgements

My work is dedicated to all the people in my life you have helped me personally and professionally.

I would like to thank my parents for the many years of encouragement. It has been reassuring to know that you are there to support me in all situations and it has been a fundamental reason that I have been able to pursue my goals.

I would also like to thank Prof. McGuffin-Cawley for his help in planning my education, work, and research goals. I have appreciated your perspective on all issues and it has helped me to find my own interests.

Also, I am grateful to Prof. Carter for the commitment she made to help with my development as a researcher. Your dedication and input to the research, presentations, and publications was invaluable and contributed greatly to the quality of the work.

Other people I would like to thank include my friends for their compassion and support. Dr. Rimnac for her comments on the thesis, Dr. French for sharing his knowledge of data science, and everyone in AMMRC who helped with the mechanical testing.

Finally, I would like to acknowledge the collaborators at Youngstown State University for the manufacturing of the Ultem test specimens, and technical discussions during the course of the program.

Abstract

Quantifying the Hierarchical Mesostructure of Fused Deposition
Modeled Materials and Measuring the Effect on the Elastic Mechanical
Response

Abstract

by

SVEN VOIGT

0.1 Abstract

FDM specimens are created by varying the process variables defined in a CAD model.
The FDM mesostructure is defined from the CAD model and used to develop a volume
fraction model that predicts mass and stiffness. The mesostructure definition is simpli-
fied by considering the hierarchical structure that is an assembly of smaller structures.
A mesoscale model is developed that predicts the change in properties in relation to a
nominal mesostructure. A second homogenization model is developed for obtaining ef-
fective macroscale properties. The model is compared to experiments on macroscale
properties of FDM test specimens. Specimens are compressively loaded in three mutu-
ally orthogonal directions. The compression setup is redesigned to optimize digital im-
age correlation (DIC) measurements of local strain. In addition to elastic response, DIC
measurements were able to detect local plastic strain. Damage in FDM parts is shown
to be strongly related to loading conditions.

1   Introduction

Fused Deposition Modeling (FDM) is an additive manufacturing method that has become capable of directly producing tools to form sheet metal[2]. The advantage of this method is the ability to quickly and cost effectively produce low quantities of custom parts[3]. However, the deflection of the FDM tool remains a challenge in sheet metal forming due to missing information about the anisotropic mechanical properties. This project aims to advance the capabilities of FDM sheet metal forming by developing an intuitive method for designing FDM materials that predicts properties directly from a computer model of the final tool.

Designing the tools by FDM involves defining a custom computer aided design (CAD) model that is used to directly make final products using a 3D printer. Once the model is uploaded to the 3D printer, FDM sequentially builds parts one filament at a time. Each filament is deposited on a platform that is horizontal to the ground. Multiple filaments are deposited on a platform to form a layer. New layers are also composed of filaments and are deposited on top of previous layers. A nozzle that deposits the filaments moves vertically away from the platform in steps for each new layer. The upward direction of the printing process is also known as the build direction. The process is controlled by many variables: some are necessary for the process to function and others control

the mesostructure of the final parts. The variables that directly impact the mesostructure of the FDM parts also significantly impact the final mechanical properties, such as stiffness[4]. They also influence the speed and cost of parts produced by FDM. Since the mesostructural variables are inversely related to stiffness and also to cost, the cost of FDM parts increases with stiffness. This demonstrates that there are clear tradeoffs when designing a part for stiffness in a sheet metal forming application.

The final FDM part is a structure composed of discrete filaments. The structure at the width of a filament, about 500 μm, is inhomogeneous. Figure 1.1 shows an assembly of filaments that represents one possible mesostructure of an FDM material. At the mesoscale, the structure clearly reveals discrete steps in the structure. However, at a greater length-scale, the properties of an FDM part resemble that of a continuum body and effective macroscopic properties could be characterized.

Characterizing every possible mesostructural combination of filaments is exhaustive and risks becoming outdated with advancements in FDM technology. Therefore, the approaches that have been developed to describe the mechanical behavior of FDM materials have been based in mechanics of materials. The mechanics of materials approaches try to relate the properties of the filament to the effective properties of the FDM part and thereby be applicable to any possible mesostructure. The first and simplest are rule of mixture approaches that estimate the reduction in stiffness from a volume fraction of longitudinal voids present in the structure[5]. Additionally, since the FDM parts are anisotropic, the effective modulus will change depending on the direction it is measured in. Approaches that predict stiffness in a particular direction apply a rotation to the stiffness tensor of FDM materials and calculate an effective elastic modulus[4,6]. Both the rule of mixtures approach and the rotation approach have been successful, but they
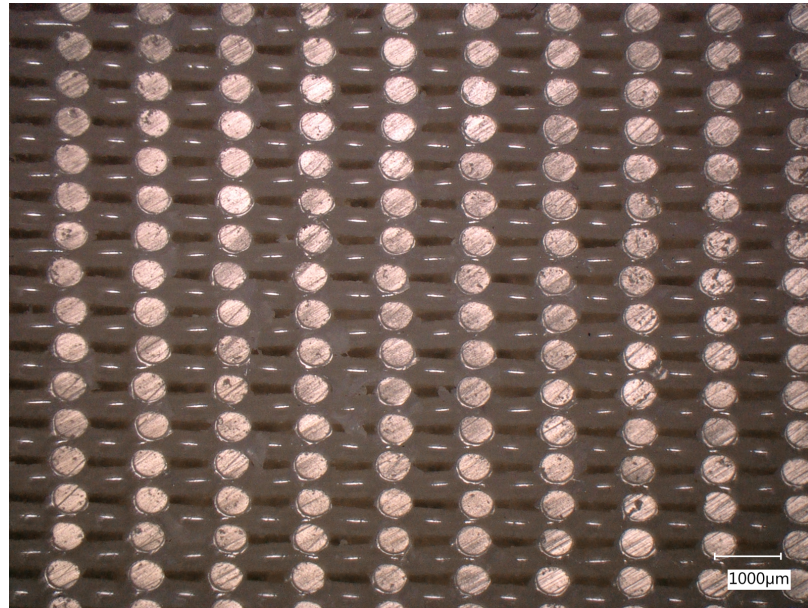
Figure 1.1. This image was taken using a Keyence VHX 5000 microscope. It shows the inhomogeneity of FDM structures. The filaments are shown to form a three-dimensional structure. Half the filaments are coming out of the page and the other half run horizontal. The filaments are approximately 500 μm in diameter and gaps exist between parallel fibers. When looking at the stack of fibers in the vertical direction, it can be seen that the filaments do not stack perfectly.

are simplistic and only consider unidirectional FDM parts. Two additional process variables are commonly used and significantly change the mesostructure of the FDM materials. Therefore, the real FDM part is more complex than considered by simple models and additional approaches need to be developed to predict an effective stiffness for an arbitrary mesostructure.

Finding effective properties for a macroscopic part from known properties at a smaller scale is known as homogenization. The rule of mixtures model is a type of homogenization that considers only proportions and not the effect of geometric position of sub-elements. A model that combines geometric positions of filaments and material properties to directly calculate macroscopic properties from the mesostructure is developed

in[7]. The algorithmic definition of the mesostructure defines the position of the filaments but makes the assumption that the geometry transverse to the fibers is equivalent in two directions. This also assumes equivalent properties in those directions. Although the model has the capacity to solve for a stiffness tensor, the model is experimentally validated by a single modulus measurement in a single direction. However, this model does demonstrate the possible effect of the mesostructure on the macroscopic properties.

Additionally, the present models represent the tensile behavior, where the FDM materials do not strain extensively before failure, where tensile failure is defined as the complete separation of a tensile test specimen[8]. However, the compressive behavior exhibits longer strains to failure, where compressive failure is defined as the formation of a crack[9]. The type of crack that forms is dependent on the mesostructure and the orientation of the test specimen. In[9], the cracks occurred along the axis of compression or at 45° to the same axis. These cracks were attributed to local effects that were observed on a macro length-scale.

In this project, the mesostructure of FDM parts is defined directly from the CAD model. Important characterization steps from previous research such as the volume fraction are given a digital definition. The geometry from the CAD model is further broken into an assembly of simple components, to simplify the definition of the mesostructure. The CAD model properties and geometry, which were defined by the designer in a CAD model, are then used to model the macroscopic elastic behavior for complex real FDM materials. Since sheet metal forming tools are commonly designed using the finite element method (FEM)[10], treating FDM materials as assemblies of shapes would allow for an intuitive construction of FDM tools for sheet metal forming without the need for

the designer to model the mesostructure. Additionally, defining the FDM part in terms of the CAD model, reduces the amount of characterization needed to qualitatively predict the mechanical properties of the final part. In sheet metal forming, this would first reduce the cost of guessing at the capabilities of an FDM tool. Then, it would allow the discovery of new applications for well-characterized FDM tools.

To validate the models, a design of experiments are developed. The macroscopic FDM specimens are deformed to failure under compression and the strain patterns are observed using digital image correlation (DIC), which tracks a speckle pattern and measures strain at multiple locations across a surface. The macroscopic elastic behavior is measured by using an average measurement of the DIC strain measurements. To compare the specimens, a method for calculating a tangent modulus is defined. The specimens are constructed to assess the consistency of a measured tangent modulus and also to assess the effect of a breadth of process variables. Understanding the consistency is necessary in sheet metal forming to understanding the predictability of FDM material properties. Measuring properties across a breadth of process variables gives insight into the effects of the variables and can be used to validate a predictive model. The experimental results are compared to the model and used to describe the real behavior of FDM materials.

The DIC strain measurements are also precise enough to capture mesoscale behavior and the inhomogeneity of strain distribution at a local scale. During the compression tests, the strain in FDM specimens accumulates locally to cause failure. The reasons for this are attributed to traction forces introduced by frictional constraints as well as the segmented mesostructure. These reasons are assessed using FEM modeling and control

compression tests to provide insight into the failure behavior of FDM materials. This information is valuable because it can identify the susceptibility of FDM materials to local cyclic plastic deformation, even if the macroscopic part is loaded elastically. Since sheet metal forming tools are loaded cyclically, local plastic deformation would cause a loss of dimensional accuracy.

Predicting Effective Properties

Known Nominal Properties

Calculated Component Properties

Component Properties Transformed Into Part Coordinate System

Homogenizing For Effective FDM Material Properties
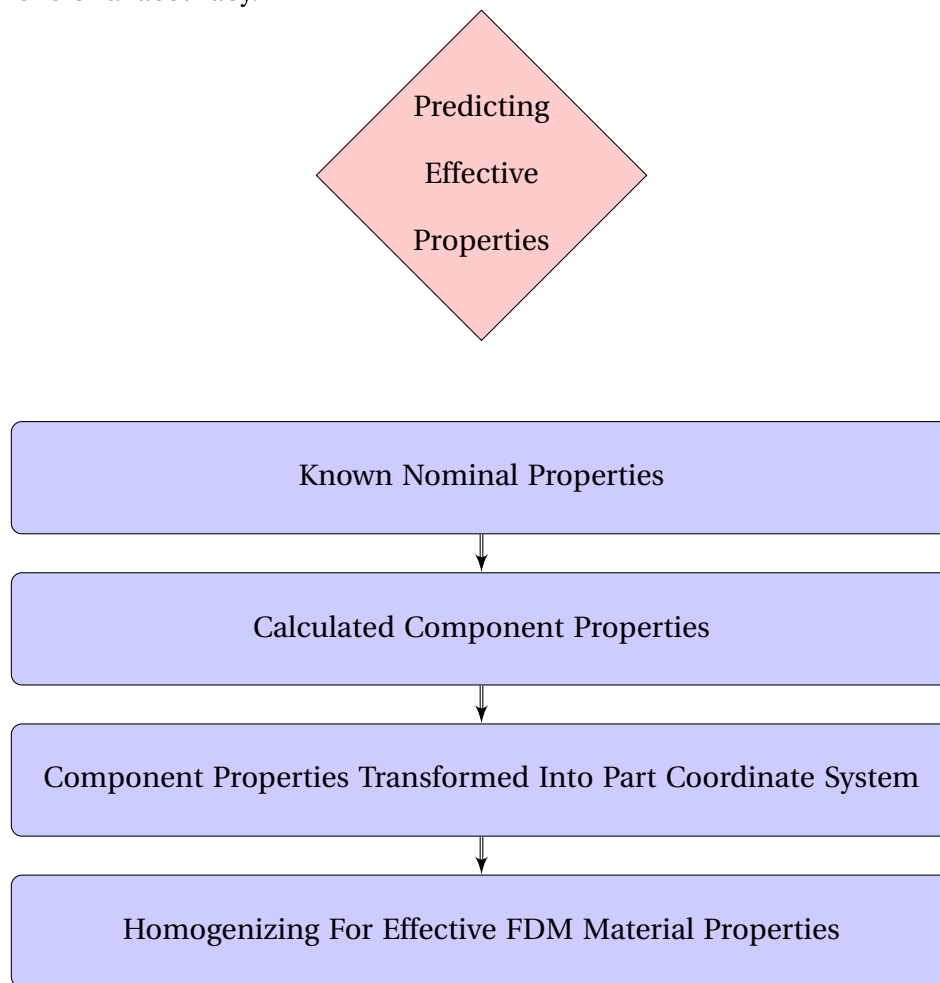
2 Background

2.1 Sheet Metal Forming

Sheet metal is metal that has been processed to be geometrically thin and flat. Sheet blanks are sheet metal pieces that haven't been formed by another process. Sheet metal forming is the process of plastically deforming a sheet blank into a geometrically complex part. Tools contain the geometric information that is passed to the sheet blank. Reliable sheet metal forming processes produce parts where the sheet blank resists failure by fracture or wrinkling and meets rigid dimensional requirements. This depends on quantitative design where the objectives are: predicting the flow stress, measuring the formability limits, and designing the tooling to meet the force and energy requirements of the forming process. Quantitative design is achieved by modeling the sheet metal forming process using Finite Element Method (FEM) techniques[10]. FEM analysis of traditional sheet metal forming assumes the tool to be rigid. When the tool is assumed to be rigid, the only values that need to be known for solving a simulation are the sheet material properties and the tool/sheet interface conditions[11].

A specific type of sheet metal forming is the deep drawing process, where the tools are a die, blank holder, and punch. The die contains the geometric information and also extends to hold the sheet blank. The blank holder is placed above the extensions of the

die and applies a pressure to the blank. The frictional forces are increased by the blank holder and serve to hold the the blank sheet in place. The punch is the moving part that forces the blank sheet into the die[10].

Rubber pad forming is a specific type of deep drawing where the punch is not a rigid tool, but a rubber pad. The rubber pad is filled with a pressurized fluid during this process. It exerts a constant pressure on the sheet blank until the expansion is restricted by the die. The rubber pad also meets the die at the edges. This results in frictional forces that hold the blank sheet in place; a job that is performed by the blank holder in typical deep drawing. An advantage of the rubber pad forming process is that the sheet blank is uniformly strained until it makes contact with the die. Rubber pad forming is a slow strain rate process that is most useful for low-production-volume[10].

Linear stretchforming is another specific type of deep drawing where the tools include clamps and a form block, which takes the place of the die. The clamps hold onto a sheet blank and pull it over the form block.[10].
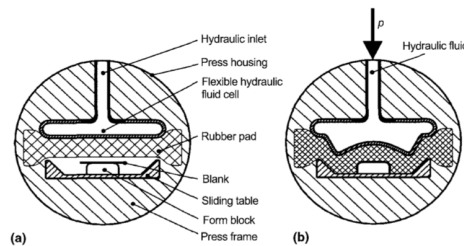
Fig. 2.18 Fluid bladder and diaphragm process: (a) before; (b) during forming. Source: Ref 2.8

Figure 2.1. Rubber Pad Forming is a specific type of sheet metal forming. A bladder behind a rubber pad is pressurized and pushes the rubber pad into the sheet metal and over a die. This process is typically used in low-production-volume processes[10].
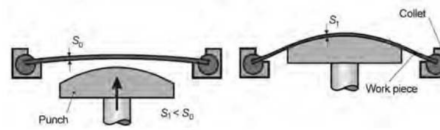
Fig. 2.23 Linear stretch forming. Source: Ref 2.4

Figure 2.2. Linear Stretch Forming is a specific type of sheet metal forming. Clamps are used to pull sheet metal over a form block[10].

2.2 Fused Deposition Modeled Tools

Tool design is one of the three crucial steps required to design a successful forming process. The tools need to support the required forces and energy of the forming process. The important variables in tool design include: geometry, surface properties, stiffness, and other responses to mechanical and thermal conditions[10].

Traditional tools are designed to be durable, however, they are long-term solutions and expensive. For low production volumes, the costs of traditional tooling are too high to implement. An accelerated development process aims to quickly produce prototype parts including sheet metal parts. This spurred the development of new types of tools that could cost effectively produce low volume prototypes. Some of these designs include configurable tools that consist of movable elements or multiple laser-cut sheets clamped together. Now, Rapid Prototyping Tools are being employed to quickly create sheet forming tools[12]. One particular use of rapid prototyping is the production of molds. Sand mold additive manufacturing can be used to make low melting temperature metal tools[12]. Fused deposition modeling (FDM) is an additive manufacturing method that is commonly used to design products. It also can be used to make molds. This includes silicone molds, which are used to cast epoxy[13].

Over time, the properties of FDM parts have evolved such that they could be directly used as tools in the forming process. Stratasys, Minnesota, USA, is a provider of 3D

printers, which are machines used to build FDM parts. They claim that FDM tools are capable and economical in hydroforming processes such as rubber pad forming[3]. Rubber pad forming is primarily used for low-production-volume products and occurs at low strain rates. This means that the requirements for tools are more forgiving and additively manufactured tools are a more attractive option than expensive traditional tools for specific low-batch products. Sheet metal forming to produce low-batch products is even quicker and cheaper than computer numerical control (CNC) manufactured parts according to Stratasys[3]. No comparison is made to other rapid prototyping tools.

The desire to manufacture custom sheet metal parts is apparent for the Maturing Additive Manufacturing for Low-Cost Sustainability program. The sustainability program aims to service ageing machines or vehicles by providing replacement parts. The required parts are important even if the number required is low. Therefore, a low-cost solution for low volumes is desirable. Also, the parts that are being replaced were hand designed and exact dimensions deviate from the blueprints. New technology gives the ability to scan these parts with a digital camera and directly produce a 3D CAD file. This technology coupled with FDM translates the exact geometric dimensions of the old part to the newly produced sheet metal part.

Although there are some benefits to using FDM tools, understanding their performance has been difficult. For one, rapidly produced tools do not have the same durability as traditional tools[10]. Durgun studied a sheet metal forming process where the sheet metal was formed between a top and bottom die, produced by FDM[2]. The study found that FDM tools are only useful for a few iterations, around 100 for the particular operation. Corners in the dies were found to be the most worn.

Another reason FDM tools are difficult to employ is that they are compliant and deform during the sheet metal forming process. In addition to wear, Durgun also reported that FDM tools deform significantly during sheet metal pressing. Two steels were included in the study, referred to as harder and softer, and it was found that only the more malleable steel could be formed to match the desired final shape. The process using the so-called harder steel deformed the tool to a point that the final shape of the sheet metal was found to be unsatisfactory[2].

This highlights the importance of understanding the characteristics of FDM tools. First, is an FDM tool capable of forming a certain material into a certain geometry. Secondly, what are the dimensions of the final formed part if the tool deflects during forming. This requires a robust approach for quantitative design.

2.3 The Fused Deposition Modeling Process

Fused Deposition Modeling (FDM) is an additive manufacturing process that builds parts from thermoplastic filaments. It belongs to a broader family of processes called solid freeform fabrication (SFF) and was developed by Stratasys, Inc. In FDM, filaments are extruded through a nozzle to build layers. Each of these filaments thermally welds with the filaments that it comes in contact with, including filaments in other layers[14,15]. This is a careful balancing process: the filament needs to be fluid enough to be extruded through a nozzle and weld to other filaments, but still viscous enough so that it maintains its shape. The filaments are deposited until the layer is finished. The nozzle then moves up the build direction and starts a new layer.

The FDM part is built in an environment that contains a platform and a robotic apparatus for controlling the position of the nozzle. The boundaries of where the nozzle can move are confined, and thus where the filaments can be placed is also confined. This environment matches a digital replica that can be manipulated by a designer. Software can be used to create a computer model of a final part in this virtual representation of the 3D printer. Then, the toolpaths are defined by a set of process variables. The toolpaths are instructions for the movement of the nozzle and final placement of filaments, which have an effect on the mesostructure and the final properties as discussed later. For Stratasys, the platform on which the FDM parts are built defines the bottom of the environment and is designated as the X-Y plane[15]. The platform is horizontal to the ground. The first layer of the FDM part is deposited on the platform and each subsequent layer is deposited on the layer beneath it. Therefore, each layer of the FDM part is parallel to the X-Y plane. The nozzle moves moves vertically away from the platform in steps for each new layer. The upward direction of the printing process is also known as the build direction and is defined as Z in the coordinate system[15].

During the printing process, the 3D printer tries to match the instructions it was given as closely as possible[14]. The filaments are extruded along the toolpaths on top of other filaments. This introduces a unique requirement that the filaments be both fluid and viscous. Fluidness is required for extrusion and the ability to fuse with other filaments. Viscousness is required so that the filament maintains its own shape and can support other filaments. This combination of properties can be achieved with only a few materials; Stratasys and this project use amorphous thermoplastics, but ceramic pastes may also work in other applications. Additionally, extrusion introduces alignment of the

polymer chains and transversely isotropic properties in the filament. The viscous filament also fuses to adjacent filaments and forms a fusion zone. Depending on the time and heat added, the properties and size of the fusion zone change[6,16]. In this fashion, additional property anisotropy is introduced by many fusion zones that occur where filaments are touching.

The extrusion temperature and cooling rate have a significant effect on the properties of the fusion zone and bonding between filaments and layers. The cooling rate is determined by the printing environment. For cheaper FDM printers such as maker-bot, the environment is unenclosed and thus at room temperature. More expensive models like the Fortus machines from Stratasys have an envelope that can maintain a higher temperature. The properties of the bond have been modeled in several research projects[6,16–19].

Thomas and Rodríguez used an analytical model to demonstrate that a slower cooling rate promotes stronger bonding[16]. Their model was based on a 2D rectangular representation of a filament in a stack of other rectangles. Rodríguez experimentally
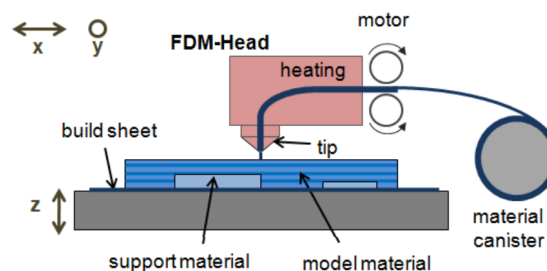
Figure 2.3. Fused Deposition Modeling Process: The figure shows a simple 3D printer. The nozzle is extruding a filament onto a platform. The part is built one layer at a time. Once the nozzle has completed a layer, it moves up in the Z direction to deposit a new layer[9].

demonstrated the optimal bonding strength for the unidirectional FDM part was obtained using a specific combination of extrusion temperature and envelope temperature[17]. Although it is true that the fusion zone properties are improved with additional polymer chain diffusion at high temperatures, Graybill showed that there is a limit. In particular, annealing an FDM part to improve diffusion between filaments detrimentally effects the properties due to thermal degradation[18]. Costa et al. expanded on the model proposed by Thomas and Rodríguez to 3D cylindrical filaments and accounted for radiation[19]. They predicted heat over time at each point in the model and the effect on the adhesion between filaments. The model was validated by experiment.

Huang et al. described the formation of the bond as the coalescence of two circular cross sections of the filaments[6]. For polymers, this process is driven by the diffusion of the polymer chains between the two filaments. The process initiates when the polymer chains begin to diffuse and then bond. During this process the polymer chains randomize in the bond[6].
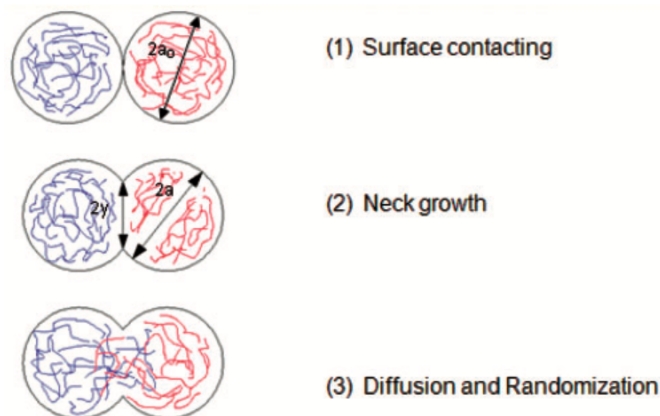
Figure 2.4. Coalescence of Filaments: The fusion process during FDM develops a bond between filaments by polymer chain diffusion and randomization.[6]

2.4 Mesostructure of Fused Deposition Modeled Parts

The result of producing a part from filaments is local structural inhomogeneity. Voids and fusions zones are present between filaments as shown in figure 2.5. This structure occurs at a smaller length than the geometric definition of final part. Therefore, it is referred to as the mesostructure.

Already discussed is the influence of the temperature and cooling rates on the mesostructure. However, the designer does not have easy control over these parameters. The designer controls the production of an FDM part from a Computer Aided Design (CAD) model and has direct control over the toolpaths that will be used to construct the final
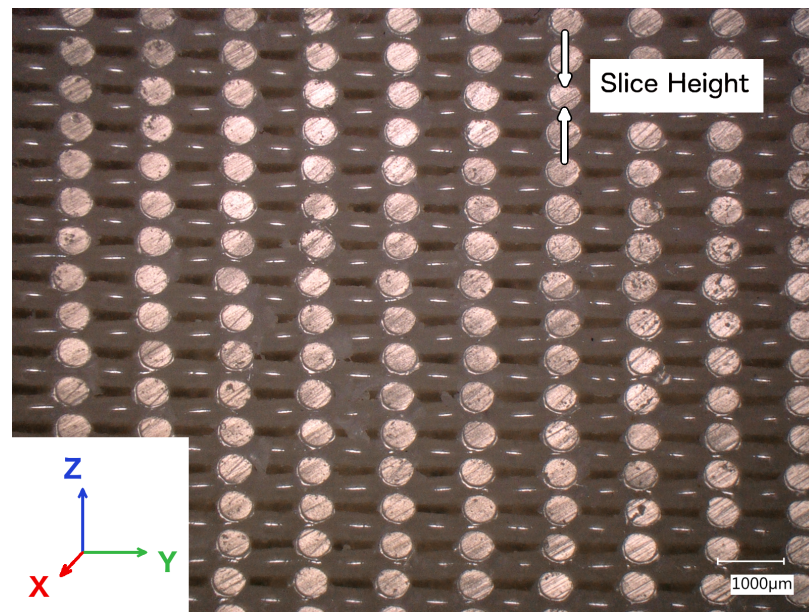
Figure 2.5. Mesostructure Micrograph with Slice Height: Real mesostructure of an FDM part printed with an air gap of $597\mu m$ and raster angle of $90°$. This image was taken using a Keyence VHX 5000 microscope. The coordinate system tells us that this part was cut vertically and the mesostructure is viewed from the side. This allows seeing the stacking between many different layers. The slice height is the parameter that controls how far apart these layers are stacked in the vertical direction.

part. Toolpaths are virtual instructions for the 3D printer that dictate the placement of filaments and the path the extrusion nozzle will travel. The mesostructure is then a function of the toolpaths[7]. The toolpaths can be altered by the designer using several process variables. First, the CAD model, represented in the STL file format, is sliced according to the slice height variable, given as a length. Each slice and therefore layer, is equal in thickness to the slice height. The slices represent each layer that will be built and thus exist in a plane parallel to X-Y plane at a distance from the platform, Z. The nozzle will always move along Z in steps of the slice height when starting a new layer[15]. The slice height is shown in figure 2.5.

Each layer in the composed of two parts: the contour and the fill[9]. The contour toolpath follows the outline of a layer and can be any shape and thickness. Several toolpaths can follow the contour starting at the furthest edge of a layer and then moving inwards. The number of toolpaths per contour is defined by a process variable called number of contours. The fill is commonly produced using the raster fill, where each toolpath in the fill is parallel to all other toolpaths within any distinct layer[9].

The in-plane mesostructure is controlled by the air gap process variable, which controls the width of the longitudinal voids present between filaments[9]. The air gap is defined as a length. Recall that the toolpaths, and thus filaments, are all aligned parallel to each other in the raster fill. The actual toolpaths are spaced apart by a distance equal to the sum of the air gap and the filament width, which is also a variable than can be chosen by the designer.

From one layer to another, the mesostructure is rotated around the Z axis by a variable called the raster angle, which is given in degrees. The raster angle controls the orientation of a layer to the layer beneath it. This keeps going for any number of layers. For

example, if a raster angle of 45° is chosen, any arbitrary layer will be rotated 45° to the layer beneath it, and 90° to two layers beneath it. The air gap, raster angle, contour, and fill are shown in figure 3.1.

2.4.1 Hierarchical Structure

FDM is an additive process that builds final parts layer by layer. The layers are also built sequentially using filaments. Therefore, each structure is always dependent on the structure at a smaller length scale. However, this structure is often repetitive and an arbitrary volume is representative of the complete structure[4–6,8]. The repetitiveness is shown in figure 2.5. Real structures are often discontinuous and non-repetitive. In these cases, the location of a filament is unique and the structure of the part can be described
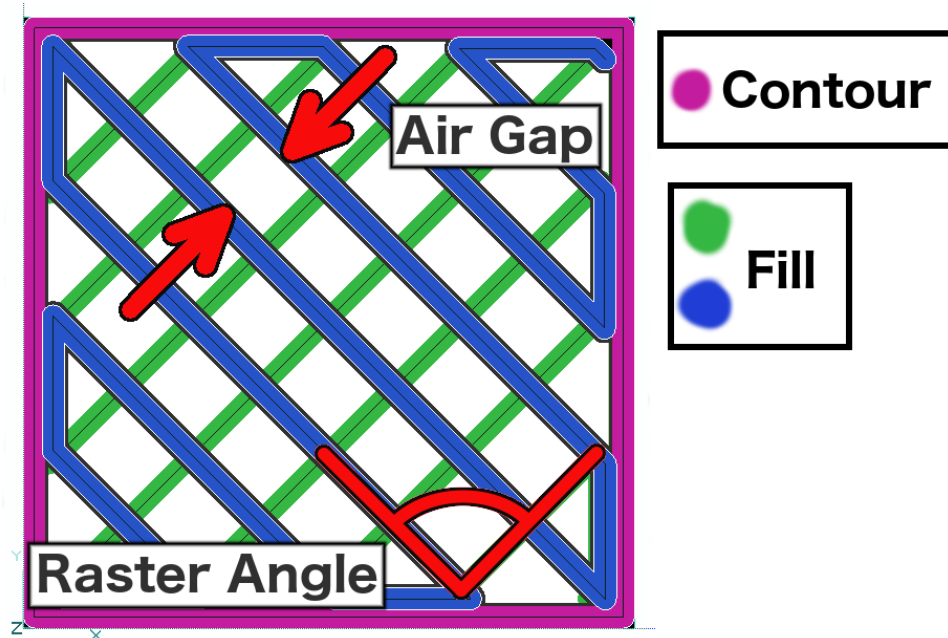
Figure 2.6. 2D Structure of an FDM Layer: In the plane of a layer, the air gap determines the spacing between rasters. The raster angle determines the angle the filaments in this layer make with the layer beneath it.

by the location of all filaments[7]. Additionally, a single part can have multiple different mesostructures. As of now, the temperatures cannot be varied during the build. However, the structural variables (air gap, raster angle, filaments per toolpath) can be varied throughout the part[20].

2.5 Background of the Finite Element Method

The quantitative design of sheet metal forming processes is achieved with the finite element method (FEM)[10]. The FEM is a way of solving differential equations using piecewise linear functions. In the case of sheet metal forming it is used to solve the governing equations of virtual work. These governing equation relate displacements, forces, stresses, and strains to each other. Each of these play a significant role in the sheet metal forming process. The FEM can be applied to arbitrary spatial domains, such as the complex tool designs encountered in sheet metal forming. The domain is sectioned into small simple geometries such as triangles and squares in 2 dimensions and tetrahedra and hexahedra in 3 dimensions. The vertices of these geometries are defined as the nodes and the discrete values of the governing equations are solved at these nodes. The solution can therefore be viewed as a field, with discrete values at each of the nodes[21].

In order to solve the sheet metal forming model using FEM, some real world values are needed such as the already-discussed geometries of the tools. Additionally, boundary conditions need to be known. These include the pressure being applied to the tool by the sheet metal, the locations the pressure is applied, and time the sheet metal makes contact with the tool. In rubber pad forming, the pressure is the pressure applied to the bladder behind the rubber pad and is the driving force that determines the locations the

pressure is applied. Lastly, material properties need to be known. These include physical properties such as density. Also necessary to know are the stiffness and/or compliance of the materials. This includes both the sheet metal and the tool. However, in FEM modeling of traditional sheet metal forming, the tool is assumed to be rigid. Therefore, the tool does not need to be characterized. The only remaining material properties that need to be defined for the model include the interface conditions between the tool and the sheet metal, such as a coefficient of friction[11]. However, tools are not always rigid[22]. Flexible tools require additional information to allow simulation of the sheet metal forming process. Cai et al. worked on configurable tools that were covered with a rubber pad. The material properties relating to the elasticity of the tool therefore had to be incorporated into the FEM model[22]. Quantitative design of FDM forming processes will also require characterization of the mechanical behavior of FDM tools.

2.6 Background of Mechanics

Mechanical theories that describe the behavior of materials can be used broadly to achieve quantitative design and test materials. Mechanics deals with the mechanical behavior of a material in response to a type of loading such as force, stress, and strain. The reference frame of classical mechanics is a Euclidean space, where the location of all points is a set of three unique numbers. The definition of vectors requires a coordinate system such as the Cartesian Coordinate System. This coordinate system consists of three mutually orthogonal axes defined by unit vectors of the same length. The mechanics naming convention for the axes is e_i. In mechanics, the Newtonian Coordinate System
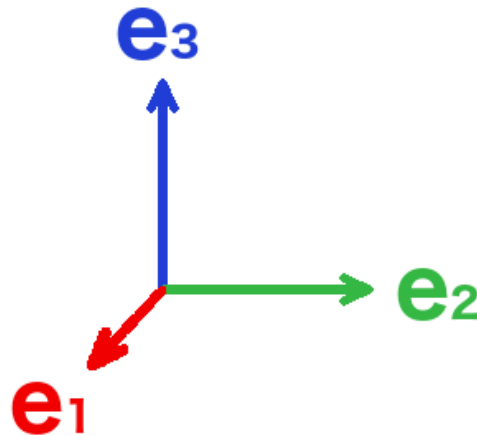
Figure 2.7. A positive cartesian coordinate system. All axes are perpen-
dicular to each other and have an orientation. The orientations as shown
are known as the positive cartesian coordinates.

is used, which is a type of Cartesian Coordinate System that guarantees Newton's laws

of motions are true[23].

$$e = \{e_1, e_2, e_3\}$$

2.6.1 Deformation

The bodies being deformed in mechanics are idealized as continuum bodies. A contin-

uum body is a physical object which can be divided infinite times and remain homo-

geneous, i.e. all subdivisions of any part of a continuum body have the same physical

properties. Deformation describes the motion of particles from a reference frame to a

deformed frame. A displacement, u, describes the change in position of a particle. A

displacement from a position x to y is mapped by the deformation gradient tensor F[24].
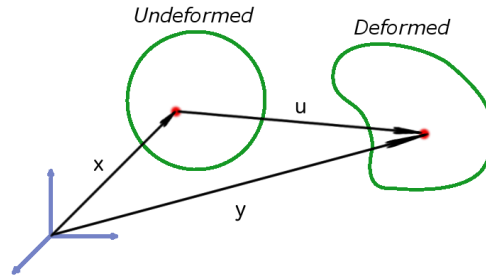
Figure 2.8. Deformation Mapping: In the undeformed body, the location of the red point can be defined with the vector x. After a deformation, the point exists in the deformed body. The vector u describes the movement of the point and y is the new location of the point in the deformed body.

$$x = \{x_1, x_2, x_3\}$$

$$y = \{y_1, y_2, y_3\}$$

$$y = x + u(x, t) \tag{2.1}$$

$$dx = F\, dx_0 \tag{2.2}$$

$$F = \nabla u + I \tag{2.3}$$

$$\nabla u = \frac{\delta u}{\delta x} \tag{2.4}$$

2.6.1.1 Strain. If this position of vectors is described in reference to the undeformed positions (i.e. $u(x, t)$), then this is referred to as a Lagrangian description of motion. Often, this is the most used definition for deformations in materials. The Lagrangian strain tensor, E, is also defined in terms of the undeformed positions[24].

$$E = \frac{1}{2}\left(F^T \ddot{F} - I\right) \tag{2.5}$$

$$E = \frac{1}{2}\left(\nabla u + \nabla u^T + \nabla u^T \nabla u\right) \tag{2.6}$$

2.6.2 Kinetics

Tractions are forces, P, per unit of area, A, that act on the surface of a body. They can be decomposed into 3 components. The stress is defined in terms of all possible tractions in a cartesian coordinate system as shown in figure 2.9.

$$t = \lim_{A \to 0} \frac{dP}{dA}$$

$$\sigma = e \otimes t \tag{2.7}$$

Additionally, the stress tensor can be proven to be symmetric by moment equilibrium. Therefore, the stress tensor only has six unique values[24].

$$\sigma = \sigma^T$$

2.6.3 Elasticity

Hooke's law identifies the proportionality between forces and deformations[23]. It states that the force, F, is proportional to the displacement, x, by a spring constant, k.

3D Stress State   Plane Stress
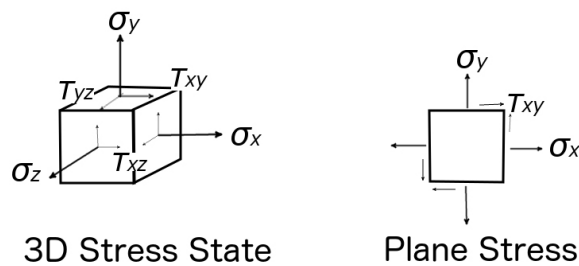
Figure 2.9. Stress State

$$F = kx$$

Another term for the spring constant is stiffness. They are convenient since they can be added in series and parallel by the simple equations 2.8 and 2.9[23].

$$k_{parallel} = \sum_{i=1}^{n} k_i \qquad (2.8)$$

$$\frac{1}{k_{series}} = \sum_{i=1}^{n} \frac{1}{k_i} \qquad (2.9)$$

They are also useful because they can be related to the geometry and material properties of a beam[25]. In equation 2.10 the material property elastic modulus, E, is related to stiffness, k. A force acts normal to an area, A, of the component. The length, L, of the component is measured in the direction of the applied load as shown in figure 2.10.

$$k = \frac{A E}{L} \qquad (2.10)$$
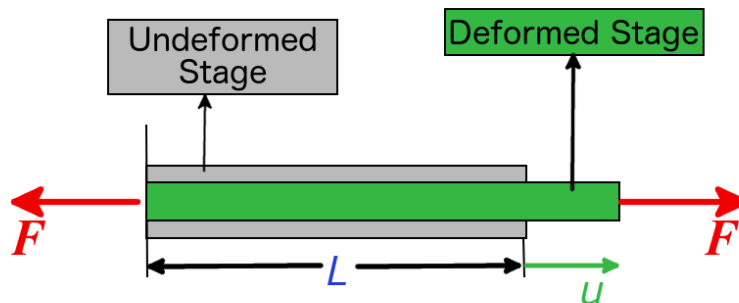
Figure 2.10. Uniaxial loading of a material element

2.6.4 Generalized Hooke's Law

Hooke's Law describes linearly elastic behavior in a single dimension. For generalized linear behavior in three dimensions, the stresses and strains can be related by a fourth order tensor. When the strains, ϵ, are related to stresses, σ, the tensor is called the stiffness tensor, C. However, when the stresses are related to strains, the tensor is called the compliance tensor, S. These tensors are inverse to each other.

$$\sigma_{ij} = C_{ijkl}\epsilon_{kl}$$

$$\epsilon_{kl} = S_{klij}\sigma_{ij}$$

$$C^{-1} = S$$

Due to the symmetry in both the stress and strain tensors, the above equations can be converted to a simpler representation using Voigt notation. The stresses and strains become vectors of length six and the compliance and stiffness tensors become a second order tensor.

$$
\begin{pmatrix} \epsilon_1 \\ \epsilon_2 \\ \epsilon_3 \\ \epsilon_4 \\ \epsilon_5 \\ \epsilon_6 \end{pmatrix}
=
\begin{bmatrix}
S_{11} & S_{12} & S_{13} & S_{14} & S_{15} & S_{16} \\
S_{21} & S_{22} & S_{23} & S_{24} & S_{25} & S_{26} \\
S_{31} & S_{32} & S_{33} & S_{34} & S_{35} & S_{36} \\
S_{41} & S_{42} & S_{43} & S_{44} & S_{45} & S_{46} \\
S_{51} & S_{52} & S_{53} & S_{54} & S_{55} & S_{56} \\
S_{61} & S_{62} & S_{63} & S_{64} & S_{65} & S_{66}
\end{bmatrix}
\begin{pmatrix} \sigma_1 \\ \sigma_2 \\ \sigma_3 \\ \sigma_4 \\ \sigma_5 \\ \sigma_6 \end{pmatrix}
$$

When symmetry is added, the number of independent constants is reduced. For orthotropic materials the stiffness tensor can be defined with three material constants:

elastic modulus, E, shear modulus, G, and poisson's ratio, v. The elastic modulus is unique in each of the three unique directions of an orthotropic material. The shear modulus and poisson's ratio are unique for each combination of the unique orthotropic directions. Due to symmetry in the orthotropic material, only the combinations are unique and not the permutations. Then, the compliance tensor is defined with nine unique material constants: $E_1, E_2, E_3, v_{12}, v_{13}, v_{23}, G_{12}, G_{13}, G_{23}$. The full form is as follows:

$$
\begin{pmatrix} \epsilon_{11} \\ \epsilon_{22} \\ \epsilon_{33} \\ 2\gamma_{23} \\ 2\gamma_{13} \\ 2\gamma_{12} \end{pmatrix} = \begin{bmatrix} \frac{1}{E_1} & \frac{-v_{12}}{E_2} & \frac{-v_{13}}{E_3} & 0 & 0 & 0 \\ \frac{-v_{12}}{E_1} & \frac{1}{E_2} & \frac{-v_{23}}{E_3} & 0 & 0 & 0 \\ \frac{-v_13}{E_1} & \frac{-v_{23}}{E_2} & \frac{1}{E_3} & 0 & 0 & 0 \\ 0 & 0 & 0 & \frac{1}{G_{23}} & 0 & 0 \\ 0 & 0 & 0 & 0 & \frac{1}{G_{31}} & 0 \\ 0 & 0 & 0 & 0 & 0 & \frac{1}{G_{12}} \end{bmatrix} \begin{pmatrix} \sigma_{11} \\ \sigma_{22} \\ \sigma_{33} \\ \sigma_{23} \\ \sigma_{13} \\ \sigma_{12} \end{pmatrix} \tag{2.11}
$$

2.6.5 Rotations

2.6.5.1 Rotation Tensor. In the cartesian coordinate system, rotation about an axis can be represented as a tensor transformation of coordinates. A rotation about the Z axis can be represented by the rotation matrix, R.

$$
R_z(\theta) = \begin{bmatrix} \cos\theta & -\sin\theta & 0 \\ \sin\theta & \cos\theta & 0 \\ 0 & 0 & 1 \end{bmatrix}
$$

When this rotation is applied to the compliance tensor it results in equation 2.12. The new compliance tensor can be calculated using equation 2.13.

$$
T_z(\theta) =
\begin{bmatrix}
\cos^2\theta & \sin^2\theta & 1 & 0 & 0 & 2\sin\theta\cos\theta \\
\sin^2\theta & \cos^2\theta & 1 & 0 & 0 & -2\sin\theta\cos\theta \\
1 & 1 & 1 & 0 & 0 & 0 \\
0 & 0 & 0 & 1 & 0 & 0 \\
0 & 0 & 0 & 0 & 1 & 0 \\
-\sin\theta\cos\theta & \sin\theta\cos\theta & 0 & 0 & 0 & (\cos^2\theta - \sin^2\theta)
\end{bmatrix}
\tag{2.12}
$$

$$
C^* = T_z(\theta)C(\theta) \tag{2.13}
$$

2.7 Constitutive Equations

2.7.1 Constitutive Rotation Model

For the rotation of an orthotropic material the effective modulus in any direction can be calculated using equation 2.14. Where S is the compliance tensor and l_{i1}, l_{j2}, l_{k3} are the direction cosines for direction $\{ijk\}$.

$$
\frac{1}{E_{ijk}} = S_{11} - 2(S_{11} - S_{12} - \frac{1}{2}S_{44})(l_{i1}^2 l_{j2}^2 + l_{j2}^2 l_{k3}^2 + l_{i1}^2 l_{k3}^2) \tag{2.14}
$$

The previous equation requires knowledge of the shear properties. However, Huang et al. used the isotropic properties of a filament and used the coalescence to develop a model for effective modulus for a single layer of an FDM part[6]. The coalescence, C, represents the fused area of contact between two filaments. The coalescence is the ratio of the radius of the neck formed between two filaments, y, and the radius of the edge of a filament as shown in figure 2.4.

$$Coalescence = \frac{y}{a}$$

Then, the effective properties in the x-y plane are a function of the bulk material properties, the geometry imposed by the FDM process, and the direction. The constitutive relations calculate an effective modulus, E_α, and shear modulus, G_α, for any loading direction α[6] due to the anisotropy of the geometry as shown in 2.11. However, calculating an effective modulus requires only the knowledge of the isotropic properties of a filament and the shape parameters. Therefore, this is a useful method of relating bulk polymer properties to the properties of a unidirectional FDM part at an orientation.

Alternatively, the same effective moduli from a rotation could be obtained experimentally. El-Gizawy et al. characterized a FDM specimens along the axis and at several angles to get effective moduli in all orientations. A full orthotropic stiffness matrix was developed this way for one particular mesostructure of an FDM part[26].
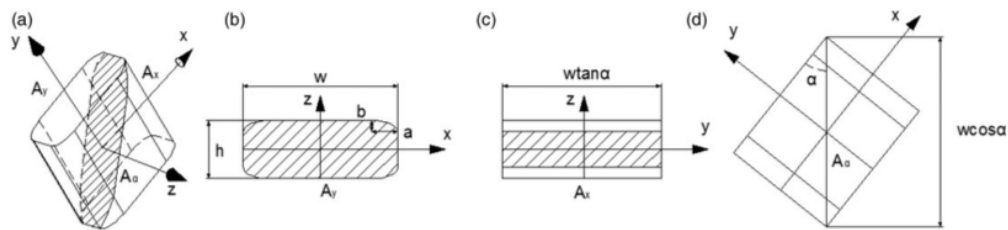
Figure 2.11. The raster angle mechanics of a section of a filament are determined by the effective area being loaded. In a, b, and c the loaded area is shaded. The largest loaded area is in a, where the filament is loaded at 45 degrees. The filament is loaded along the length in b. The filament is loaded transversely in c. and the loaded area is the smallest. The definition of the angle of loading is shown to be with respect to the axis of the fiber in d.[6]

2.7.1.1 Shear Modulus and Transverse Stiffness at Positive Air Gaps. Multiple FDM mesostructures were evaluated by Li et al. including positive air gaps[4]. The mesostructures were tested at several different angles, but the raster angle process variable was kept at 0 degrees. When the air gap was positive, it was predicted and shown experimentally that the shear modulus and stiffness transverse to the filaments is 0 MPa.

2.7.2 Constitutive Model for Multiple Components

Constitutive equations describe one physical quantity with respect to another physical quantity. The particular constitutive equations considered in this project are stress-strain relationships. Two rule of mixtures models for a non-homogeneous orthotropic material are the Voigt[27] and Reuss models[28]. These are the classical models of adding stiffness and are also commonly referred to as parallel and series, respectively. These are based off the Hookean equations in section 2.6.3. These models can be used to describe materials such as fiber reinforced composites, where the fibers are oriented in one direction in the matrix. The fibers and matrix also have different material properties. Their structure bears resemblance to periodic FDM parts, as shown in figure 2.12. It can be seen that the long fibers are oriented along one axis similar to the way the voids are oriented in an FDM part. The direction along the axis of the fibers is denoted 1 and the transverse direction 2.

In the Voigt model, the strains, ϵ, in the fibers, l, and matrix, m, are the same. The stresses, σ, are distributed according to the volume fraction, f, of the fibers. In this way, the effective modulus along the axis, $E_{1-axial}$, can be calculated according to equation 2.15.

$$\epsilon_1 = \frac{\sigma_1}{\epsilon_1} = \epsilon_{1l} = \frac{\sigma_{1l}}{E_l} = \epsilon_{1m} = \frac{\sigma_{1m}}{E_m}$$

$$\sigma_1 = f\sigma_{1l} + (1-f)\sigma_{1m}$$

$$E_{1-axial} = \frac{\sigma_1}{\epsilon_1} = \frac{f\sigma_{1l} + (1-f)\sigma_{1m}}{\frac{\sigma_{1l}}{E_l}} = fE_l + (1-f)E_m \tag{2.15}$$

In the Reuss model, the role of stresses and strains is reversed from the Voigt model; the stresses are equal and the strains are distributed due to f. This allows the calculation of an effective modulus that is transverse, $E_{2-trans}$, to the fibers as demonstrated in equation 2.16.

$$\sigma_2 = \frac{\sigma_2}{\epsilon_2} = \sigma_{2l} = \epsilon_{2l}E_l = \sigma_{2m} = \epsilon_{2m}E_m$$

$$\epsilon_2 = f\epsilon_{2l} + (1-f)\epsilon_{2m}$$

$$E_{2-trans} = \frac{\sigma_2}{\epsilon_2} = \frac{\sigma_2 f}{f\epsilon_{2l} + (1-f)\epsilon_{2m}} = \left(\frac{f}{E_l} + \frac{1-f}{E_m}\right)^{-1} \tag{2.16}$$
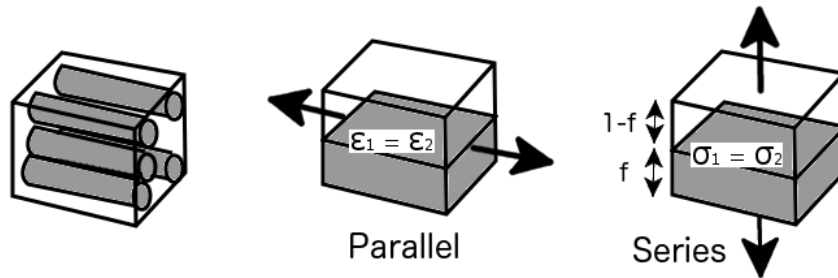
Figure 2.12. A schematic of a fiber reinforced composite is shown in a. The series and parallel additions are still preserved if the fibers are all considered one component. Therefore, they can be grouped together as shown in b and c. The Voigt model considers the parallel loading condition in b. The Reuss model considers the series loading in c.

2.7.3 Homogenization

When the effective properties of a part that is composed of fibers and a matrix are calculated, a concept called homogenization is being used. In more general terms, homogenization attempts to take the known properties at a smaller scale and generate effective properties at a larger scale. In the case of the Voigt and Reuss models, the properties of the fibers and matrix are known, and the volume fractions are used to generate effective properties. Another common approach is identifying a representative volume element, RVE, with volume, $\bar{v}$. For FDM parts, the RVE can be identified for mesostructures with a repetitive or periodic unit cell[5]. At the length scale of the RVE, the stress and strain fields are discontinuous. However, if a periodic microstructure is identified, then the RVE has properties that are representative of the larger structure[5]. Rodríguez et al. shows that the macroscopic stresses, Σ, and strains, E, are the average of the mesoscale stress, σ, and strain, ϵ, of all RVE elements over the volume, V, of the entire macroscopic element. The displacement vector, u, and the vector normal, n, to the surface, S, being acted on are used to define E.

$$\Sigma = \frac{1}{V} \int_{\bar{v}} \sigma \, dV \tag{2.17}$$

$$E = \frac{1}{V} \oint_{\bar{v}} \frac{1}{2} [u \otimes n + n \otimes u] \, dS \tag{2.18}$$

Rodríguez et al. go on to formulate the form of the effective macroscopic stiffness tensor, $\bar{C}$, for FDM materials. In the definition of $\bar{C}$, C is the fourth order stiffness tensor of the filaments, and H is the fourth order homogenization tensor.

$$\Sigma = \bar{C}E \tag{2.19}$$

$$\bar{C} = \frac{1}{V} \int_{\bar{v}} C : H dV \tag{2.20}$$

Rodríguez et al. show that their homogenization approach closely correlates to real world measurements of FDM parts produced with the polymer ABS for two particular mesostructures, one of which required a custom non-commercial process. FDM can produce many mesostructures, as discussed in the next section, so work needs to be done to expand constitutive modeling to any arbitrary FDM mesostructures. The particular mesostructure that Rodríguez et al. considered was unidirectional, raster angle equal to 0, no shells, and an air gap of -25.4 μm.

A model that combines geometric positions of filaments and material properties to directly calculate macroscopic properties from the mesostructure is developed by Liu et al[7]. The algorithmic definition of the mesostructure defines the position of the filaments but makes the assumption that the geometry transverse to the fibers is equivalent in two directions. This also assumes equivalent properties in those directions. The model uses green's function to define the filament-composed mesostructure and uses a Fast Fourier Transform to solve for the stiffness given stress and strain. Liu et al. show that the method is closely related to Finite Element Method (FEM) where the mesostructure is defined as a structure of interacting filaments. Although the model has the capacity to solve for a stiffness tensor, the model is experimentally validated by a single modulus measurement in a single direction. However, this model does demonstrate the possible effect of the mesostructure on the macroscopic properties.

2.8 FDM Characterization

2.8.1 Volume Fraction

Volume fractions were essential to the materials models developed by Rodríguez et al[5]. They used real world measurements of the volume so that the properties of the FDM part could be related to bulk polymer properties. An attempt to relate volume to process variables using a regression approach is developed by Srivastava et al[29]. They used six different process variables and applied it to an unknown geometry. The volume was obtained directly from the 3D printing software and the volume was not measured. The volume changed in relation to the process variables and this was captured in a regression analysis. Although it is not sure what geometry the model represents, Srivastava et al. showed that in general process variables can be linked to volume. However, the issue becomes more complex because the material volume reported by the 3D printing software does not accurately represent the real volume of material printed to create an FDM part[30].

2.8.2 Mesostructure Characterization

When the toolpath instructions are sent to the 3D printer, the nozzle follows the toolpath and builds a part layer by layer. The final mesostructure of the part is a result of these paths. Several studies have focused on characterizing the mesostructure of FDM parts, especially in relation to the build style. These studies have also focused on identifying how close the real mesostructure is to the ideal mesostructure represented by the build style.

Early studies started by considering one standard mesostructure[31]. As mentioned in 2.7.3, this mesostructure has a raster angle of 0°, no shell, and an air gap of -25.4μm. Rodríguez et al. found that the mesostructure consisted of a repeating RVE. The voids seen in the cross-sectional plane are described as squares with an area density. The area density is defined as the size of one void per RVE. The RVE elements were shown to be similar in shape to each other, but small random deviations were present. The void density was measured from micrographs.

Li et al. expanded on the previous study by varying the air gap variable[4]. They still calculated the area density per RVE, but did it directly from filament shape. However, they still measured the average overlap between filaments from micrographs. This overlap and filament shape is important in defining the mesostructure of FDM parts and how they deviate from an ideal structure.

Another study that found thermal cycling increased the surface roughness[32]. This has implications in sheet metal forming because increased roughness restricts metal flow and plastic tools are likely to heat when stressed. In addition to the overall randomness, Bakar et al. found that filaments deposited along circular toolpaths were more likely to deviate from the toolpath[33].

2.8.3 Mechanical Characterization

Mechanical characterization of FDM parts has taken two approaches: mesoscale and macroscopic. Mesoscale characterization requires a model to relate the mesoscale properties and structure to the macroscopic properties. The studies[5,6,8,26,31] that most influence the mesoscale approach in this project have already been discussed in sections 2.7.3 and 2.6.5. However, these studies are limited in scope and do not account for a

raster angle or shell. They consider the air gap, orientation, and changes in the stress distribution due to changes in void content and contact area between filaments.

One other significant mesoscale approach represented the FDM mesostructure as an FEM beam model as shown in figure 2.13. Villalpando et al. used the FEM model to predict the load to failure for several mesostructures[1,34]. However, compliance or stiffness of the FDM structure were not evaluated.

The majority of studies focused on characterizing the macroscopic properties of FDM specimens in tension at different orientations[9,35,36]. Domingo-Espin et al. characterized the stiffness tensor of a single build style and designed a component with a FEM model that incorporated the stiffness tensor[37].

2.8.3.1 Central Composite Design of Experiments. The FDM process has a wide variety of process variables that can be changed, and no well-defined analytical equations to describe the effect of the process variables to final properties. This makes it appealing to try a central composite design of experiments to obtain a response surface and derive a regression analysis equation.

The following papers all apply a regression type analysis to understand the impact of several process variables. Their approach involves testing a lot of different specimens
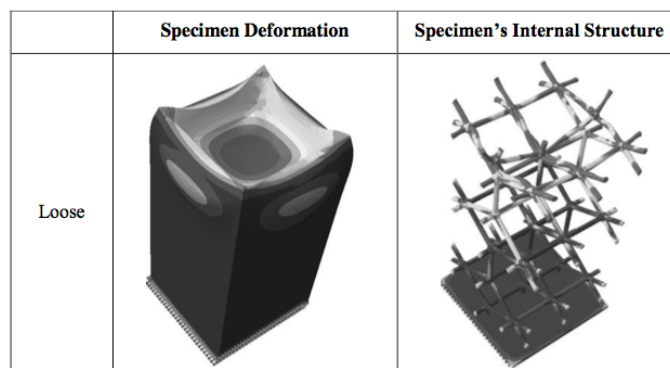
Figure 2.13. FDM mesostructure represented as a FEM beam model[1]

and changing the process variables. This was useful in finding the process variables that were most impactful on the mechanical response. However, the regression analysis was not robust enough to achieve reliable prediction of properties for a build style. Additionally, the regression type analyses did not result in a stress tensor that could be incorporated into a FEM model used in sheet metal forming analysis. The process variables found to impact mechanical properties the most include air gap, raster angle, slice height, raster width, and number of shells[38–45].

2.9 Testing

Most of the past studies focused on tensile testing. No standards exist for the testing of FDM parts, so the tests were typically adapted from ASTM D638, the tension test standard for rigid polymer[46]. However, it has been noticed that these tests have notable downsides since FDM parts are not homogenous materials. Notably, the tension tests fail at the fillet radius of the dog bone specimen[38]. This is due to the rasters terminating at the contour, which is rounded in the fillet radius. It is thought that this termination acts as a stress concentrator and leads to premature failure of the dog bone specimens. Therefore, another standard has been commonly modified for testing FDM in tension. ASTM D3039, the standard for laminated composites uses a rectangular prism test specimen, which allows the rasters to be uniformly loaded[47].

The standard for rigid polymers in compression is ASTM D695[48]. This test has perceived complexity due to the need for high alignment and the introduction of shear stresses through frictional constraints. To test this complexity, the National Institute for Standards and Technology (NIST) ran a repeatability study on the compression test for

metals, ASTM E9 [49,50]. This test is almost identical to ASTM D695 and uses the same test setup. The part geometry and strain rate differ. In both ASTM E9 and D695, 3 things are optional: lubricating the surfaces, using spherical seating platens, and choosing between strain and displacement control. NIST shows that the material properties measured are similar regardless of the choices made. However, the strain-time curve is straight for strain controlled tests and curved (concave-up) for displacement controlled tests as seen in figure 2.14.
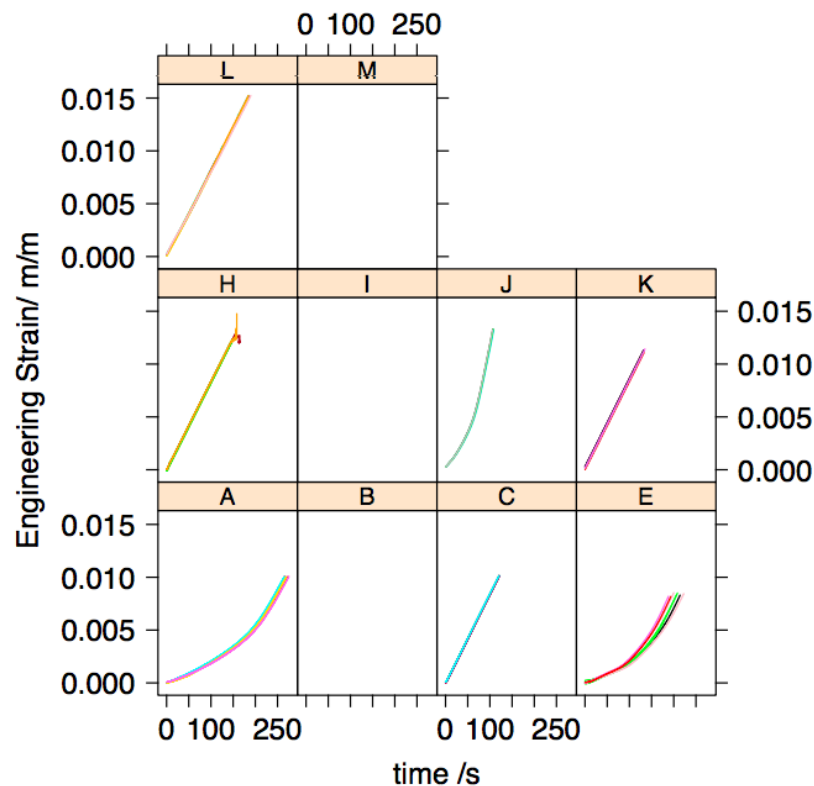
Figure 2.14. This image shows the compressive strain-time plots from a round robin conducted by NIST. The round robin studied how similar the results were for compression tests carried out in several laboratories. Some labs didn't report time. Labs A, E, and J used displacement controlled testing. Labs C, K, H, and L used strain controlled testing.

2.9.1 Defining the Compression Test

During a uniaxial compression test, a load is applied along a single axis. However, the material and test remain three dimensional. From equation 2.11, it can be seen that a uniaxial stress leads to deformations in more than one direction. These strains are are described by the poisson's ratio. The applied strain rate results in a compressive strain is along the axis of compression. However, the specimen also wants to expand along the other axes of the cartesian coordinate system during a compression test. If we take an example positive cartesian coordinate system and the axis of compression is defined as Z, then the other axes are defined as X and Y. A compressive strain ϵ_Z results in strains along X and Y given by the appropriate poisson's ratio:

$$\epsilon_X = -\nu_{XZ}\ \epsilon_Z$$

$$\epsilon_Y = -\nu_{YZ}\ \epsilon_Z$$

2.9.1.1 Frictional Constraints. Since a uniaxial strain is applied, the specimen wants to strain uniformly along any one axis. In the above example, the strain along X or Y would therefore be uniform along the length of the specimen in the Z direction. However, the contacts between the specimen and the compression platens imposes a frictional constraint. This constraint applies a shear force to the Z and -Z faces.

2.9.2 Digital Image Correlation

Digital Image Correlation (DIC) is a tool that is used to identify the deformation of a random isotropic pattern[51]. This random pattern is usually a randomly generated speckle pattern, since this fulfills the criteria. DIC works in two parts: tracking movement and

mapping displacement. Two user defined variables are important in determining how the DIC algorithms identify and track movement and deformation: subset size and step size. The subset size is defined in pixels and the area of the subset size is the number defined by the user squared. The subset size is used to identify a unique family of speckles. This family is tracked using correlation functions. The step size is the distance the algorithm moves from one subset to the next. Usually, the step size is chosen so that these overlap. The greater the subset size and step size, the more the data is smoothed.

The deformation is calculated using shape functions that determine whether the subset was deformed. The DIC algorithms calculate a strain for each subset. This is analogous to placing thousands of tiny strain gauges across the surface of the specimen. This can reveal a strain field with high resolution and contains a lot of data about the deformation of a sample.
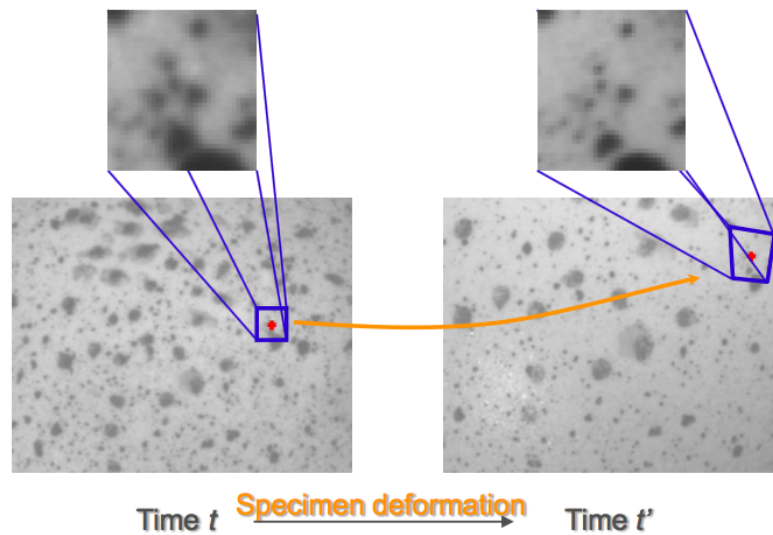
Figure 2.15. This figure shows both the displacement and strain features of DIC. The correlation functions are used to track a family of speckles and then the shape functions are used to identify the deformation of the subset. This image was taken from a presentation by Correlated Solutions.

3   Methods

FDM materials were designed from a great number of process variables, which allowed for a wide range of possible mesostructures. This project did not characterize all of the structures. Instead this project developed a method that described how the CAD model influenced the mesostructure and how the mesostructure influenced the final properties. The CAD model was defined as the original three dimensional geometry as well as the processing introduced by the 3D printer software that generates the toolpaths. An approach with two steps was developed to describe and predict the stiffness of FDM materials directly from the process variables. The first step described the changes in the mesostructure that occurred due to the process variables and how those changed the stiffness. This involved proven rule of mixtures approaches and rotating the stiffness tensor from the mesoscale layer coordinate system to the macroscopic part coordinate system. The second step generated effective properties for FDM parts by using the homogenization of multiple mesostructures to macroscopic properties. This step utilized a unique method of treating an FDM part as an assembly of multiple components. A tangent modulus was chosen as the property to compare mesostructures. A comprehensive design of experiments (DOE) was developed to determine the variability in the tangent modulus measurement and to validate the constitutive relationships and

the homogenization approach. Additionally, the DIC measurement techniques used in this project provided great insight into the mechanical response of FDM materials and additional observations were made to support the strain mapping.

Symbol	Definition	Units	CAD Defined/ Modeled/ Measured	Page Defined
g	air gap between filaments	mm	CAD	42
q	number of filaments per toolpath	NA	CAD	42
w	width of filaments	mm	CAD	42
d_{min}	minimum distance between straight and parallel toolpaths	mm	Model	42
d_{fil}	distance between center of filaments in mesostructure	mm	Model	52
ϕ	raster angle	Degrees	CAD	42
γ	orientation of a layer	Degrees	Model	42
h	slice height process variable	mm	CAD	42
z	vector of all the locations of layers along the Z axis	mm	Model	42
l	index of a layer	NA	Model	42
s	unit length transverse to fiber axis	$1mm$	Model	53
n_{fil}	number of filaments along the unit length	NA	Model	52
f_{fil}	volume fraction in the 1, 2, and 3 directions due to the change in air gap	NA	Model	53
c_{comp}	number of sub-components with unique orientations	NA	Model	56
f_{comp}	volume fraction in the X and Y directions due to the raster angle	NA	Model	53
$E_{1,2,3}^{nom}$	nominal tangent moduli of the mesostructure	MPa	Model	50
$E_{1,2,3}^{arb}$	tangent moduli of the mesostructure with positive air gap	MPa	Model	53 & 54
$E_{1,2,3}^{rot}$	effective tangent moduli of the mesostructure with a positive raster angle	MPa	Model	55 & 58
$E_{1,2,3}^{fill}$	effective tangent moduli of the mesostructure with an arbitrary air gap and positive raster angle	MPa	Model	59
$E_{X,Y,Z}$	effective tangent moduli of the macroscopic part in three orthogonal directions	MPa	Model and Measured	59

Table 3.1. Symbols used to define the CAD model, develop the equations for the constitutive model, and/or describe what was measured

3.1 Mesostructure

The mesostructure in this project was uniquely defined as a collection of regions with homogenous mesostructure. Homogenous mesostructure was the repetitive unit cell observed when the process variables stayed the same and the layers of the fill were composed of straight and parallel filaments. These regions closely matched the mesostructure of the FDM materials modeled in section 2.7. Therefore, a quantitative description of the mesostructure was created to directly relate the process variables to the material models.

We started out by defining the distance between toolpaths. Since the toolpaths were parallel, the distance considered was the shortest distance between two parallel lines.

$$d_{min} = q \times w + g \tag{3.1}$$

where d_{min} was the shortest distance between two parallel lines, q was the number of filaments per toolpath, w was the width of a single filament, and g was the air gap as defined by the designer. If $g \leq 0$, all the filaments in a layer would be touching their neighbors.

Additionally, the toolpaths were oriented in the X-Y plane by an orientation to the X axis. The orientation of the first layer was specified by a constant, γ_0. Then, the orientation of each subsequent layer was determined by the raster angle variable, ϕ.

$$\bar{z} = h * \bar{l}$$

$$\bar{l} = h * \bar{z}$$

$$\gamma_l = \left(l \times \phi + \gamma_0 \right) \ mod \ 180 \tag{3.2}$$

If the raster angle was greater than 0, the layer orientation, γ_l, changed continuously as the part is built along Z, with discrete layers at each of the layer indices, $\bar{l}$. The vector z represented the Z coordinate of all layers, h was the slice height variable as defined by the designer. The orientation of a layer at index l was given by equation 3.2. The discussed process variables that control the FDM process were collectively known as the "Build Style." The build style defined the process and had great influence on the final properties and mesostructure of the FDM part. A CAD model of the build style, including two layers, is shown in figure 3.1. In this CAD model, there was one filament per toolpath, a large air gap, a single toolpath in the contour, and a raster angle of 90° between the two consecutive layers.
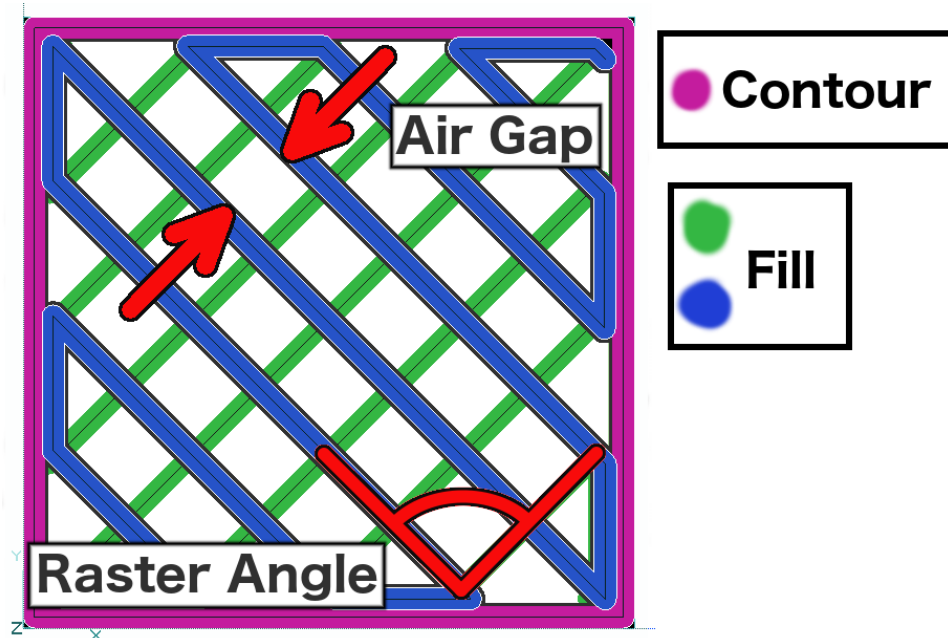
Figure 3.1. FDM Structure In-Plane: In the plane, the air gap determined the spacing between rasters. The raster angle determined the angle the filaments in this layer make with the layer beneath it.

3.1.1 FDM Coordinate System

When designing an FDM part, the software Insight (Version 110, Stratasys, Eden Prairie MN) was used. The Insight software defined a coordinate system for the FDM part. This was adopted as the macroscopic coordinate system. The axes in the macroscopic coordinate system were labelled X, Y, and Z as shown in figure 3.2.

This conveniently followed the convention for laminates. For each individual layer, another coordinate system was defined that also followed the convention for coordinates of a single lamina. This was called the mesoscale coordinate system. The axes were labeled 1, 2, and 3 as shown in 3.2. The orientations of each layer followed the description of orientation of filaments earlier in this section. Therefore, the orientations were described as an angle to the x axis in the x-y plane (i.e. 0° was a layer where all the filaments were aligned along the x axis).

3.1.2 Symmetry in the Mesostructure

The nominal mesostructure was defined as the mesostructure where the process variables considered, air gap, raster angle, and number of contours, were set to 0 in their respective units. A computer-produced visual of the nominal mesostructure is shown in figure 3.3. The lack of a raster angle means that the nominal mesostructure is composed of a single component. Therefore, the fibers in each layer of the mesostructure are oriented in the same direction. The axes for the mesostructure are therefore constant throughout the mesostructure.

By adding a positive air gap to the nominal mesostructure, the structure decreased in density. Also no straight path in the X-Y plane of the material continuously touched
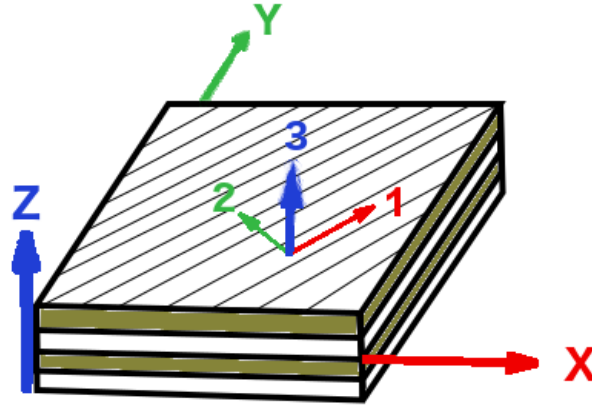
Figure 3.2. Macroscopic and mesoscale coordinates for a laminate were defined differently. The macroscopic coordinates were labelled X, Y, and Z and were oriented with respect to the directions the part was built in. In contrast, the laminar coordinates were labelled 1, 2, and 3 and were defined with respect to the axis of the filaments where 1 was along the axis. The build direction, Z, and the out of layer direction, 3, were always the same direction. This schematic represents the real FDM mesostructure, where γ_0 is 45° and ϕ is 90°.

filaments as shown in figure 3.4. This structure was still considered a single component, since there was no raster angle.

By adding a raster angle, each layer was rotated by an angle to the layer beneath it. This changed the orientation of the layers with respect to the macroscopic coordinate system of the FDM part as shown in figure 3.5. Direction 3 stayed the same for each of the layers. Since the layers have different orientations, the structure is considered to have multiple mesostructures. These were represented as separate sub-components: one for each of the orientations as shown in figure 3.7.
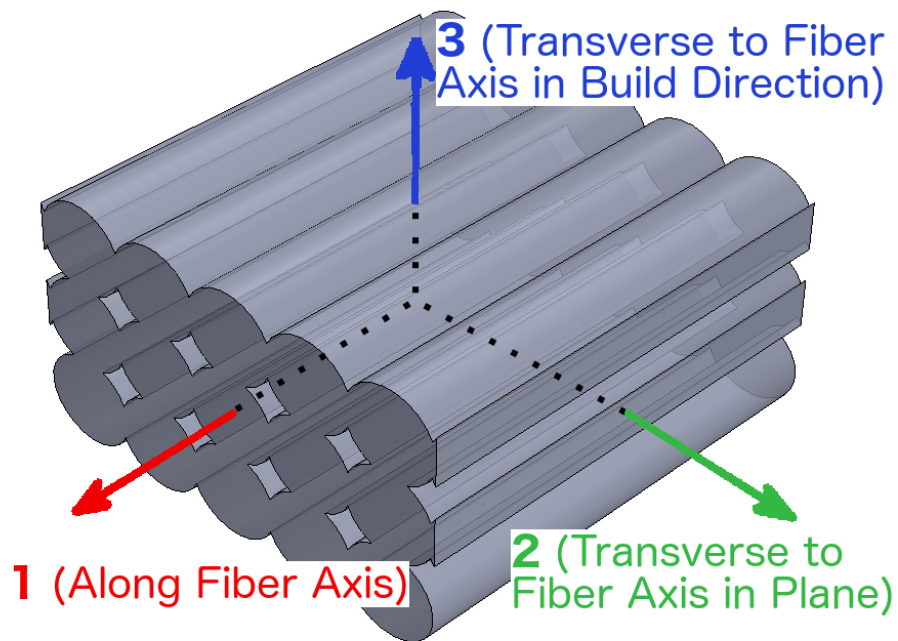
Figure 3.3. Nominal Mesostructure: Isometric view of a computer generated graphic with transparent material

3.1.3 Hierarchy at Multiple Length-Scales

The hierarchy considered in this study was inspired by the homogenization techniques discussed in sections 2.7.3 and 2.6.5. These methods identified a homogenous mesostructure that was composed of a smaller unit cell. However, in these approaches, all the unit cells had equivalent properties. In this project, the approach considered components with different properties that were homogenized to obtain effective properties for the macroscopic part.

3.1.3.1 Filaments. The smallest continuum unit was assumed to be a single filament of an FDM part. It also assumed the properties of a single filament were not altered for the three process variables considered. The largest non-homogeneous unit in an FDM part was a unit cell composed of filaments and voids.

Figure 3.4. Mesostructure with Positive Air Gap: This mesostructure was generated with a Fortus 400mc (Stratasys, Minnesota) and showed the real mesostructure with zero values for the contour or raster angle process variables. For this figure, the 3 direction of the mesostructure is normal to plane of the image. The orientation of the fibers is the 1 direction and the 2 direction is up.
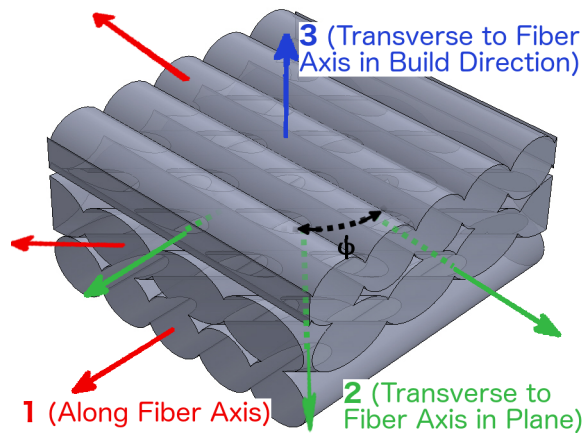
Figure 3.5. Mesostructure with 45° Raster Angle: The isometric view (A) demonstrated the different orientations of layers when a raster angle was introduced.

3.1.3.2 Mesostructure. The mesostructure was composed of filaments and was everything larger than the unit cell. The mesostructure was therefore a homogeneous region divided into unit cells if the air gap and orientation of a layer did not change. However, when these variables were different throughout the FDM part, then the mesostructure would be inhomogeneous.

3.1.3.3 FDM part. The macroscopic FDM part is composed of multiple components, each with a homogeneous mesostructure. In the special case the FDM part is composed of one component, the mesostructure of the FDM part is homogeneous.

If this approach is taken, the representation of the mesostructure can be simplified. Previously, the number of contours was considered to be part of the process variables. However, the only unique aspect of the contour was that the air gap was equal to 0 and it wasn't oriented with filaments in the fill, as discussed in section 2.4. Therefore, the contour can be defined as a component where all build style variables were the same except for the orientation. If the contour is straight, then it can be considered a single component.

Using the multiple components approach produces a part that can be considered as an assembly of different components. Additionally, by removing the contour as a process variable, the degrees of freedom of the process were reduced by one. A graphical representation of how the three dimensional structure was represented as multiple components is shown in figure 3.6.

The contours were also referred to as shells. Typically, contour referred to the toolpath designed in the CAD model and shell referred to the actual printed structure. Note that the two shells on either side of the fill were considered to be the same. This approach was inspired by the volume fraction models for fiber matrix composites, where
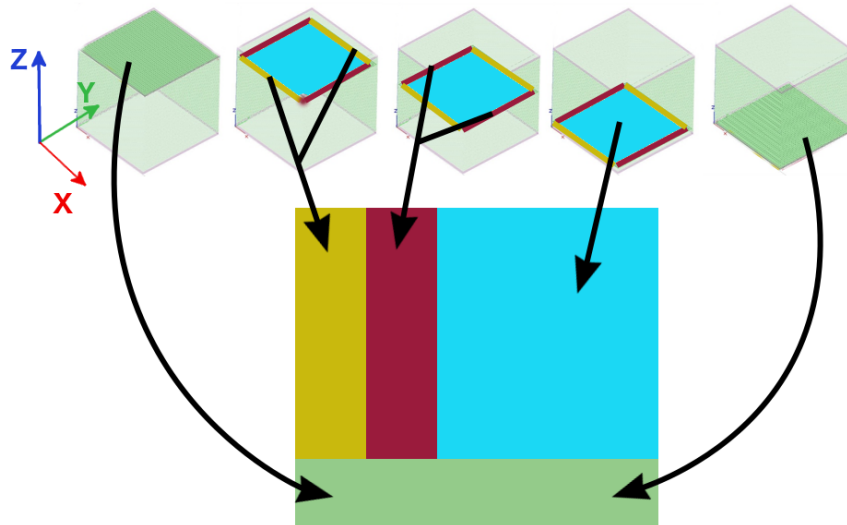
Figure 3.6. FDM Part with Multiple Components: The three dimensional part can be decomposed into a component representation with reduced complexity. Each component has a unique mesostructure that is defined by the air gap and raster angle. A component is defined by exactly one air gap and one raster angle. When the air gap or raster angle change, a new component needs to be defined.

the only geometric consideration was the area fraction as discussed in sections 2.6.3 and 2.7. Additionally, this approach was applied to layers that were oriented in the same direction. If the layers were oriented in different directions, they were considered new components. Layers with the same orientation were combined into a single component as shown in figure 3.7. This method worked with the methods discussed in 2.6.3 as long as the new components preserved the original series or parallel relationships between the layers.

Effective Part **Multiple Layers** **Homogenized Layers**
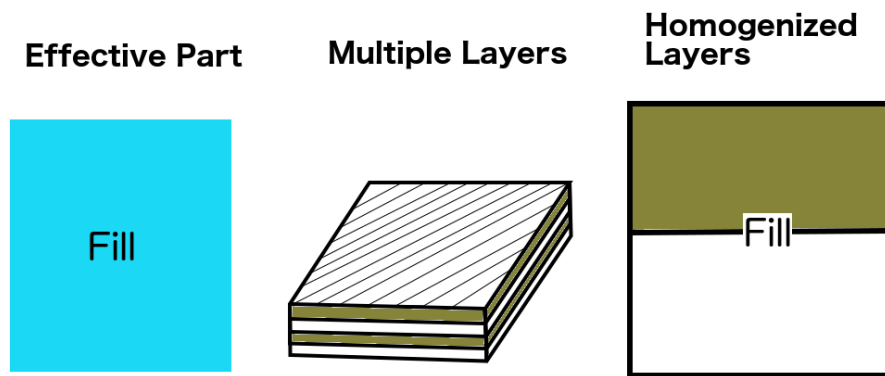
Figure 3.7. Homogenization of Multiple Layers with the Same Orientations: A fill could have multiple layers with different orientations. The layers with the same orientation were considered the same sub-component.

3.2 Constitutive Equations

The constitutive equations were developed for a homogeneous mesostructure. They were inspired by the rule of mixtures models for FDM parts, but were directly related to the process variables defined in the CAD model. The modulus that was manipulated was a real measured tangent modulus for a nominal FDM structure, versus the bulk material modulus used in past models. There were three nominal tangent moduli due to the anisotropy in the FDM properties. The properties were first manipulated for a change in air gap, which was described using a rule of mixtures approach. Then the properties of the layer were transformed into the macroscopic coordinate system to prepare for the homogenization of effective properties.

3.2.0.1 Nominal Tangent Modulus. Due to the symmetry discussed in section 3.1.2, the nominal mesostructure had three unique axes of anisotropy. This made the nominal mesostructure orthotropic and one tangent modulus, E, was defined for each of the three directions.

$$E_1^{nom}, E_2^{nom}, E_3^{nom}$$

3.2.1 Volume Fraction Air Gap

3.2.1.1 Directions 1 and 3. The tangent modulus in the 1 and 3 directions, E_1 and E_3, was a function of the air gap in the arbitrary mesostructure, g_{arb}, the nominal tangent moduli, E_1^{nom} and E_3^{nom}, and the filament width, w.

$$E_1^{arb}\left(g_{arb}, E_1^{nom}, w\right)$$

$$E_3^{arb}\left(g_{arb}, E_3^{nom}, w\right)$$

The rule of mixtures function was based on the volume fraction, f_{fil}, of an arbitrary mesostructure. In an effort to calculate properties directly from the CAD model, the volume fraction was determined as a relationship to the nominal volume present, where the number of filaments, n, took the place of volume. The number of filaments was defined as the number of toolpaths that could fit into a unit length, s, where the unit length was transverse to the axis of the filaments and remained the same in the nominal and arbitrary mesostructures.

$$s = s_{nom} = s_{arb}$$

The number of filaments that could be placed in this length was determined by the distance between filaments, d. For the case that there is only one filament per toolpath, equation 3.1 can be used to solve for the distance between filaments, d_{fil}. The number of filaments then follows logically as the total number of distances that fit into the unit length, as shown in equation 3.4.

$$d_{fil} = w + g \tag{3.3}$$

$$n = \frac{s}{w + g} \tag{3.4}$$

The ratio in the reduction of the number of filaments, $\frac{n_{arb}}{n_{nom}}$, was then calculated from the number of filaments for each of the arbitrary mesostructures.

$$\frac{n_{arb}}{n_{nom}} = \frac{\frac{s_{arb}}{w_{arb} + g_{arb}}}{\frac{s_{nom}}{w_{nom} + g_{nom}}} \tag{3.5}$$

Additional simplifications were made from the definitions of the mesostructure made in section 3.1 and from other assumptions. From section 3.1 we knew that the air gap, ag, for a nominal mesostructure is defined as 0 units of length. Additionally, if the filament width process variable is not changed, then the filament widths, w, for a nominal and arbitrary mesostructure will be the same. Then the ratio for the number of filaments is simplified as shown in equation 3.6.

$$g_{nom} = 0$$

$$w = w_{nom} = w_{arb}$$

$$\frac{n_{arb}}{n_{nom}} = \frac{w}{w + g_{arb}} \tag{3.6}$$

Since the number of filaments took the place of volume, the volume fraction, f_{fil}, is equivalent to the ratio of the filaments, $\frac{n_{arb}}{n_{nom}}$.

$$f_{fil} = \frac{n_{arb}}{n_{nom}}$$
$$f_{fil} = \frac{w}{w + g_{arb}} \tag{3.7}$$

3.2.2 Stiffness Air Gap

For the 1 and 3 directions, the filaments and voids ran along the length of the FDM part. Therefore, the Voigt model, as given in equation 2.15, was used to calculate the tangent modulus of an arbitrary mesostructure. Since the voids have no stiffness, the Voigt model was simplified to equation 3.8.

$$E^{arb} = f_{fil}\, E^{nom} \tag{3.8}$$
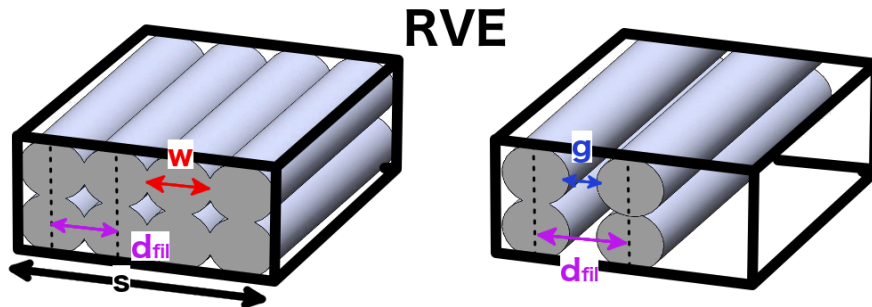
Figure 3.8. Representative Volume Element: The RVE was used to define the volume fraction, where the volume fraction was the number of filaments and air gaps that fit along an arbitrary length. The volume fraction was used for all the following models such as the air gap stiffness, raster angle stiffness, and mass models.

Combining equations 3.7 and 3.8 gave the tangent modulus for the 1 and 3 directions for an arbitrary mesostructure.

$$E_1^{arb} = \frac{w}{w + g_{arb}} E_1^{nom} \tag{3.9}$$

$$E_3^{arb} = \frac{w}{w + g_{arb}} E_3^{nom} \tag{3.10}$$

Note that this method assumed that the nominal mesostructure had a volume fraction of 1. This was not the real volume fraction of the filaments. It was used as a relationship between the volume of material in the nominal mesostructure as compared to the volume in an arbitrary mesostructure.

3.2.2.1 Direction 2. If there was a positive air gap, then no material continuously supported the load applied in the 2 direction as shown in figure 3.4. Additionally if bending strength was ignored, then the effective modulus in the 2 direction became zero. This resulted in a piecewise definition for E_2^{arb}. Section 2.7.1.1 discussed a study that experimentally validated that a positive air gap resulted in a stiffness much less than a MPa in direction 2.

$$E_2^{arb}\left(g_{arb}, E_1^{nom}\right)$$

$$E_2^{arb} \begin{cases} E_2^{nom} & g_{arb} = 0 \\ \\ 0 & g_{arb} > 0 \end{cases} \tag{3.11}$$

3.2.3 Raster Angle

The raster angle oriented the filaments of a layer in relation to the macroscopic coordinate system, which is composed of the X, Y, and Z axes. Since the filaments were straight

lines, symmetry was used to define the limits of the raster angle. Firstly, the maximum raster angle different from 0° was 179°, since a straight line rotated 180° was equivalent to a straight line rotated 0°. A raster angle greater than 180° and less than 360° was the same as a raster angle between 0° and 179°. For example, a raster angle of 225° is the same as 45°. For the purposes of the following model, 180° was used instead of 0°. This made the range of ϕ from 1° to 180°. However, typically, 0° was used in the CAD model. Since the constitutive equations aim to directly relate the CAD model to the final properties the following piecewise definition for the raster angle, ϕ, was made.

$$
\phi \begin{cases} 180 & \phi = 0 \\ \phi & \phi > 0 \ \& \ \phi \leq 180 \end{cases}
\tag{3.12}
$$

3.2.3.1 Directions X and Y. When there was a positive air gap, the effective tangent modulus was 0 MPa for any direction other than along the axis of the fibers. Note that when the air gap was 0 mm, the stiffness of a layer was more complex and the following equations did not apply. The tangent modulus in different directions was not experimentally determined, but taken from past studies discussed in section 2.7.1.1. Additionally, a layer with an air gap has no shear modulus or poisson's ratio. Using equation 2.14, it was determined that only layers aligned in the direction of the desired effective tangent modulus contribute to the tangent modulus. Therefore, the tangent modulus in the X and Y directions was a function of the raster angle and the arbitrary tangent modulus in the 1 direction. Since the raster angle was a designer defined process variable, the proposed method again directly related final properties to the CAD model.

$$
E_X^{rot}\left(\phi, E_1^{arb}\right) = E_X^{rot}\left(\phi, g_{arb}, E_1^{nom}, w\right)
$$

$$E_Y^{rot}\left(\phi, E_1^{arb}\right) = E_Y^{rot}\left(\phi, g_{arb}, E_1^{nom}, w\right)$$

The volume fraction, f_{comp}, was determined as the fraction of sub-components with the proper alignment. This was done using equation 3.13, which calculated the number of sub-components, c_{comp}, when a raster angle, ϕ, was introduced. The raster angle had to be a divisor of 180° or be equivalent to a negative raster angle that was a divisor of 180°. Figure 3.9 shows the trend in the change of number of sub-components with raster angle.

$$If\ \phi\ |\ 180°\ or\ (\phi - 180°)\ |\ 180°,\ then\ c_{comp} = \frac{180°}{\phi} \tag{3.13}$$
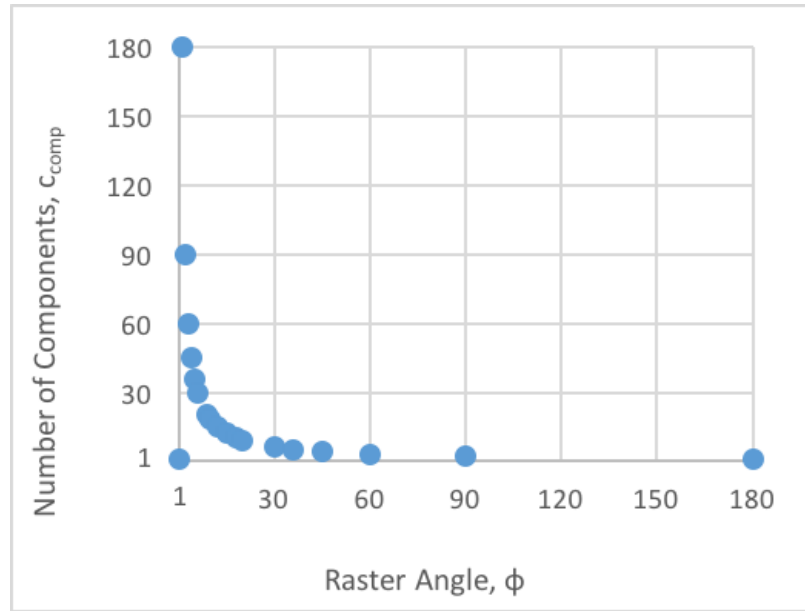
Figure 3.9. Number of Sub-Components with Raster Angle: When a raster angle is introduced, the number of unique orientations changes. With a raster angle of 1°, there will be 180 rotations until the orientation of a layer is the same as the first layer. When there is no raster angle and a raster angle of 180°, there is only one orientation that any layer can have.

Only one of these components was aligned with the axis of loading. Therefore, the volume fraction was equal to the fraction of the whole that the one aligned component represented.

$$f_{comp} = \frac{1}{c_{comp}} = \frac{\phi}{180°} \tag{3.14}$$

The adjusted stiffnesses at an orientation, E_X^{rot} and E_Y^{rot}, was calculated by modifying the previously calculated stiffness of an arbitrary mesostructure with equation 3.14. Originally, E_2^{arb} with a positive air gap originally had no stiffness, which meant there was no stiffness in the Y direction. However, after a raster angle was added, the layers aligned in the Y direction will provide a stiffness, E_Y^{rot}.

$$E_X^{rot} = \frac{\phi}{180°} E_1^{arb} \tag{3.15}$$

$$E_Y^{rot} \begin{cases} 0 & \phi = 0 \ \& \ g_{arb} > 0 \\ \frac{\phi}{180°} E_1^{arb} & \phi > 0 \ \& \ g_{arb} > 0 \end{cases} \tag{3.16}$$

The trend associated with the change in the predicted stiffness is directly related to the trend in the change of the number of sub-components. The change in the number of sub-components follows an exponential trend. However, real FDM parts typically do not have raster angles less than 15°. For raster angles greater than 15°, the change in the raster angle volume fraction, f_{comp}, is approximately linear, as is shown in figure 3.10.

3.2.3.2 Direction Z. In the build direction there was always contact between layers and thus contact between the components the layers were grouped into. The components were assumed to be an arbitrary mesostructure with an air gap, where none of the layers have any orientation in relation to the coordinate system of a component. Therefore, the
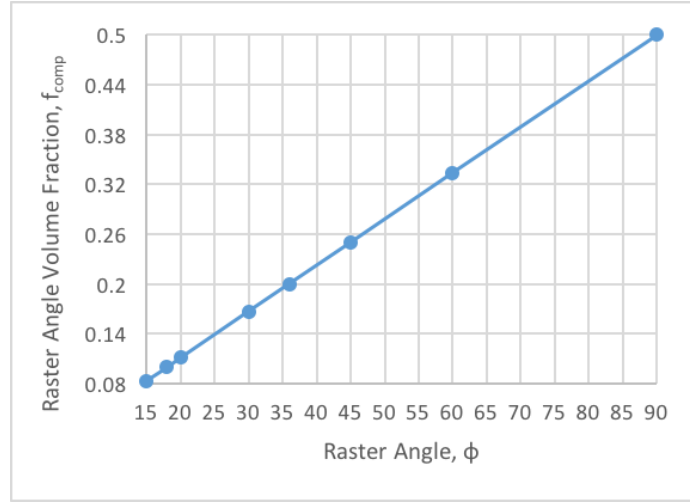
Figure 3.10. Change in f_{comp} with Real Raster Angles: Real raster angles are typically greater than 15°. In this region of the model, the trend is approximately linear.

components would have a tangent modulus in the 3 direction and therefore Z direction, E_Z^{rot}. This modulus was equal to the tangent modulus of the mesostructure with an arbitrary air gap and no raster angle.

$$E_Z^{rot} = E_3^{arb} \tag{3.17}$$

3.2.4 Combining Air Gap and Raster Angle

The reduction in area and therefore tangent modulus, $E_{X,Y,Z}^{fill}$, of a mesostructure with a positive air gap and raster angle was compounded when both the air gap and raster angle were changed. Modeling was accomplished by using the tangent modulus definitions for an air gap in equations 3.9, 3.11, and 3.10 and substituting for E^{arb} in equations 3.15, 3.16, and 3.17. Equations 3.18, 3.19, and 3.20 are the resulting compounded tangent modulus definitions. The *fill* subscript was used in reference to the homogenization approach.

$$E_X^{fill} = \left(\frac{w}{w+g}\right)\left(\frac{\phi}{180°}\right) \times E_1^{nom} \tag{3.18}$$

$$E_Y^{fill} \begin{cases} 0 & \phi = 0° \ \& \ g > 0mm \\ E_2^{nom} & \phi = 0° \ \& \ g = 0mm \\ \left(\frac{w}{w+g}\right)\left(\frac{\phi}{180°}\right) \times E_1^{nom} & \phi > 0° \ \& \ g > 0mm \\ Not\ Defined & \phi > 0° \ \& \ g = 0mm \end{cases} \tag{3.19}$$

$$E_Z^{fill} = \frac{w}{w+g} \times E_3^{nom} \tag{3.20}$$

3.2.5 Homogenization

Macroscopic FDM parts, besides the fill, also included a component known as the shell. The shell was the name given to the component that was generated from many filaments laid on the contour toolpath. The nominal mesostructure had been chosen to be equivalent to the mesostructure of the shell because all FDM parts are designed to contain a shell around the fill. Therefore the shell was the nominal mesostructure and also had the same properties. The macroscopic tangent modulus, $E_{X,Y,Z}$, was therefore a function of the nominal tangent modulus, $E_{1,2,3}^{nom}$, the fill tangent modulus, $E_{X,Y,Z}^{fill}$, and the geometry. Additionally, the macroscopic tangent modulus could be obtained directly from the CAD model and the nominal tangent modulus measurements.

$$E_{X,Y,Z}\left(E_{1,2,3}^{nom}, E_{X,Y,Z}^{fill}, geometry\right)$$

$$E_{X,Y,Z}\left(E_{1,2,3}^{nom}, \phi, g_{arb}, w, geometry\right) = E_{X,Y,Z}\left(E_{1,2,3}^{nom}, CAD\ model\right)$$

The homogenization approach was adapted from Hooke's law in section 2.6.3. The geometry was the same as shown in figure 3.6. Using both Hooke's law and geometry the spring stiffness, k, of the macroscopic FDM part was described as the combination of spring stiffnesses of the components. The subscripts S1, S2, and S3 are used to simplify the shell1, shell2, and shell3, subscripts.

$$k_{eff} = \frac{1}{\frac{1}{k_{shell1}} + \frac{1}{k_{shell2}+k_{shell3}+k_{fill}}}$$

Using equation 2.10, the spring stiffnesses were converted to the geometric lengths, L, geometric areas, A, and material modulus, E, representation.

$$\frac{A_{eff}\,E^{eff}}{L_{eff}} = \frac{1}{\frac{L_{S1}}{A_{S1}\,E^{S1}} + \frac{1}{\frac{A_{S2}\,E^{S2}}{L_{S2}}+\frac{A_{S3}\,E^{S3}}{L_{S3}}+\frac{A_{fill}\,E^{fill}}{L_{fill}}}}$$

Geometric relationships, which were shown in figure 3.6 and described in section 3.5.5, were used to simplify the equations. Then, in line with the goal of homogenization, the stiffness equations were solved for effective macroscopic tangent modulus.

$$A_{eff} = A_{S1} = A_{S2} + A_{S3} + A_{fill}$$

$$L_{S2} = L_{S3} = L_{fill}$$

$$L_{eff} = L_{S1} + L_{S2}$$

$$E^{eff} = \frac{1}{\frac{L_{S1}}{\alpha_{S1}\,E^{S1}} + \frac{L_{S2}}{\alpha_{S2}\,E^{S2}+\alpha_{S3}\,E^{S3}+\alpha_{fill}\,E^{fill}}}\,\frac{1}{\frac{1}{L_{eff}}}$$

The area α and length fractions λ achieved even further simplification. The effective macroscopic tangent modulus in any of the three orthotropic directions could be solved using equation 3.21.

$$\alpha = \frac{A}{A_{eff}}$$

$$\lambda = \frac{L}{L_{eff}}$$

$$E^{eff} = \frac{1}{\frac{\lambda_{S1}}{\alpha_{S1}\,E^{S1}} + \frac{\lambda_{S2}}{\alpha_{S2}\,E^{S2} + \alpha_{S3}\,E^{S3} + \alpha_{fill}\,E^{fill}}} \tag{3.21}$$

In addition to predicting the macroscopic tangent modulus, the measured macroscopic tangent modulus of an FDM part could be used to calculate the tangent modulus of the fill of the part using equation 3.22.

$$E^{fill} = \frac{-\alpha_{S1}\,\alpha_{S2}\,E^{S1}\,E^{S2} - \alpha_{S1}\,\alpha_{S3}\,E^{S1}\,E^{S3} + \alpha_{S2}\,E^{S2}\,E^{eff}\,\lambda_{S1} + \alpha_{S3}\,E^{S3}\,E^{eff}\,\lambda_{S1} + \alpha_{S1}\,E^{S1}\,E^{eff}\,\lambda_{S2}}{A_{fill}\,(A_{S1}\,E^{S1} - E^{eff}\,\lambda_{S1})} \tag{3.22}$$

The exact stiffness of the components depended on the orientation to the macroscopic part. The following table 3.2 outlines which values replaced the component moduli, $E^{S1,S2,S3}$ used in equations 3.21 and 3.22. Also for clarification, the fill and macroscopic coordinate system is the same. Therefore, when E_X^{eff} was calculated, E_X^{fill} was used on the right hand side of equation 3.21.

Direction	E^{S1}	E^{S2}	E^{S3}
X	E_1^{nom}	E_1^{nom}	E_2^{nom}
Y	E_2^{nom}	E_1^{nom}	E_2^{nom}
Z	E_3^{nom}	E_3^{nom}	E_3^{nom}

Table 3.2. Shell tangent modulus values depended on the macroscopic orientation of the FDM part. This table outlines the appropriate orientation and modulus to use when representing the shell

3.2.6 Mass of an FDM part

The mass of an FDM part, m_{eff} depended on the mass of each of the components, m_{comp}.

$$m_{eff} = \sum m_{comp} \tag{3.23}$$

At a smaller scale, the mass of the component was also the sum of the mass of its constituents, the filaments and the voids. Since the voids had no mass, the mass of a component was the sum of masses of all filaments, m_{fil}. Also, if a representative volume element was considered, then all filaments in this RVE had the same mass. Therefore, the number of filaments, n_{fil}, were used to obtain the total mass.

$$m_{comp} = \sum m_{fil} = n_{fil} \times m_{fil} \tag{3.24}$$

Then the masses of a component with the nominal mesostructure, m_{nom}, and an arbitrary mesostructure, m_{arb} were defined with equation 3.24. Within the RVE, each component had a different amount of filaments, n_{nom} and n_{arb}, respectively.

$$m_{nom} = n_{nom} \times m_{fil} \tag{3.25}$$

$$m_{arb} = n_{arb} \times m_{fil} \tag{3.26}$$

Substituting for m_{fil}:

$$m_{arb} = n_{arb} \times \frac{m_{nom}}{n_{nom}} = \frac{n_{arb}}{n_{nom}} \times m_{nom} \tag{3.27}$$

Using equation 3.6, the mass of an arbitrary mesostructure was related to the mass of the nominal mesostructure, as long as they were both part of the same RVE with the same volume.

$$If \; V_{nom} = V_{arb} \, , \; then \; m_{arb} = \frac{w}{w + g_{arb}} \times m_{nom} \tag{3.28}$$

When the arbitrary and nominal mesostructure both had the volume of the RVE, the density relationship between the nominal density, ρ_{nom}, and arbitrary density, ρ_{arb}, was obtained by dividing by the volume of the RVE, V_{RVE}.

$$If \; V_{nom} = V_{arb} \, , \; then \; \frac{m_{arb}}{V_{RVE}} = \frac{w}{w + g_{arb}} \times \frac{m_{nom}}{V_{RVE}}$$

$$\rho_{arb} = \frac{w}{w + g_{arb}} \times \rho_{nom} \tag{3.29}$$

The mass of any FDM part depended on the density and volume of each of the components. When the FDM part was composed of a shell and a fill component, the mass of the FDM part could be obtained by their densities, ρ_{shell} and ρ_{fill}, and their volumes, V_{shell} and V_{fill}.

$$\rho_{shell} = \rho_{nom}$$

$$\rho_{fill} = \rho_{arb}$$

$$m_{eff} = m_{shell} + m_{fill}$$

$$m_{eff} = \rho_{shell} V_{shell} + \rho_{fill} V_{fill} \tag{3.30}$$

$$m_{eff} = \rho_{nom} V_{shell} + \frac{w}{w + g_{arb}} \rho_{nom} V_{fill} \tag{3.31}$$

3.3 Design of Experiments

The design of experiments (DOE) had several goals. The first was to observe if the macroscopic tangent modulus of an FDM part built from the same CAD model was consistently the same. This was necessary to validate the assumption that the properties of the material and the process were linked and that variability introduced by the 3D printing process did not effect the ability to model the tangent modulus. Secondly, the model needed to be validated across a range of process variables. This required getting the initial inputs for the model, which included three nominal tangent moduli. Variables were also chosen as those that would satisfy the models that were created. These included the raster angle and the air gap.

3.3.1 Nominal Measurements

To be able to measure the local properties of a mesostructure, the FDM part could not consist of other mesostructures. The only FDM mesostructure that could be observed with digital image correlation was the nominal mesostructure. This is because the surface of the nominal mesostructure was continuous unlike the mesostructures with a positive air gap. Therefore, the tangent moduli of the nominal structure were the same as the macroscopic moduli that were measured.

$$E_1^{nom} = E_X^{eff}$$

$$E_2^{nom} = E_Y^{eff}$$

$$E_3^{nom} = E_Z^{eff}$$
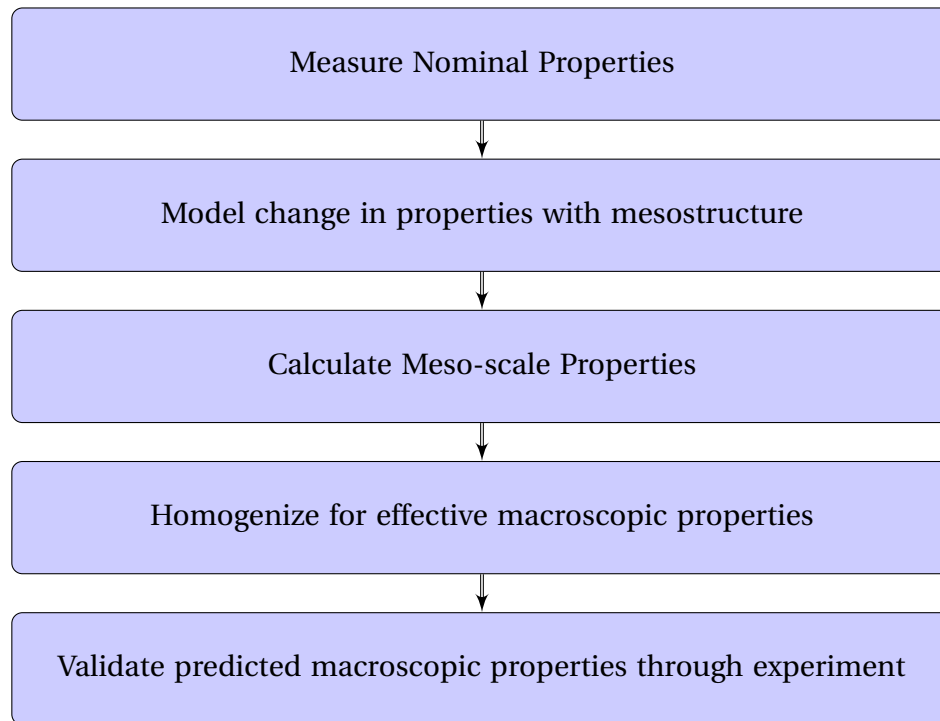
Figure 3.11. Hierarchical Modeling Approach: The modeling considered the effect of the smaller length-scales on the effective properties of an FDM material. The effective properties were measurable and used to validate the model.

3.3.2 Design Space- Choosing Process Variables

The design space was chosen from the variables identified in past literature to have the most significant impact on mechanical properties and evaluating the limits of Stratasys Fortus 400mc printers and the Insight software. The variables chosen from the past literature studies include air gap, raster angle, and material. The air gap boundaries were chosen from values that were shown to produce dimensionally accurate parts. Since the goal of the project was to directly relate 3D printing variables to final part properties, dimensionally accurate was defined as anything that could be used without additional manufacturing steps. The full ranges of the chosen variables were shown in table 3.3.

Variable	Min	Max
Air Gap	0mm	1.27mm
Raster Angle	0°	90°
Material Strength	ABS	ULTEM

Table 3.3. Design Space Variables and Ranges

3.3.3 Design Space- Defining Process Constants

Besides the variables chosen in this study, there existed many other process parameters. These were kept constant and were outlined in table 3.4

3.3.4 Test Specimen Shape

The test specimen shape was chosen to best meet the goals of the project. Considerations included the ability to measure mechanical properties, the material anisotropy, the integration with measurement tools, and the ability to compare results with other researchers. Additionally, the DIC measurements used in this project required the specimen to have a flat surface that stayed in focus when viewed with a camera. A cubic test specimen could be tested in any of three directions. This reduced the need to print a

Constant	Value
Printer	Fortus 400mc Large
Extrusion Tip	T16
Extrusion Temperature (ABS)	330°C - 360°C
Envelope Temperature (ABS)	>108°C
Extrusion Temperature (ULTEM)	380°C
Envelope Temperature (ULTEM)	195°C
Start Angle, γ_0	0°
Filament Width, w	0.508mm
Slice Height, h	0.254mm
Number of Shells	3

Table 3.4. Process parameters that were held constant. Data for extrusion and envelope temperatures was clearest for ULTEM and temperatures for all other materials were given as ranges[26]

new specimen at a different orientation. This meant that the cubic test specimen had improved utility and removed other variables that could arise from changing the 3D printing process. The utility was useful in that a bunch of specimens could be printed and then used for any test. Failed tests could easily be rerun with the extra cubic test specimens. Using the same CAD model also met the goals of the project that aimed to characterize the variability that arises through the 3D printing process. Additionally, some of the partners on the project were using cubic test specimens, and comparisons could be made in the future.

3.4 CAD Modeling

For this project, specimens were printed on a Stratasys Fortus 400mc 3D printer with a large envelope, 355mm × 254mm × 254 mm. The printer received instructions in the form of toolpaths, which instructed the printer where to move the extrusion nozzle and place a filament. These instructions were created and visualized in the Stratasys Insight software. The resulting CAD model represented the geometry, the mesostructure, and the instructions that made up the final part.

The CAD model was created by first generating the geometry in software capable of converting the geometry to the STL file format. Software examples included paid programs such as SOLIDWORKS or open source tools such as Google SketchUp. The STL file format could then be imported into Insight. The first step to creating the CAD

Shape	Height (mm)	Width (mm)	Length (mm)
Cubic	25.4	25.4	25.4

Table 3.5. Specimen Shape Dimensions
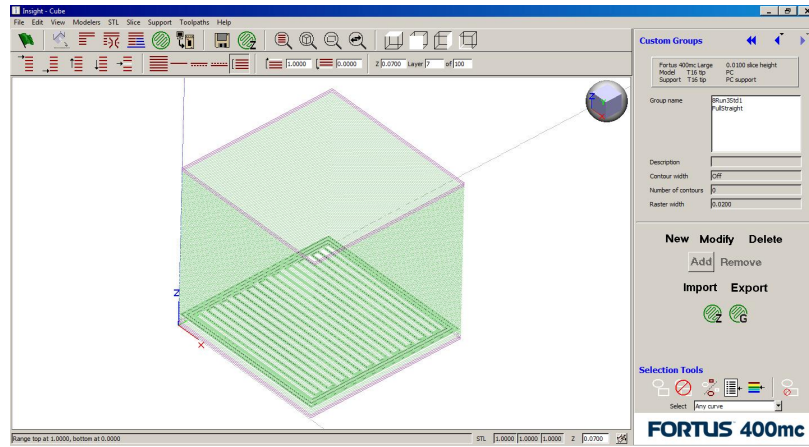
Figure 3.12. CAD Model of a Test Specimen- Insight Software: The CAD model was created in Insight software. It represented the geometry, the mesostructure, and the instructions that made up the final part.
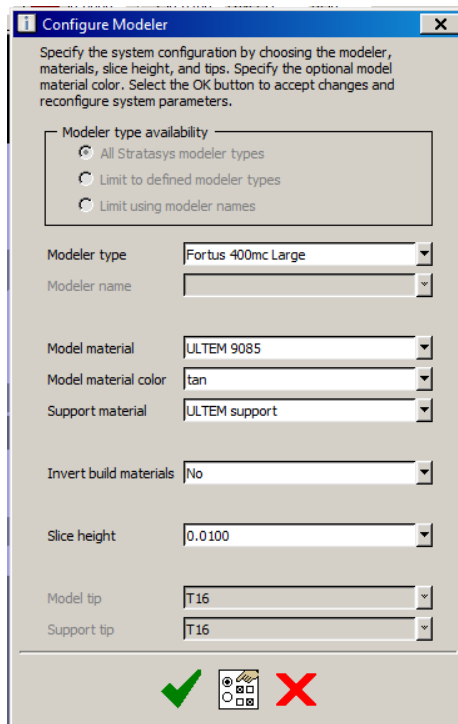
Figure 3.13. Modeler Setup- Insight Software: The modeler setup ensured the instructions were written for the correct 3D printer and 3D printer setup

model was configuring the modeler. This required selecting the appropriate printer and nozzle tip. Additionally, the slice height and material were defined in the modeler setup.

After the modeler was configured, four to five additional steps were required to finish the CAD model depending on whether the part needed supports.

    I. Slice 3D part into layers according to slice height parameter

    II. Create group that defines all other process variables

    III. Select layers and add group

    IV. Generate Toolpaths for each group

    V. (Optional) generate supports

The slicing of the 3D geometry creates layers that formed the final part. Any layer could be assigned a unique set of process variables or they could all be selected at once and assigned the same structure. Additionally, features within a layer that were spaced more than 0.0254mm apart could also be assigned separate process variables. Once the process variables were assigned, the toolpaths could be generated and viewed. Supports could also be added in case there was overhanging geometry that would be pulled down by gravity.

3.4.1 Printing Specimens

The Fortus 400mc is prepared by attaching the correct tip, inserting the correct polymer filament, and inserting a polycarbonate sheet onto the platform. The polymer sheet acts as the platform for the printing process and FDM parts are built on top of it. After the instructions are sent to the Fortus 400mc as a file with a .cmb extension, the FDM part is built layer by layer and the duration of the printing procedure is proportional to the volume of material deposited. If the specimens were printed with supports, then they
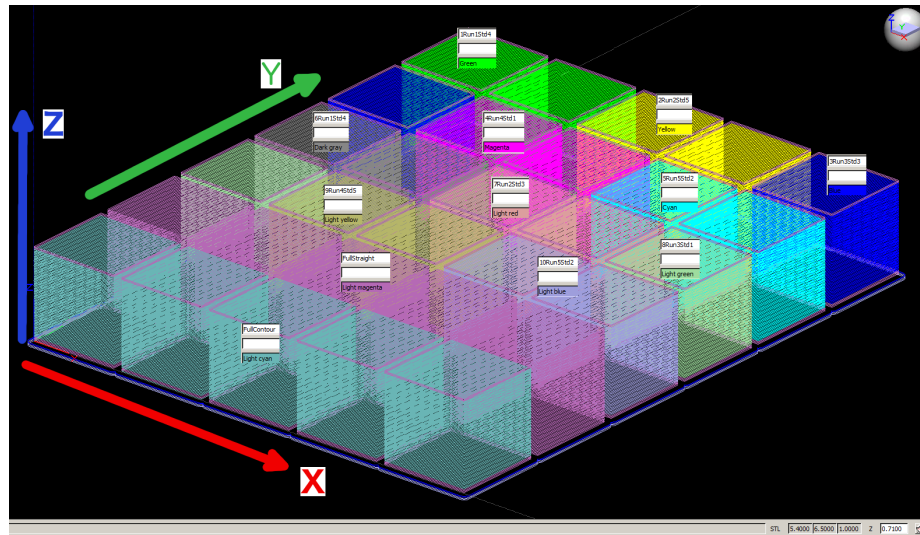
Figure 3.14. CAD Model of Specimens with Separate Process Variable Groups: Several groups of process variables could be defined in a single CAD model, although the slice height and material had to remain the same. These groups could be assigned to individual layers or features .

needed to be suspended in a detergent bath until the supports were gone. The composition of the detergent bath was reported by Stratasys as 60-70% sodium carbonate, 20-30% sodium hydroxide, 1-5% sodium lauryl sulfate, and 1-5% sodium metasilicate. The detergent bath was performed until the supports were gone, which can take longer than 8 hours.

3.4.2 Specimen Groups

Since each combination of process variables creates a specimen with unique structure and properties, these combinations will be given their own label as a group. Each group studied was inside the design space defined by the variables and constants in tables 3.3 and 3.4. The number of specimens per group varied depending on the goals. Test specimen groups 0000, 0400, 0445, and 8, were produced to test for the variance in tangent modulus measurements, therefore, a significant amount of them were produced. Other

groups were produced to explore the design space. Table 3.6 summarizes the groups studied in this project.

3.4.3 Control Specimens

In addition to FDM specimens, several control specimens were chosen for the project. These included materials that behaved as viscoelastic-plastic materials or as orthotropic materials. These properties were believed to be characteristic of FDM materials and would therefore provide a reference for how an ideal specimen would behave. The control specimen materials, properties, and orientation tested were listed in table 3.7. Only one of each control specimen was obtained.

Group ID	Air Gap (mm)	Raster Angle (Degrees)	Material	Number of Specimens	Tests Analyzed
0000	0.000	0.00	ULTEM 9085	16	15
0400	1.016	0.00	ULTEM 9085	16	12
0445	1.016	45.00	ULTEM 9085	16	15
1	1.067	76.82	ABS-M30i	2	3
2	0.597	45.00	ABS-M30i	2	3
3	1.067	13.18	ABS-M30i	2	3
4	0.121	13.18	ABS-M30i	2	3
5	0.121	76.82	ABS-M30i	2	2
6	1.270	45.00	ABS-M30i	2	3
7	-0.076	45.00	ABS-M30i	2	3
8	0.597	0.00	ABS-M30i	8	9
9	0.597	45.00	ABS-M30i	8	9
10	0.597	90.00	ABS-M30i	2	3
S	0.000	0.00	ABS-M30i	5	6

Table 3.6. Specimen Groups

Material	Properties	Orientation Tested
Nylon (Translucent White)	Homogeneous and isotropic	NA
Pine	Orthotropic	Across Grain
Poplar	Orthotropic	Along Grain
Maple	Orthotropic	Along Grain

Table 3.7. Control Specimens

3.5 Test Preparation and Procedure

The testing in this project was designed to apply a compressive strain to the testing spec-imens and take images of the test specimen. This required careful sample preparation, measurement calibration, measurement optimization, and controlled compression pa-rameters.

3.5.0.1 Measuring Mass. Before the samples were speckled with a random pattern for DIC, their mass was measured. The scale used to measure mass was GR-202, manufac-tured by A&D, and had milligram precision.

3.5.1 Sample Preparation

To prepare specimens for Digital Image Correlation (DIC) strain measurement required them to be coated with a random speckle pattern. The pattern was paint applied with an airbrush, where the paint was mixed 1 parts water to 2 part black acrylic paint. The pressure used to operate the airbrush was 12psi and the airbrush head was opened all the way. Figure 3.15 shows a typical resulting speckle pattern. Note that samples were not machined or altered in any way from their as-printed state except for the addition of a speckle pattern.
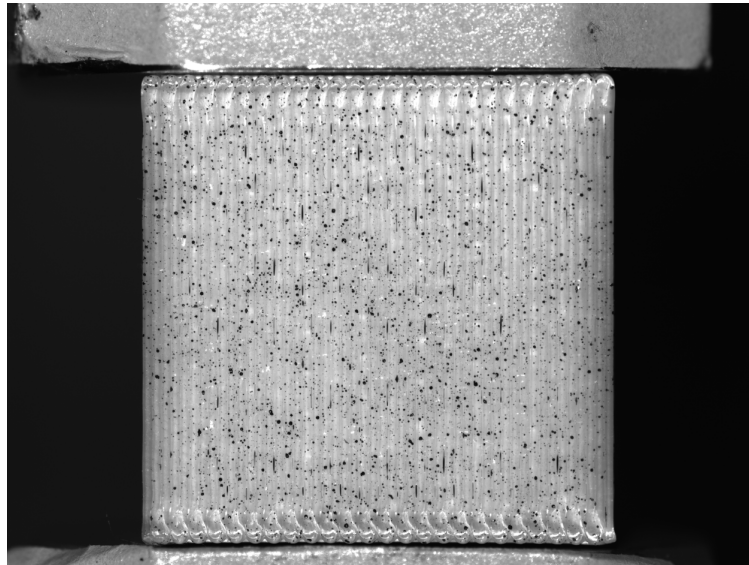
Figure 3.15. Typical speckle pattern- Specimen 0445A Face 3

3.5.2 DIC Validation

3.5.2.1 Spherical Aberration. Spherical aberrations were an issue that could have effected the accuracy of DIC measurements near the edge of an image. To detect spherical aberrations, a calibration slide was moved from the left most edge of the DIC image to the right most edge of the DIC image. Images were taken at regular intervals of distance. The results of this calibration produced the same measurement between calibration circles and therefore indicated spherical aberrations did not seriously effect measurements.

3.5.2.2 DIC Algorithm Accuracy. The possible accuracy of the DIC software was stated as within one microstrain in the Correlated Solutions manual. However, the accuracy for any specific test condition needed to be validated. A common ability of DIC software was the ability to detect any change in an image, even those that were introduced by digital methods. When a real compression test is run, the real strain is unknown. However, a digitally altered image will be strained exactly the amount specified. To digitally
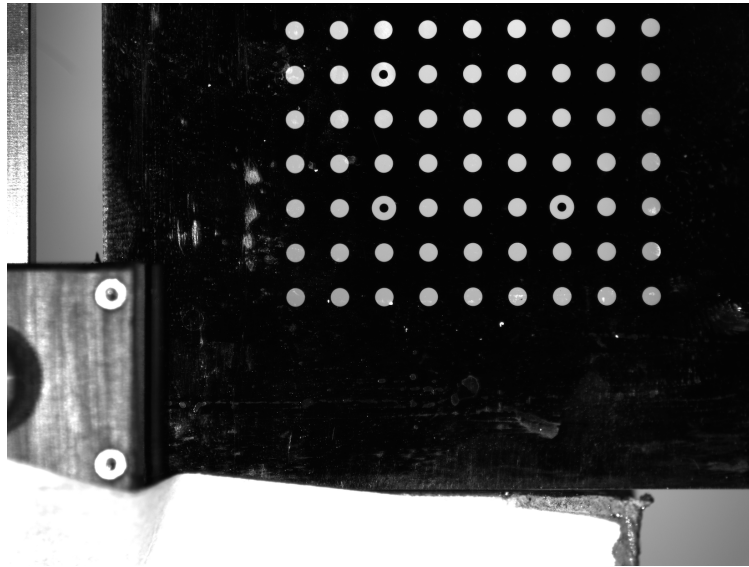
Figure 3.16. Calibration slide viewed in DIC camera: The centers of circles are 3mm apart

strain the images, open-source picture editing software, GIMP (Version 2.6, GIMP.org), was used. The algorithm chosen to strain the images was cubic interpolation. The image was strained in the vertical direction. Strain from the digitally strained images was obtained using the same methods as used for real experiments. These methods are outlined in section 3.5.9.

3.5.2.3 Background Noise. In contrast to the algorithm accuracy, background noise was defined as error in both image measurements and the computation of strain. Background noise from computation was determined by analyzing the same image multiple times in the DIC software. Background noise from the experiment was determined from several images taken of unstrained specimens. Before a compressive strain was applied to the specimen, several images were taken to obtain a reference image for the test. These were also used to measure background noise.

3.5.3 DIC Measurement Optimization

To ensure accuracy of the strain measurements, three things were important:

1. Focus

2. Contrast

3. Low image saturation

Focus was achieved by setting the aperture to the lowest setting, 2.8, and focusing on the specimen being tested. However, before running any compression tests on a particular day, the DIC had been calibrated using a glass slide with a patterned grid. Although this calibration was not used in the analysis for this project, it might be useful and thus it was desirable to keep the calibration constant for all tests run on a day. This meant that the optical zoom could not be adjusted to focus on the specimen. Instead, the camera and specimen had to be in the exact same locations in relation to each other for every test. In practice, only the sample was moved on the compression platens until it was in focus. The entire face of the test specimen had to be in focus so it was necessary to rotate the part until focus of the face was achieved. Additionally, it was known that the face would bow out. Therefore, it would be better if the specimen was at the far end of the focal depth, so that the bowing out would not cause the face to leave the focal depth of the lens. Testing at a 2.8 aperture always resulted in loss of focus due to bowing. Therefore, testing was done at an aperture of 4, where the focal depth was greater.

While the focusing was done by eye, the ability to keenly focus the image was possible without the need for quantification of the focus. This was due to the short depth of field that was used to focus the part versus the greater depth of field used during testing as shown in figure 3.17. This prevented the specimen being observed from becoming unfocused during the test. The calibration slide shown in figure 3.16 was taken at an

aperture setting of 2.8 and also demonstrated the ability to clearly detect focus with the eye. This is because the focus dropped very quickly at the low aperture setting.

Contrast was controlled by adjusting the brightness of two LED lights. Increasing the brightness increased contrast, however, excess brightness caused image saturation. Image saturation caused the DIC strain calculations to be less accurate. Therefore, a balance of contrast and image saturation was needed and the light was adjusted accordingly for each test. Image saturation was also caused by reflections on the face of the specimen. To reduce reflections, the LED lights were placed so that the light came in along the axis of the filaments. Therefore, the lighting was placed to the left and right of the specimen when the filaments were horizontal and placed above and below when the filaments were vertical. Images 3.18 and 3.19 illustrate the impact of the locations of the light sources.

A. Low Aperture   B. High Aperture
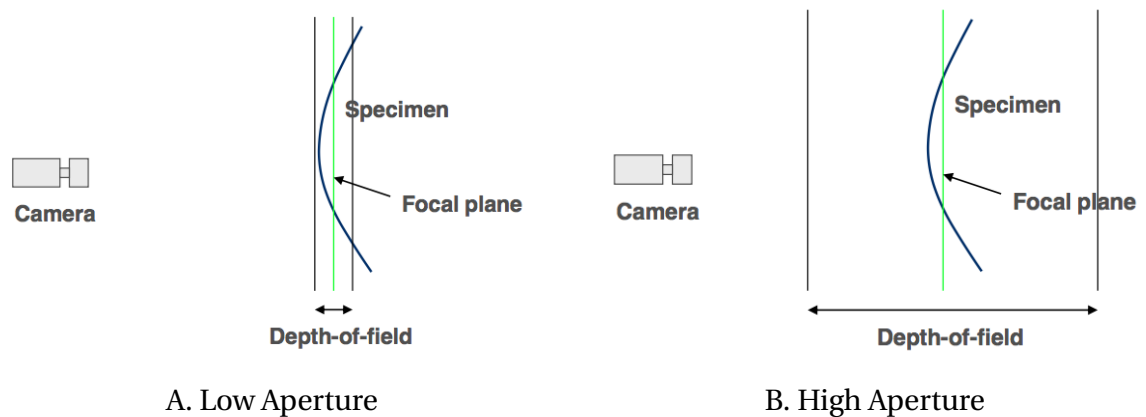
Figure 3.17. DIC- Depth of Field: The depth of field was the area that will look focused when an image was taken. Any object within the depth of field will look focused. A low aperture has a shorter depth of field and thus can be used to focus an image. Switching to a higher aperture then increases the depth of field and ensures that the object will be less likely to leave the depth of field and become unfocused.
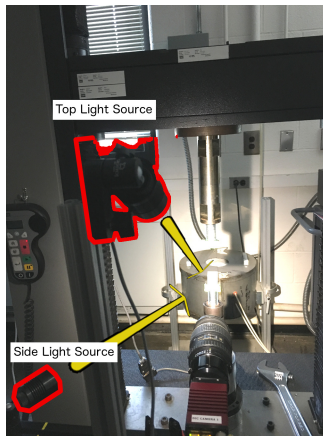
Figure 3.18. Positioning of light sources
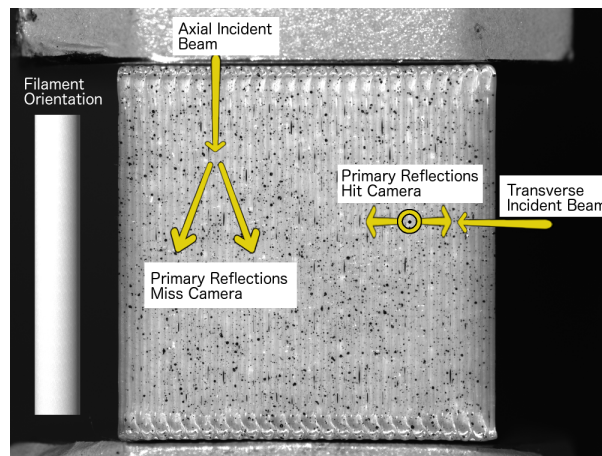
Figure 3.19. Reflectivity with respect to filament orientation

3.5.4 Testing Coordinate System

Compression tests apply a strain rate along a single axis, which was referred to as the axis of compression. This axis forms one part of a three-dimensional cartesian coordinate system used in the experiments. Another axis of the coordinate system was coincident with the optical axis of the DIC camera. The last axis of the coordinate system was parallel to the lens of the DIC camera and to both compression platens. The names of the axes in the cartesian coordinate system were defined in terms of the specimen and thus the name of the axis of compression can change between compression tests.

Since the tests were run along the axis of compression, care needed to be taken to align the desired axes of the FDM part with the axis of compression and axis parallel to the lens of the DIC camera. Three orientations were tested that would be able to reveal all the possible poisson's ratios of an orthotropic material.

Material Axis Aligned with Axis of Compression	Material Axis Parallel to Lens
1	2
2	3
3	1

Table 3.8. Axes Alignment with Axis of Compression and Parallel to Lens Axis
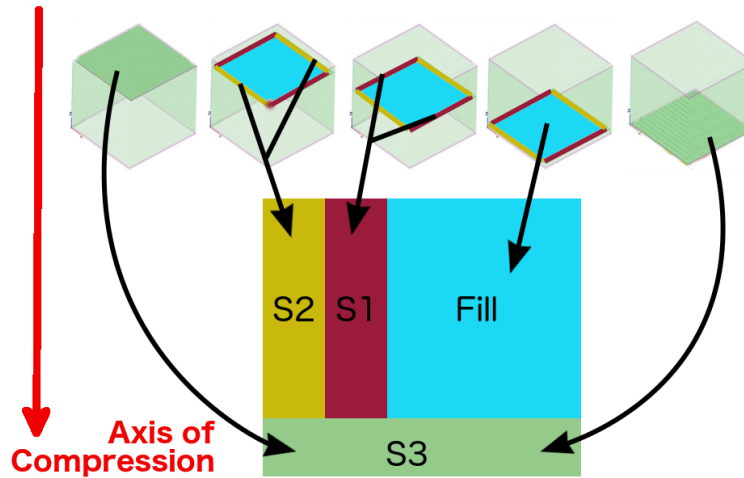
Figure 3.20. Geometry in Axis of Compression Coordinate System: The shell components and fill were all assigned a specific location in the axis of compression coordinate system. The volume and properties of these components could change depending on the orientation of the FDM part in the compression coordinate system.

3.5.5 Geometry Definitions in the Axis of Compression Coordinate System

The geometry of each shell and the fill remained the same in the FDM part coordinate system. One issue when attributing the lengths of this geometry was at the intersections between components. The length of intersections between the vertical shells with normals X and Y were split evenly between both and resulted in equal volumes of each. The intersections between all shells on the top and bottom faces were all considered to be part of the shell with normal Z as shown in figure 3.6.

Component	Length in X (mm)	Length in Y (mm)	Length in Z (mm)
Shell with normal X	3.05	23.87	23.88
Shell with normal Y	23.87	3.05	23.88
Shell with normal Z	25.40	25.40	1.52
Fill	22.35	22.35	23.88

Table 3.9. Shell and Fill Geometry: Each component was a rectangular prism. The side lengths were listed in this table.

Although the shape remained the same, differences in the length and area fractions occurred with a change in orientation. In figure 3.20, S1, S2, and S3 represented a shell and were tied to the axis of compression coordinate system. The figure represented how the parallel or series relationships were formed. Shell normal X, shell normal Y, and shell normal Z, are shells defined in the part coordinate system. The shell from the FDM part that occupied the S1, S2, or S3 location changed when the FDM part was oriented differently in the compression coordinate system. Additionally, the intersections, although very small in volume, had to be assigned properties as well. Their properties depended on location of the intersection in S1, S2, or S3 and adopted the properties of the shell occupying that location. This was the reason different properties were adopted for $E^{S1,S2,S3}$ in table 3.2. The length and area fractions were also effected by the FDM part orientation to the axis of compression.

Fraction	Compression in X	Compression in Y	Compression in Z
α_{S1}	0.1164	0.0564	0.1128
λ_{S1}	0.880	0.880	0.940
α_{S2}	0.0564	0.1164	0.1128
λ_{S2}	0.880	0.880	0.940
α_{S3}	1.000	1.000	1.000
λ_{S3}	0.120	0.120	0.060
α_{fill}	0.8272	0.8272	0.7744
λ_{fill}	0.880	0.880	0.940

Table 3.10. Area and Length Fractions with Respect to Orientation

3.5.6 Test Conditions

The conditions were adapted from the ASTM D695 and D1621-10 standards. The conditions were kept constant to ensure repeatability of the experiment. The environmental conditions were taken from ASTM D695 and include temperature and humidity, since these can alter the mechanical properties of polymers. The crosshead speed was taken from ASTM D1621-10 and kept constant throughout all experiments, since it too can significantly influence the properties of polymers such as ULTEM and ABS. The conditions were shown in table 3.11.

3.5.7 Test Setup

The test setup included a test frame and a DIC system for measuring strain. The test frame was an Instron 1125 with a 100kN load cell. The compression platens were machined from medium-strength grade-5 steel hex screws. The correlated solutions DIC system included a camera, lens, and a computer loaded with the correlated solutions software. The load cell and test frame were interfaced with the DIC system using a National Instruments DAQ with BNC connectors. The load cell was connected to channel 0 and the crosshead displacement to channel 1. The data used for analysis was only taken from the DIC computer. Another computer ran the Instron test frame. The software used to run the Instron test frame was MTS testworks.

Condition	Value
Temperature	60F-80F
Humidity	40-60RH

Table 3.11. Specimen Conditions
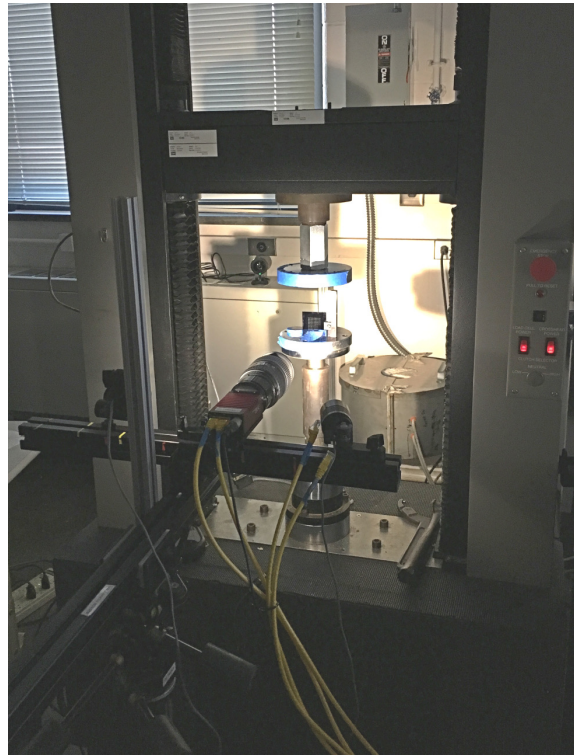
Figure 3.21. Instron and DIC setup

3.5.8 Test Execution

After the focus, contrast, and low image saturation were optimized, the test was started. First, the DIC was set up to start taking images at constant time intervals. The frequency ranged from $\frac{1\ image}{6s} - \frac{1\ image}{4s}$ and was chosen so that 140 images were taken for each test. After the image collection was started, the Instron was set to compress until the user stopped the process. The analog data was recorded on a range -10V to 10V, where 10,000N was equal to 1V.

$$Frequency = \frac{Test\ Duration}{140\ Images}$$

Displacement Rate (mm/min)	Strain Rate (s^{-1})
0.254	Appx. 1.7e-4

Table 3.12. Testing Controls

3.5.9 DIC Image Processing

The compression test collected images and analog data. VIC-2D(Version 6, Correlated Solutions, Irmo, SC) software was used to calculate strains for each image. This process, like the focusing, required a lot of judgement decisions. An area of interest (AOI) had to be selected on the reference image, which defined where the program searched for a speckle pattern in the rest of the images. The reference image was the image taken before the specimen was loaded. It was important to select the whole surface of the cube and nothing else. However, since the AOI was a rectangle, this was sometimes impossible if the image was slightly rotated. Then the AOI was processed for each of the images taken. As described in section 2.9.2 the strain was calculated for each subset of the image. Some parameters could be changed for the processing but for the most part these were kept to the defaults. The DIC parameters were outlined in table 3.13. The subset sizes and step sizes were also varied from 21 to 105 and 5 to 25, respectively. This was done for two nominal mesostructure specimens to identify if there were any inconsistencies coming from the DIC based on what the parameters were.

Parameter	Description
Subset Size	21 Pixels
Step Size	5 pixels
Interpolation	Optimized 4-tap
Interpolation Criterion	Normalized squared differences
Interpolation Subset Weights	Gaussian
Thresholding Prediction Margin	0.02
Thresholding Confidence Interval	0.1
Thresholding Matchability	0.1

Table 3.13. DIC parameters

3.6 Analysis Methods

To evaluate mechanical characteristics, the analysis method attempts to find an objective method for evaluating mechanical characteristics of a specimen. The method accounts for systematic and measurement errors, identifies key components of the stress-strain-time relationship, and chooses a material property that was representative for the specimen and comparable to other specimens. The methods were implemented in the programming language R.

3.6.1 Strain Measurements

The processing of the DIC images produced a strain field for every point in time. As described in section 2.7.3, the macroscopic strain state was the average of the strain field at any point in time. The average was easily obtained in VIC-2D by selecting to extract all strain values. This produced an average strain value for each image and synced it with the recorded time and analog load data for each image.

3.6.2 Converting to Stress

The stress was calculated using equation 3.32, where F was the force in Newtons and A was the area in m^2. The load was recorded as an analog voltage, V, and converted to force using a conversion factor from section 3.5.8. The cross-sectional area was not measured, but taken directly from the CAD model as reported in section 3.4.1. The specimen dimensions were always the same as described in section 3.3.4. Then the stress, σ, was calculated from the analog data using equation 3.33.

$$\sigma \ (Pa) = \frac{F}{A} \frac{N}{m^2} \tag{3.32}$$

$$F = 10000 \frac{N}{V} * V$$

$$A = 0.00064516 m^2$$

$$\sigma \ (MPa) = \frac{1}{0.064516} \frac{MPa}{V} * Volts \tag{3.33}$$

3.6.3 Removing Outliers

Sometimes, the DIC experienced difficulty in correlating the strained image to the reference image. This caused a loss of local strain measurements and in extreme cases some strain measurements came to dominate the averaged strain values, drastically changing the average strain used in stress-strain analysis. However, this does not mean that the next image experienced the same difficulty because strain calculations were made to the reference image, which was the first undeformed image of the test specimen. The poor measurements were captured by finding outliers from the stress versus strain data. The first step was fitting a linear least squares (LLS) model, where the stress was dependent and the strain was independent. Then using this model, the residuals, r, were calculated,

where Y represents the actual values and Y' represents the predicted values.

$$r = Y - Y'$$

The assumption was made that the residuals follow a normal distribution and outliers were defined as the data points (strain, stress), where the residuals were less than 0.3% likely to fit the normal distribution of residuals. This process was done recursively until no more outliers were detected.

3.6.4 Patch Missing Data

The images were taken at a constant frequency, λ, as described in 3.5.8. The real time values, t, for each measurement occured at i times the period, T, where i was an integer.

$$T = \frac{1}{\lambda}$$

$$t_i = i * T \tag{3.34}$$

However, the DIC computer occasionally froze and images would not be taken. Fortunately, the time kept increasing while the computer's other functions were frozen. Therefore, when the computer would start taking images again, the real time of the next measurement would be captured. The real time after the skip would also follow equation 3.34. If a skip occurs for intervals where m was the first index, n the last index (R notation), and all values in the range m to n were a subset of all intervals, i

$$m : n \subset i$$

then, the index j represents the number of skips such that all skips can be represented

by

$$(m:n)_j \subset i$$

where j was the number of skips, then the measurements after the skip would have the

time intervals:

$$t_{n+1} = (n+1) * T$$

The next step was to fill the skips where there was no data using linear interpolation

$$t_{(m:n)_j} = \frac{(m:n)_j - (m_j - 1)}{(n_j + 1) - (m_j - 1)} * (t_{n_j+1} - t_{m_j-1}) + t_{m_j-1} \tag{3.35}$$

This process was extended to the strain and stress vectors

$$\epsilon_{(m:n)_j} = \frac{(m:n)_j - (m_j - 1)}{(n_j + 1) - (m_j - 1)} * (\epsilon_{n_j+1} - \epsilon_{m_j-1}) + \epsilon_{m_j-1} \tag{3.36}$$

$$\sigma_{(m:n)_j} = \frac{(m:n)_j - (m_j - 1)}{(n_j + 1) - (m_j - 1)} * (\sigma_{n_j+1} - \sigma_{m_j-1}) + \sigma_{m_j-1} \tag{3.37}$$

3.6.5 Detecting Fracture

Fracture was detected by normalizing the stress, $\bar{\sigma}$, and strain,$\bar{\epsilon}$, vectors

$$\sigma_{Norm} = \frac{\bar{\sigma}}{\sigma_{max}}$$

$$\epsilon_{Norm} = \frac{\bar{\epsilon}}{\epsilon_{max}}$$

and then computing the distances between each ordered set of points $(\epsilon, \sigma)_i$

$$d_i = |< (\epsilon_{i+1} - \epsilon_i, \quad \sigma_{i+1} - \sigma_i >| \tag{3.38}$$

The first $d_i > 2 * avg(d)$ was identified as the index of fracture. The UTS was defined as the index of highest stress up to fracture. Subsequent analysis was only on the $(\epsilon, \sigma)_i$ where $i \leq UTS$.

3.6.6 Calculating Tangent Modulus

When the rule of mixtures was applied, the strain was assumed to be constant throughout the FDM part. When we increase the amount of voids, the filaments were still being strained the same amount. The change in effective modulus was due to the change in perceived stress $\sigma = \frac{F}{A}$. Therefore, the strain in an FDM part was the same for any build style and a tangent modulus can be taken at the same strain for all FDM parts made from the same material and tested using the same procedure. To define the tangent modulus an initial data point was identified as s. This point was defined as the first point on the stress-strain curve where $\epsilon > 0.5\% strain$. Then the data used to calculate tangent modulus was $(\sigma_s, \ldots, \sigma_{s+9})$ and $(\epsilon_s, \ldots, \epsilon_{s+9})$. A LLS model was fit to these data points and used to report tangent modulus.

3.6.7 Finite Element Method

Finite element modeling was done in Abaqus. The specimen was modeled as an isotropic solid with properties equivalent to that of bulk ULTEM 9085. The compression platens were modeled as low carbon steel. The interface between the platens and specimen was assigned to have a coefficient of friction of 0.24. This friction coefficient was taken from ULTEM Resin 4000 data sheet (Sabic IP, Houston, TX) because the data was not available for ULTEM 9085 or from Stratasys. The lower compression platen was fixed and a constant velocity was applied to the top compression platen. The specimen consisted of a

cubic hex mesh with one million nodes. The velocity was equivalent to 0.254mm/min. The test was run for 500s and the state of the system was computed for every 10s.

3.7 Failure Analysis

Failure was defined two ways: significant cracking resulting in inability to carry load or as extensive plastic deformation. The type of failure observed was attributed to anisotropy, mesostructure, and testing conditions.
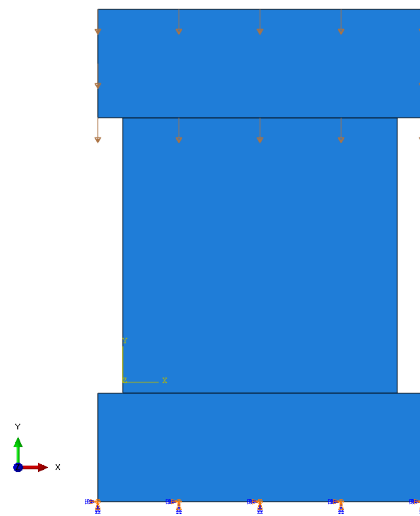
Figure 3.22. The theoretical compression test was run in Abaqus. Several view methods were available, including one that shows the boundary conditions imposed on the model. The top and bottom rectangular cuboids were the compression platens and the cube in the middle was the specimen. The arrows on the top platen indicate a defined velocity in a single direction. The arrows on the bottom platen indicate that the bottom platen was constrained in all directions.

3.7.1 Local Plastic Strain

The strain fields calculated by the DIC were used to show the local strains leading up to failure. In addition to indicating failure, plastic strain was also observed with the DIC when the specimen was unloaded.

3.7.1.1 Residual Strains. The first type of plastic strain that was observed was residual. These strains occurred after a test that was run to failure and then unloaded. The residual strain maps showed that while some areas unloaded, others were left plastically strained. Since all of the tests covered in section 3.3 were run to failure, there was a lot of residual data.

3.7.1.2 Cyclic Strains. Cyclic plastic damage was another type of plastic strain that could be observed with DIC analysis. Cyclic tests were conducted on two specimens from group 8, with a mesostructure as defined in table 3.6. The cyclic tests were conducted along the X axis of the specimens. Three cycles per specimen were run to a load of 7kN.

3.7.2 Sectioning Test Specimens

In order to relate the observed plastic strain to the mesostructural damage, the test specimens had to be sectioned. This was achieved with a high speed saw and coolant because the lower speed saws without coolant introduced heating that destroyed the mesostructure. The high speed saw used was the TechCut 5 precision high speed saw produced by Allied High Tech Products, Inc. (Rancho Dominguez, CA, USA). The saw utilized a carbide blade. Specimens were cut in half once, and the DIC face was kept intact. Only specimens with residual strains were sectioned.

3.7.2.1 Imaging Test Sections. Mesostructural damage was imaged using a Keyence VHX 5000 (Osaka, Japan). The optical microscope took images at different focal depths and generated a 3D image that showed cracking in the mesostructure.

4 Results

This section validates the DIC measurements and compares the stiffness and mass models to the experimental data. The foundation of the models was a description of the mesostructure derived from the CAD model. The experimental data was obtained for real FDM parts with multiple mesostructures. Two of the CAD model parameters, air gap and raster angle, were changed to produce different mesostructures. The models try to predict how the stiffness and mass of real FDM specimens change with the CAD model parameters. Additionally, a qualitative analysis of deformation and failure of the mesostructure is studied using real images and micrographs of FDM parts.

4.1 Mass Model

The air gap volume fraction method was derived from the number of filaments in an RVE, which was defined by the designer of an FDM part using the air gap process variable. The mass model was the most direct method of observing the volume fractions in real FDM parts. Therefore, the mass model was employed to validate the volume fractions model.

Each of the specimens was a 25.4mm cube, but it was observed that different mesostructures resulted in changes to the mass of a cubic test specimen. The differences between different mesostructures were further clarified by the similarity of the masses for specimens with the same mesostructure. For each group of specimens with the same mesostructure, the largest standard deviations were ±0.1g, which represented about one hundredth of total mass. More commonly, the standard deviations represented only one thousandth of the total mass.

The mass model developed for FDM parts was derived from the volume fraction method, which attempted to describe the volume in terms of the number of filaments present. The number of filaments was taken directly from the CAD model. Additionally, the CAD model defined the width and height of filaments. Therefore, it was assumed these filaments kept the same properties. The model is compared to experimentally determined masses of the FDM specimens in figure 4.1. The masses of real specimens mostly follows the trend predicted by the mass model. However, the model does not

Group	ϕ (Degrees)	g (in)	Material	Mass (g)	Mass St. Dev. (g)
S	0.00	0.00	ABS	16.02	0.01
2	45.00	0.02	ABS	10.15	0.00
3	13.18	0.04	ABS	8.68	0.02
4	13.18	0.00	ABS	14.17	0.00
5	76.82	0.00	ABS	14.15	0.00
6	45.00	0.05	ABS	8.26	0.01
8	0.00	0.02	ABS	10.00	0.10
9	45.00	0.02	ABS	10.12	0.09
0000	0.00	0.00	ULTEM	18.83	0.02
0400	0.00	0.04	ULTEM	10.26	0.01
0445	45.00	0.04	ULTEM	10.29	0.00

Table 4.1. Masses of Specimen Groups: The variable definitions are given in table 3.1

capture the drop in mass observed when the raster angle is increased and the air gap remains $0.00mm$.

4.2 Utilizing Digital Image Correlation

The method for obtaining data in this project was compression testing on an Instron screw-driven frame coupled with Digital Image Correlation that acquired images of the FDM parts at a defined frequency. The methods used to obtain A raw DIC image before DIC analysis is shown in 4.2.
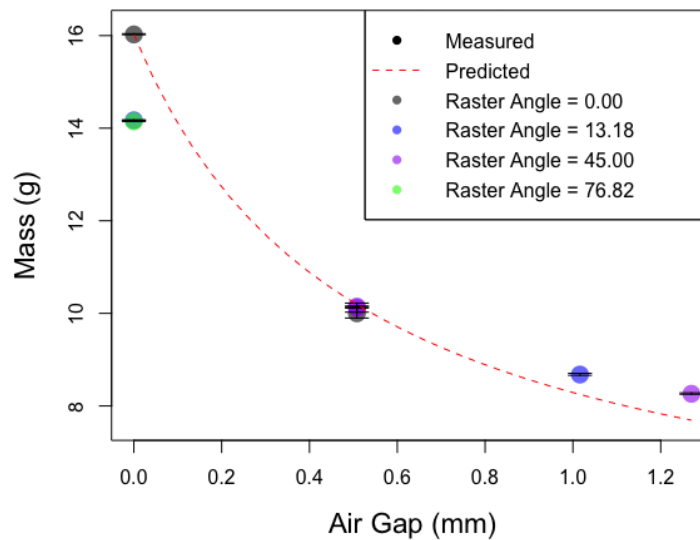
Figure 4.1. Mass of ABS Specimens: The real masses mostly follow the trend predicted by the mass model. However, a clear shift is observed when a raster angle is introduced at an air gap of $0.00mm$, which is not captured by the model. The error bars on each of the data points show there is little uncertainty in the experimentally measured data.
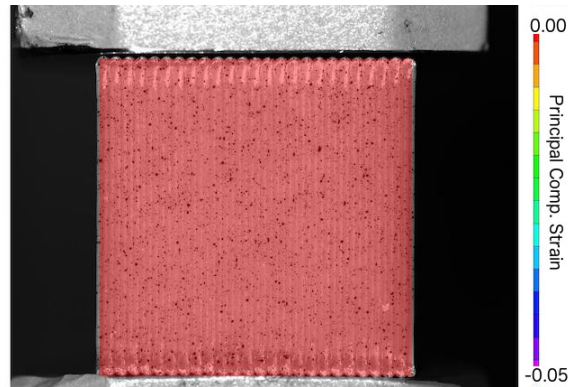
Figure 4.2. Raw DIC Image: These images contained the strain information from the compression test. However, DIC software is needed to compute the strains from the raw image data. The specimen in this image is 0000E. The axis of compression is X and the transverse direction is Y.

4.2.1 Processing Images

The raw DIC images had a resolution of 3296×2472 pixels. The specimen occupied a region approximately 1590×1590 pixels. DIC software was used to determine a strain field for each image. This was accomplished by computing the affine displacement field for every subset size of 21×21 pixels. The centers of the subsets were spaced 5 pixels apart. This resulted in approximately 100,000 calculations of displacement fields per image. Once affine displacement fields were calculated, the Lagrangian strain fields were calculated. The DIC software allows the user to display the following strain fields e_{xx}, e_{yy}, e_{xy}, where the directions were defined as the coordinates of the image, as well as the principal strains values and vectors. The principal strains represented the compression coordinate system strains. The compressive principal strain field is shown in figure 4.3. The strains in the axis of compression coordinate system were then translated to the material coordinate system. In figure 4.3, the compressive principal strain would represent strain along the X axis of the FDM part. Also shown in figure 4.3, the bottom platen remains stationary, so the strain is inhomogeneously distributed through out the cube.
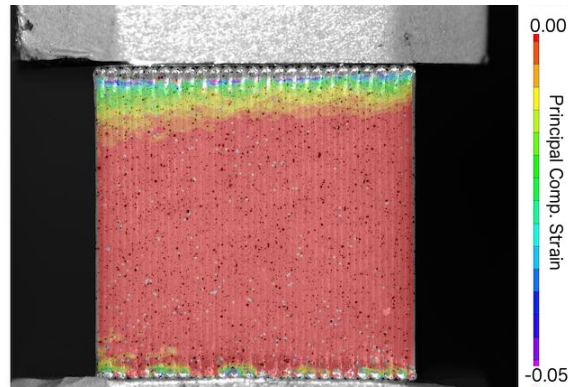
Figure 4.3. Strain Map During Compressive Loading: After DIC analysis, the strain field was computed across the speckle pattern available in the raw image. The specimen in this image is 0000E. The axis of compression is X and the transverse direction is Y.

4.2.2 Algorithm Accuracy

The accuracy of DIC analysis was validated by artificial applying strain to a raw DIC image. Artificially straining a raw DIC image involved resizing it using an interpolation algorithm. After running DIC analysis on the artificially strained images, the strain maps revealed that DIC was able to capture the artificial strain.

By artificially straining an image, the exact applied strain was known. Strain was applied in the vertical direction a total of three times to produce three new images. The reference image was include in DIC analysis for a total of four images. DIC analysis measured the strain of each of the artificially strained images in relation to the reference image. The comparison of the actual artificial strain to the DIC measurements of strain are presented in table 4.2.

Figure 4.5 indicates that the precision of the calculated strain does not decrease with increasing strain above 2 millistrain.

A. 0.24% Strain axis   B. 1% Strain
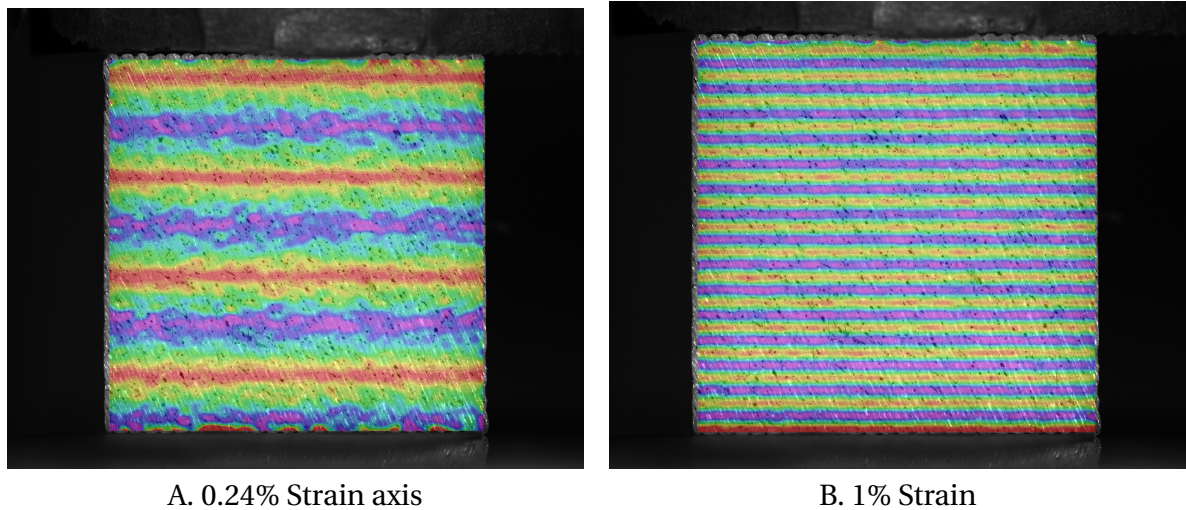
Figure 4.4. Digitally Strained DIC Images: Images strained by cubic interpolation using GIMP software show the ability of DIC software to detect the digitally strained image. Purple indicates higher strain, green is medium strain, red is no strain. A small strain of 0.24% shows significant amounts of red, indicating little to no strain. A higher strain of 1% shows the higher amount of purple and no red. The specimen in this image is 10B. The axis of compression is X and the transverse direction is Y.

Image	Artificial Strain- Actual (millistrain 10^{-3})	Strain- DIC (millistrain 10^{-3})	Difference (millistrain 10^{-3})
Reference	0.00	0.00	0.00
1	1.21	1.21	0.001
2	2.39	2.43	0.037
3	10.0	10.1	0.104

Table 4.2. Artificially Applied Strain and DIC Computed Strains

4.2.3 Inherent Noise

There is inherent "noise" in the values of strain as a function of the 1) the strain calculation method inherent to the software and 2) the noise in the images. The computational noise was assessed by calculating "strain" between the reference image and the same image, while the image noise due to the imaging methods was assessed by calculating
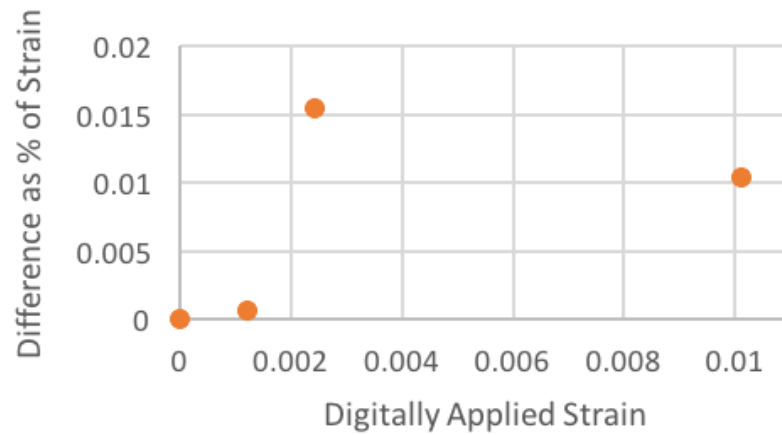
Figure 4.5. Difference as a Percent of Strain: The difference as a percent of strain is an effective method for assessing the difference between digitally applied and DIC computed at higher strains.

"strain" between multiple images acquired of the same unstrained cube. The DIC analysis was run with a subset size of 21 pixels and a step size of 5 pixels.

4.2.4 Subset Size

The optimum subset and step size for DIC analysis needed to determined based on the strain field values and computational efficiency. Table 4.4 enumerates how the computational time changes with changing analysis parameters. The strain fields produced by a larger subset and step size were much smoother than those produced with smaller

Type of Noise	Noise Threshold	Observed Images
Computational Noise	$< 10^{-7}$	4
Image Noise	$< 10^{-4}$	50

Table 4.3. Computational and Image Noise: The noise was established by running DIC analysis on unstrained images. Computational noise consisted of running DIC analysis on the same image, while image noise consisted of running DIC analysis on several images taken of an unstrained cube. The DIC analysis was run with a subset size of 21 pixels and a step size of 5 pixels.

subsets. Additionally, when the subset and step were large, there were less strain points and strain was calculated much faster. The small subset size had the advantage of showing local deformations and variations in the strain field. Although the small and large subset sizes produced very different strain fields, the average strain measurements remained remarkably similar. This indicates that the homogenization method of averaging local strains across a macroscopic part is clearly applicable to FDM parts.

Subset Size (Pixels)	Step Size (Pixels)	Average Computational Time (min)
21	5	~25
42	10	~20
63	15	~15
84	20	~10
105	25	~5

Table 4.4. Subset Sizes: The step size was approximately a quarter of the subset size. As the subset and step size increased, the computation time dropped. However, the resolution of the strain field was impacted.
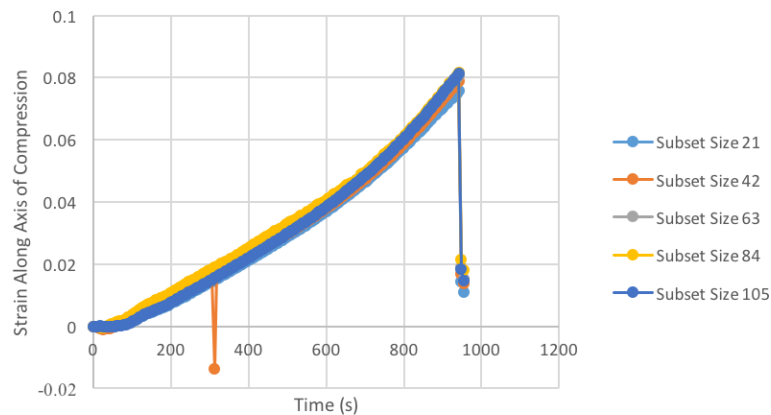
Figure 4.6. Impact of Subset on Strain Computation: Specimen 0000E was compressed along the X axis and the Y axis was defined as the transverse axis. The DIC analysis was run multiple times with different subset and step sizes. The strain time-series are compared for each subset and step size.

4.3 Analysis of Mechanical Response

Mechanical response was assessed from the experimental stress and strain data. The stress data was calculated from the analog load data logged during the compression test and the cross-sectional area defined in the CAD model. The strain data was obtained through the DIC analysis of each raw image. The DIC acquired approximately 140 images for each compression test. According to the methods outlined in 2.7.3 the macroscopic strain state was the average of all strain data points across the field. The stress and strain values for each image were synced using the time stamp.

The property chosen to represent the mechanical response was a tangent modulus. The results are organized to show how the tangent modulus was calculated in practice and the precision of this method. The final precision of the tangent modulus property represented the variability in stiffness of an FDM part and also the variability of the methods used to calculate tangent modulus.

The tangent modulus was also modeled as a response to the mesostructural design variables and geometry. The model was developed for three orthogonal directions of an FDM part. The model is compared to experimental results from specimens created with the same geometry but various mesostructures.

4.3.1 Tangent Modulus

The starting point for calculating the tangent modulus was the stress-strain plot. Each plot has approximately 140 data points, since there were 140 recordings of raw images and analog data. A tangent modulus was calculated for each specimen starting at a specific strain. For the ULTEM dataset, this strain was 0.5% and for the ABS dataset, the

strain was 1%. Figure 4.7 shows where the tangent modulus is calculated on a nominal ULTEM sample.

4.3.2 Measuring Nominal Values

Before the constitutive equations can be solved, the nominal values need to be determined. This involved measuring several cubes with no raster angle, no air gap, and no shell. Results for these measurements are given in table 4.5

4.3.3 Precision of Tangent Modulus Measurements

Precision was determined as the standard deviation of the tangent modulus calculation. The tangent modulus calculation was developed in section 3.6.6 and evaluated for
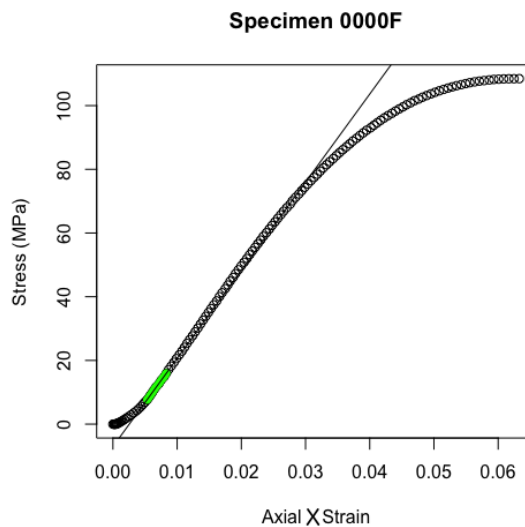
Figure 4.7. Stress-Strain Curve: This plot was generated from the strain, which was obtained through DIC analysis, and the stress, which was obtained from the analog data. The toe was attributed to the displacement controlled test. The green region was identified using an algorithm where the straight line is fitted to calculate a tangent modulus. Specimen 0000F was compressed along the X axis and the Y axis was the transverse axis.

Material	Property	Mean (MPa)	StdDev (MPa)	Number Samples	Group
ABS	E_1^0	2091	92	2	S
ABS	E_2^0	2251	NA	1	S
ABS	E_3^0	1949	30	2	S
ULTEM	E_1^0	2848	57	5	0000
ULTEM	E_2^0	2666	300	5	0000
ULTEM	E_3^0	2290	34	5	0000

Table 4.5. Nominal Stiffness Measurements

three directions of all ULTEM specimen groups. The precision of the tangent modulus was determined from specimens that were strained in the same direction and had the same mesostructure. At least 4 specimens were considered for each precision measurement, where the precision measurement applied to a particular mesostructure and axis of compression. It was shown that the precision of the tangent modulus remained within ±5% for all specimen groups except for the nominal modulus of the Y axis.

4.4 FDM Modeling

Constitutive equations were developed in section 3.2 that related the mesostructure to stiffness. The mesostructure was defined in terms of the process variables and the stiffness was represented by a uniaxial tangent modulus along one of the axes of the macroscopic coordinate system. Therefore, there were three models that described any mesostructure as described in equations 4.1, 4.2, and 4.3.

Group	Axis of Compression	Tangent Modulus Mean (MPa)	Tangent Modulus Std. Dev. (MPa)
0000	X	2848	57
0000	Y	2666	300
0000	Z	2290	34
0400	X	935	22
0400	Y	488	24
0400	Z	851	18
0445	X	928	26
0445	Y	871	40
0445	Z	682	12

Table 4.6. Precision of Tangent Modulus Measurements: The mean and standard deviation of the tangent modulus was established for each of the groups in the ULTEM specimen set. The process variables and number of specimens for each group were defined in table 3.6.

$$E_X^{fill} = \left(\frac{w}{w+g}\right)\left(\frac{\phi}{180°}\right) \times E_1^{nom} \tag{4.1}$$

$$E_Y^{fill} \begin{cases} 0 & \phi = 0° \ \& \ g > 0mm \\ E_2^{nom} & \phi = 0° \ \& \ g = 0mm \\ \left(\frac{w}{w+g}\right)\left(\frac{\phi}{180°}\right) \times E_1^{nom} & \phi > 0° \ \& \ g > 0mm \\ Not\ Defined & \phi > 0° \ \& \ g = 0mm \end{cases} \tag{4.2}$$

$$E_Z^{fill} = \frac{w}{w+g} \times E_3^{nom} \tag{4.3}$$

However, the real test specimens were FDM parts composed of multiple components, each with their own mesostructures. The components were parallel or in series to each other along each of the axes of the FDM part coordinate system. Therefore, the macroscopic stiffness model could predicted tangent modulus along the axes using equation 4.4. The mesostructure of the three shell components remained the same for each test, only their orientation to the axis of compression changed. However, the

mesostructure of the fill changed between test specimens. Therefore, the change in the effective tangent modulus, E^{eff}, was due to the changes in the fill.

$$E^{eff} = \cfrac{1}{\cfrac{\lambda_{S1}}{\alpha_{S1} \ E^{S1}} + \cfrac{\lambda_{S2}}{\alpha_{S2} \ E^{S2} + \alpha_{S3} \ E^{S3} + \alpha_{fill} \ E^{fill}}} \qquad (4.4)$$

4.4.1 Direction X

In the X axis, the constitutive model predicts that the increase in air gap causes a non-linear decrease in the tangent modulus, which is seen as the curve of the surface along the blue plane in figure 4.8. Additionally, low raster angles that result in many different orientations of layers were predicted to drastically reduce the tangent modulus. In contrast, raster angles, such as 0° and 90°, that produce many layers oriented along the X axis were predicted to produce the mesostructure with the highest tangent modulus. The model also assumed that layers with a positive air gap and oriented in a direction other than the loaded X axis, did not contribute to the tangent modulus. The model is defined as the change to the nominal mesostructure. Therefore, the nominal tangent modulus is the anchor for the model and does not indicate its accuracy.

When the raster angle is zero, and the air gap is changing, the model predicts an X axis tangent modulus that is higher than the experimental value. However, when the raster angle is positive, the model predicts X axis tangent moduli that are lower than the experimental value. This occurs in both the ABS and ULTEM datasets.

4.4.2 Direction Y

In the Y axis, the model is identical to the X axis model except for the zero raster angle case. This is demonstrated by the same consistently under predicted tangent moduli
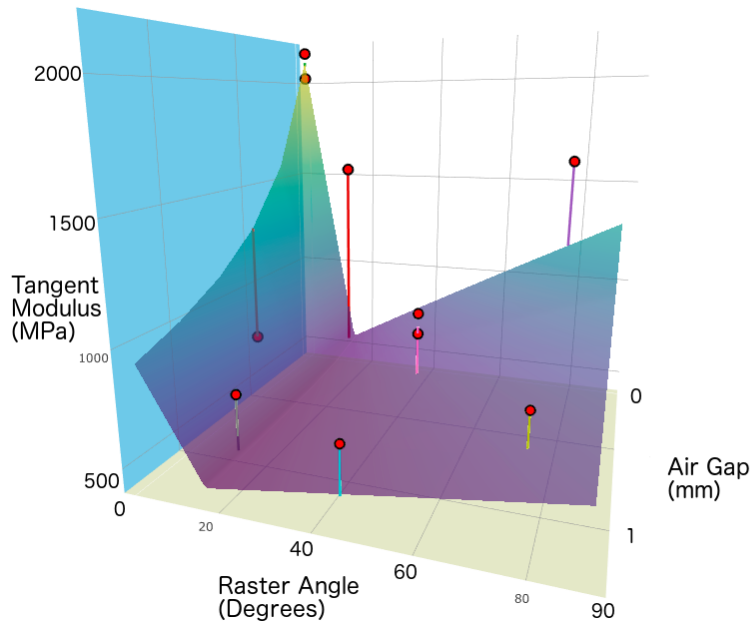
Figure 4.8. Tangent Moduli of ABS- X axis: The plane represents the model and the red points represent real measurements. The independent variables are air gap and raster angle, which are process variables defined in the FDM CAD model.
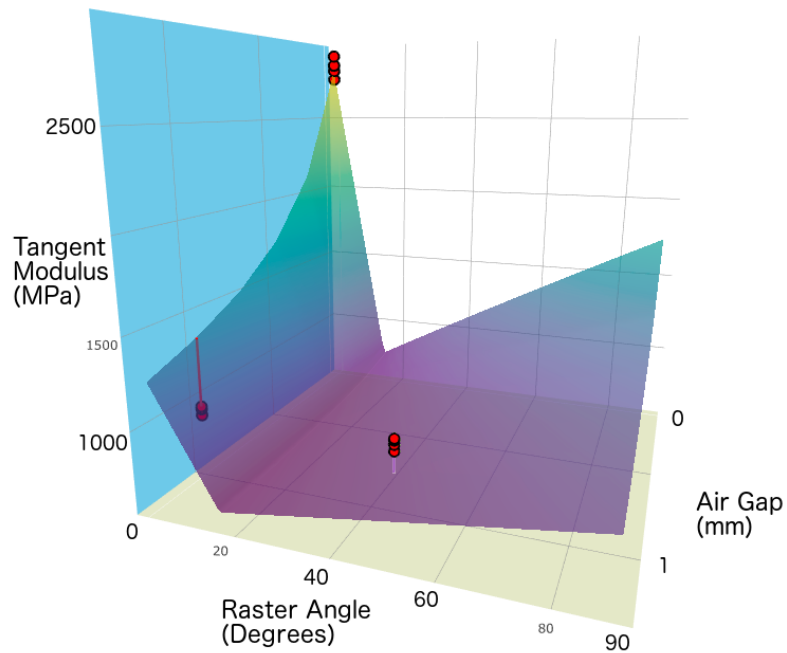
Figure 4.9. Tangent Moduli of ULTEM- X axis

when the raster angle is positive as was seen for the X axis model. However, when the raster angle was zero, the model predicted that the fill of an FDM part had no stiffness and only the shell contributed to the overall tangent modulus. The shell shared the same mesostructure and tangent modulus with the nominal structure, however, the shell was much thinner. The model accounted for the reduction in cross-sectional area. When the raster angle was 0, the difference between the predicted Y axis tangent modulus and measured Y axis tangent modulus was less than 10% of the total tangent modulus. This was the same for both ABS and ULTEM and can be seen in figures 4.10 and 4.11.

4.4.3 Direction Z

In the Z axis, the model predicts tangent modulus is exclusively a function of air gap. This is the same model as seen in the X axis, when there was no raster angle. Again, when relying exclusively on the volume fraction method, the model over predicts what
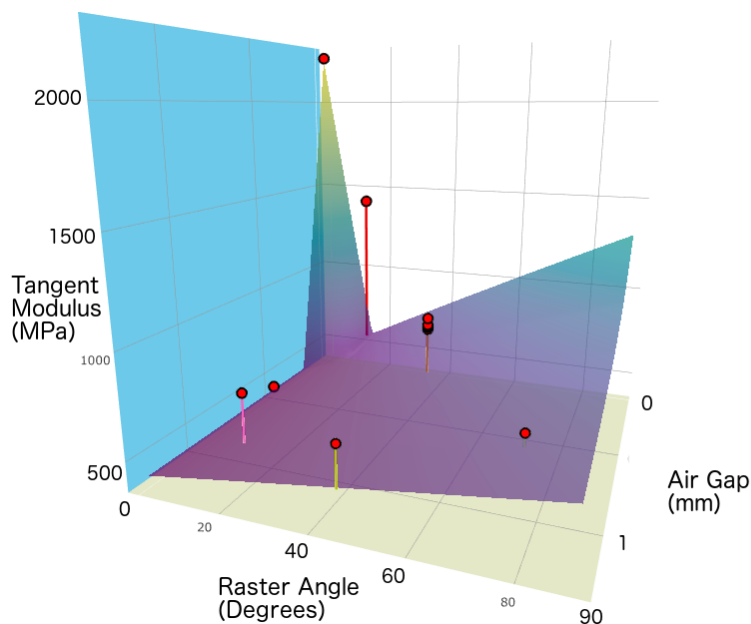
Figure 4.10. Tangent Moduli of ABS- Y axis
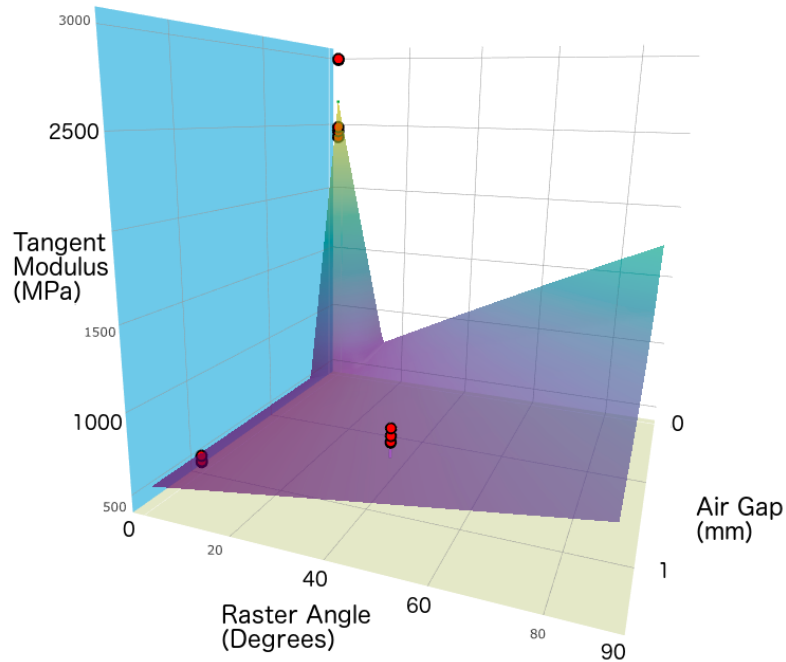
Figure 4.11. Tangent Moduli of ULTEM- Y axis

the real tangent modulus of an FDM part will be. This is also seen for both the ABS and ULTEM datasets.

4.4.4 Regression Model

Although the constitutive models were different for each direction, the trends in the experimental data looked to be relatively consistent as shown in figure 4.14. Additionally, the major influence on the experimental tangent modulus seemed to be coming from the air gap and not the raster angle. To quantitatively analyze these observations, a regression analysis was conducted on the experimental data. The data was analyzed and visualized simultaneously by normalizing it. Normalization was carried out by dividing the tangent modulus in a particular direction by the corresponding nominal modulus.
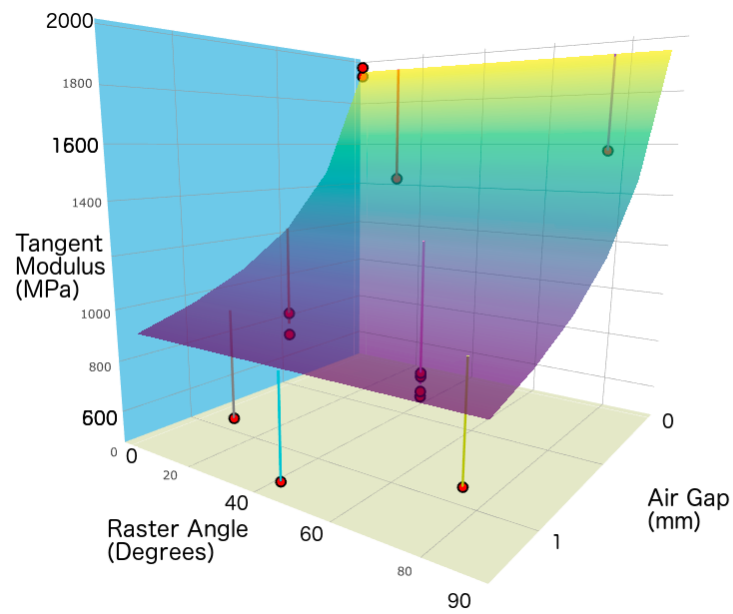
Figure 4.12. Tangent Moduli of ABS- Z axis
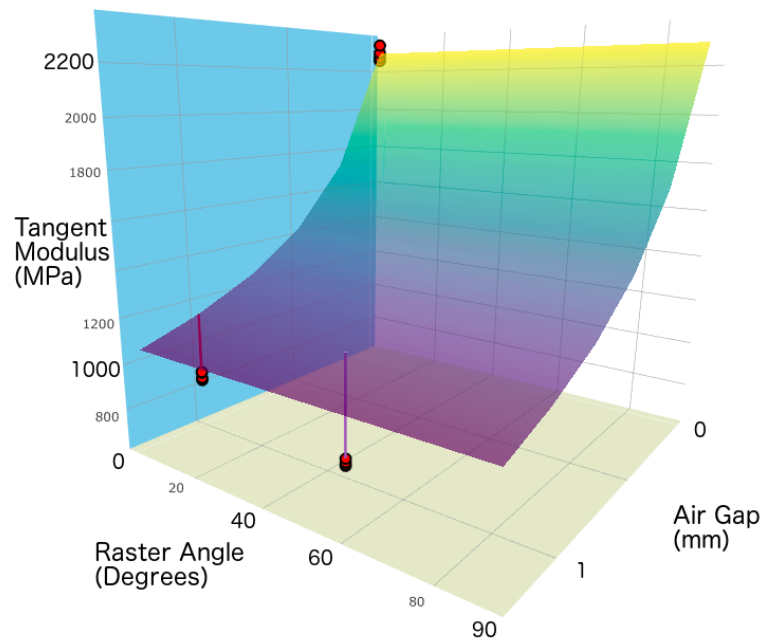
Figure 4.13. Tangent Moduli of ULTEM- Z axis

For example, a measured X axis tangent modulus would be divided by the X axis nominal modulus.

The regression analysis used a function of the form given in equation 4.5, with weights given in table 4.7. The weights show that the fitted function predicts a similar impact from the air gap and raster angle as the constitutive model. However, the weights are lower than are suggested by the constitutive model. It is important to note that the regression did use a function that was similar to the constitutive model, so it is natural that it would look similar. However, the regression analysis weights keep the same sign; even more, the regression surface keeps the same shape as the constitutive model for a dataset that includes all three orthogonal directions.
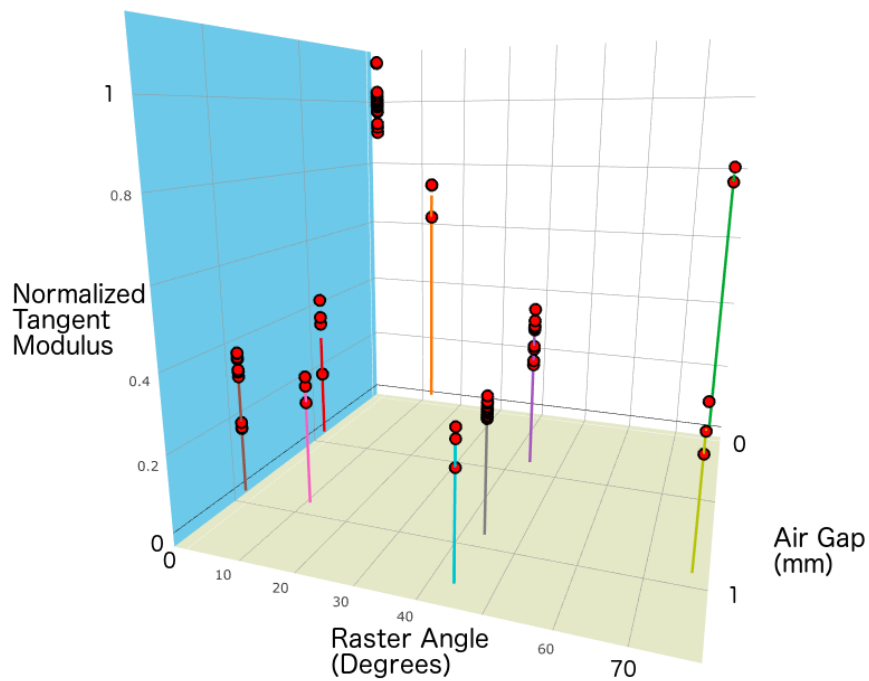
Figure 4.14. Normalized Tangent Moduli: The experimental tangent moduli could be visualized in a single plot by normalizing them.

$$E_{norm} = a \cdot \phi + b \cdot exp(c \cdot g) \tag{4.5}$$

	Estimate	Std. Error
a	8.95e-04	4.26e-04
b	0.61	0.03
c	-20.86	1.96

Table 4.7. Regression Weights
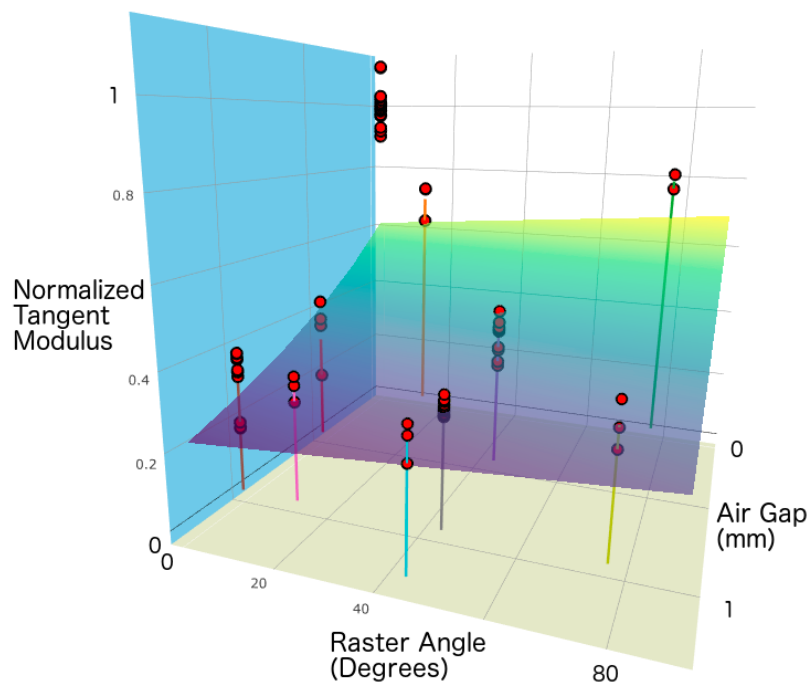
Figure 4.15. Regression of Normalized Tangent Moduli: The regression reveals a trend in the tangent moduli data that is similar to the constitutive models, but is less weighted.

4.5 Strain Distributions

In addition to taking the average strain, the data in the DIC images was used to reveal local strains. These could reveal strain anomalies such as an area of strain accumulation, as shown in figure 4.16. However, the indication of damage does not alone tell the story of how the FDM part acquired damage. Additional information, such as cyclic loading and micrographs, was used to further tell the story of how local strain accumulation led to damage and failure in FDM parts.

4.5.1 Residual Plastic Strain

A cyclic test loaded FDM parts to a stress of 10.5MPa, approximately 75% of the yield strength. Figure 4.17 shows the DIC strain maps of specimens that were loaded elastically and then unloaded. The unloaded images reveal that specimens retained residual strain after being unloaded, although they were loaded elastically. This residual strain remains even after the specimens were allowed to relax for two minutes.

Figure 4.16. Concentrations of Strain on the Surface of Specimen: Specimen 0000N was compressed along the Z axis and X was defined as the transverse.

A. No cycles- Reference Image

B. No cycles- Background noise

C. 1 cycle- No relaxation

D. 1 cycle- Two minutes relaxation

E. 2 cycles- No relaxation

F. 2 cycles- Two minutes relaxation
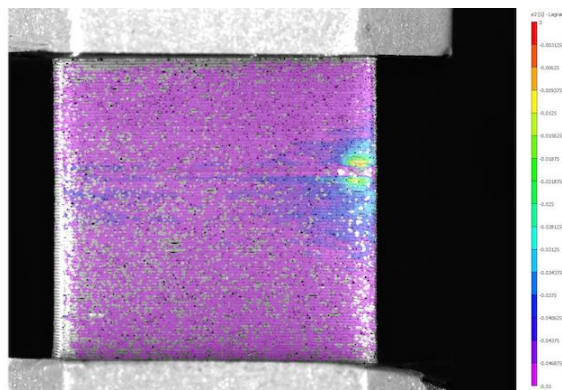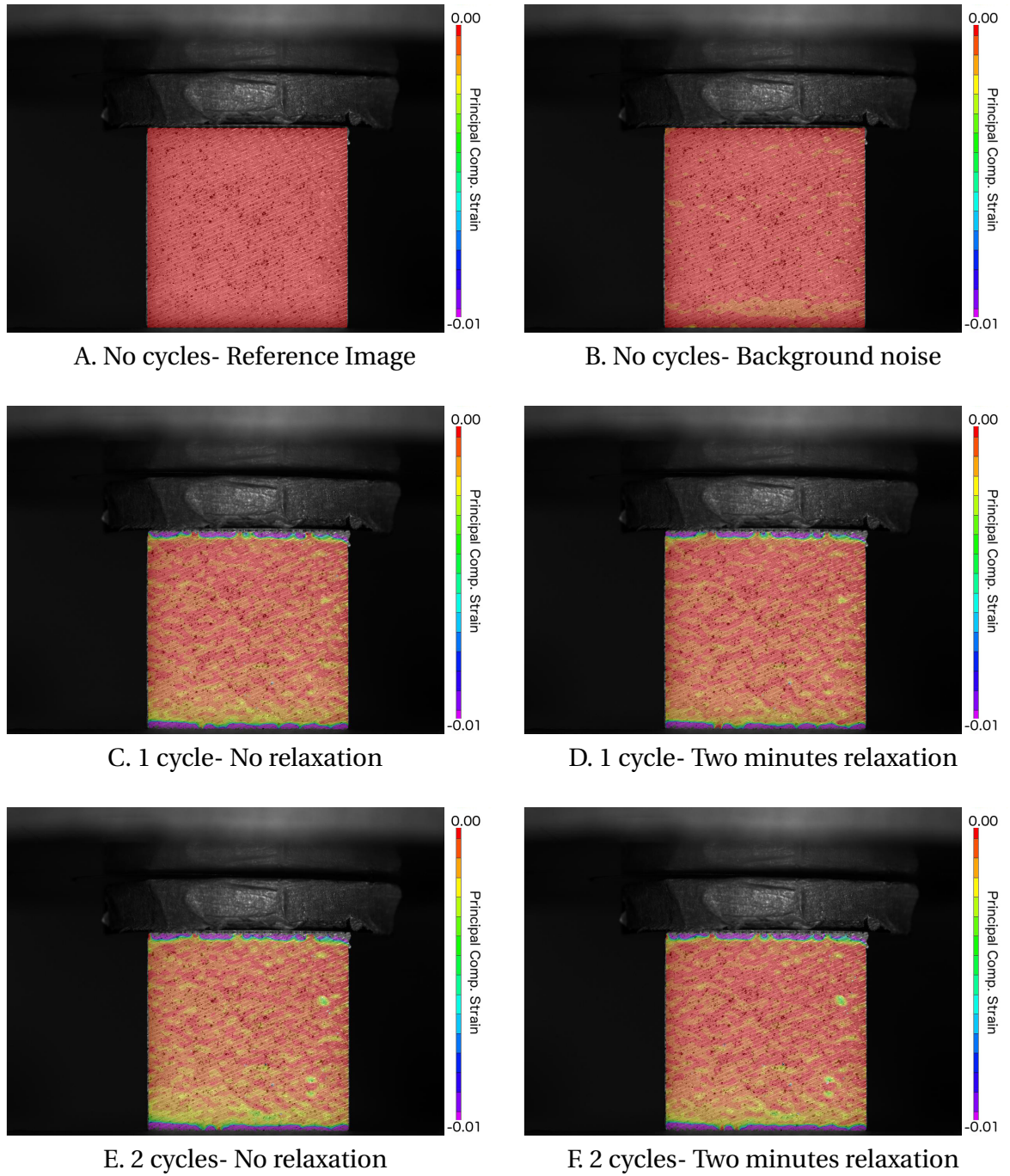
Figure 4.17. Cyclic FEM strain maps show the evolution of residual strain over time. Each of the images shows the residual strain of unloaded specimens that have been loaded cyclically. Specimen 8D was strained in the X direction and Y was the transverse.

The accumulation of cyclic strain was quantified by averaging the strain map for each of the analyzed DIC images. The strain after each cycle is shown in figure 4.18. In figure 4.19, the majority of residual strain was accumulated after the first cycle. The change in residual strain for subsequent cycles was less than the initial change in residual stress.

4.5.2 Strain Field Variations

During compression it was noticed that the strain fields seemed to be most concentrated along diagonals. Additionally, these diagonals were often the leading cause of failure of FDM parts.

The failure associated with the diagonal concentration of strain involved a sudden crack that evolved along the entire diagonal of the part. Observing the complete part, it
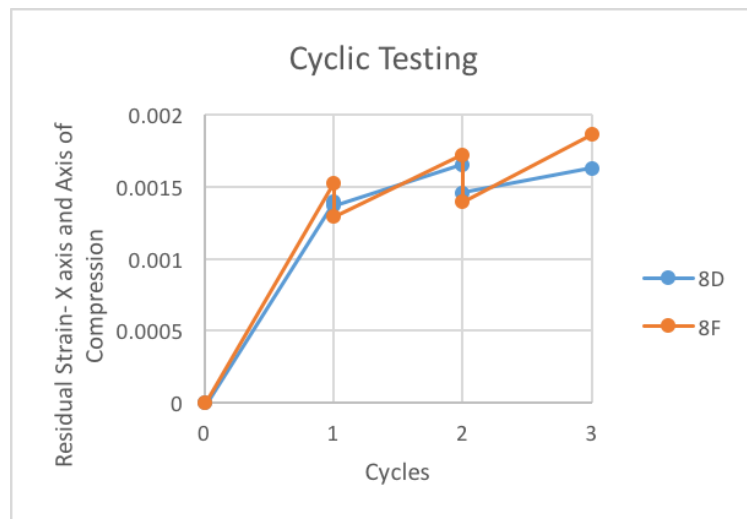
Figure 4.18. Cyclic Strain Accumulation: Two samples were loaded to a stress of 10.5MPa for three cycles. The residual strain was recorded after the samples were unloaded. The residual strain was measured immediately after unloading and again after two minutes.majority of the plastic strain was observed after the first cycle and resilience to additional plastic strain was observed in the following cycles.
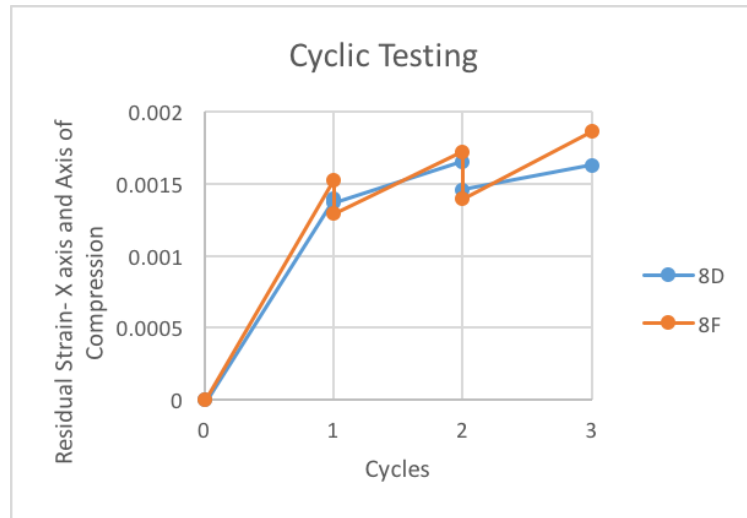
Figure 4.19. Cyclic Strain Accumulation: Two samples were loaded to a stress of 25MPa for three cycles. The residual strain was recorded after the samples were unloaded. The residual strain was measured immediately after unloading and again after two minutes.majority of the plastic strain was observed after the first cycle and resilience to additional plastic strain was observed in the following cycles.
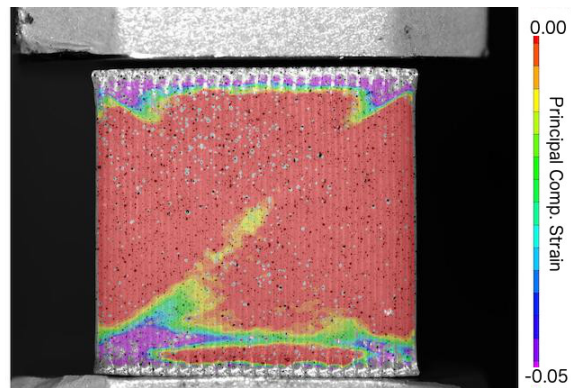
Figure 4.20. Residual Strain Along Diagonal

looked as if the top and bottom of the FDM part had separated and the top was sliding diagonally down the bottom. This was characterized by a bending of the shell, which did not crack. Upon closer inspection, it could be seen that unlike the shell, the fill mesostructure had cracked.

A. Failure by splitting
Specimen 0445C loaded along X axis

B. Failure along diagonal
Specimen 2A loaded along Y axis
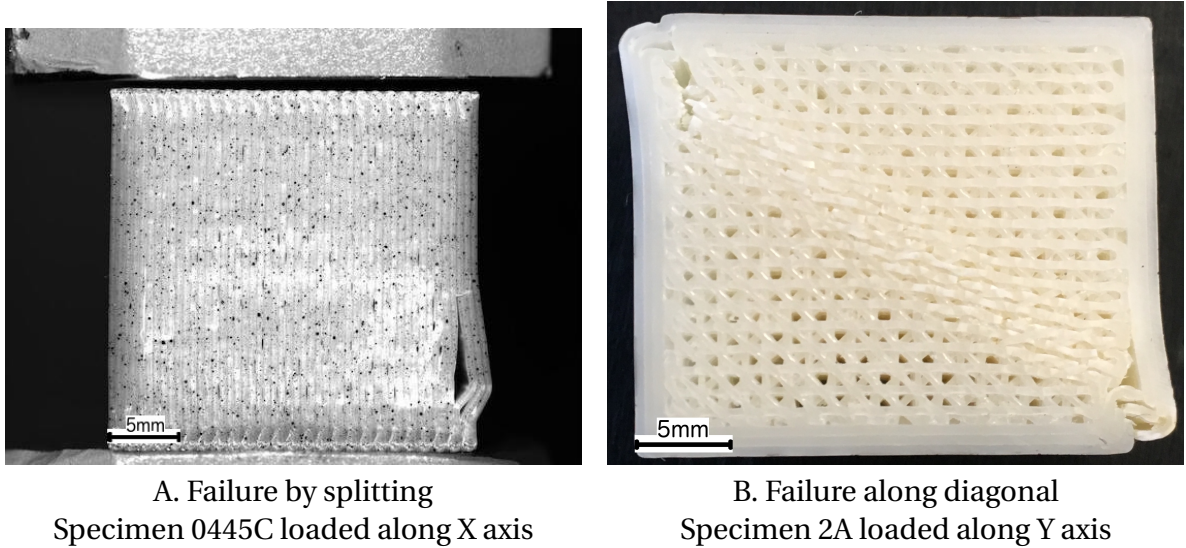
Figure 4.21

The crack formed during the testing ran along the entire diagonal. Cracking occurred where the part was strained the most. Cracking along a diagonal was not sudden but occurred gradually. However, it appeared that the cracked filaments did not just crack once, but twice. This formed a rotated zone of filaments in between two zones that kept the original mesostructural form.
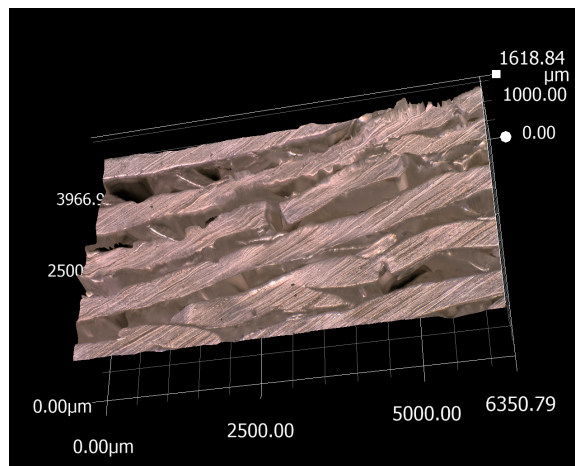
Figure 4.22. Micrograph of Cracking Failure

4.6 Understanding the Strain Distributions

A major concern in this project was the strain variation observed during the compression testing. In the following section, the terms horizontal and vertical are exclusively used to refer to the appearance of the strain map. Figure 4.23 shows the evolution of axial strain in specimen 0000E as it was loaded along the X axis of the FDM coordinate system. The strain map shows that there is strain variation in both the horizontal and vertical directions of the strain map. The horizontal top and bottom edges display the most compressive strain and no horizontal variations are observed. Between the top and bottom edges of the strain map, the strain varies with both the horizontal and vertical directions. The low strain region on the right edge has a radial distribution that forms a semi-circle.

Unlike the strain in the axial direction, the strain in the transverse direction is tensile. Therefore, the colors of the strain map are reversed and red represents the highest tensile strains. The resolved tensile strain follows a clear pattern as can be seen in figure 4.24 and the highest transverse strain is concentrated along the diagonals of the FDM specimen.

The strain maps, as produced by the FEM models, represent the strain variations in a continuum material. The test conditions were assumed to be the same in the FEM model and the real experiments. Therefore, the FEM strain maps should represent how a continuum material would have responded during the compression test. The FEM strain maps in figure 4.25 show that the top and bottom edges strained the most. Additionally, there were no observable horizontal strain variations across the top and bottom edges. Between the top and bottom edges, the strain is concentrated along the vertical

A. 0s (unloaded)

B. 294s (loaded)

C. 384s (loaded)

D. 474s (loaded)

E. 564s (loaded)

F. 942s (unloaded)
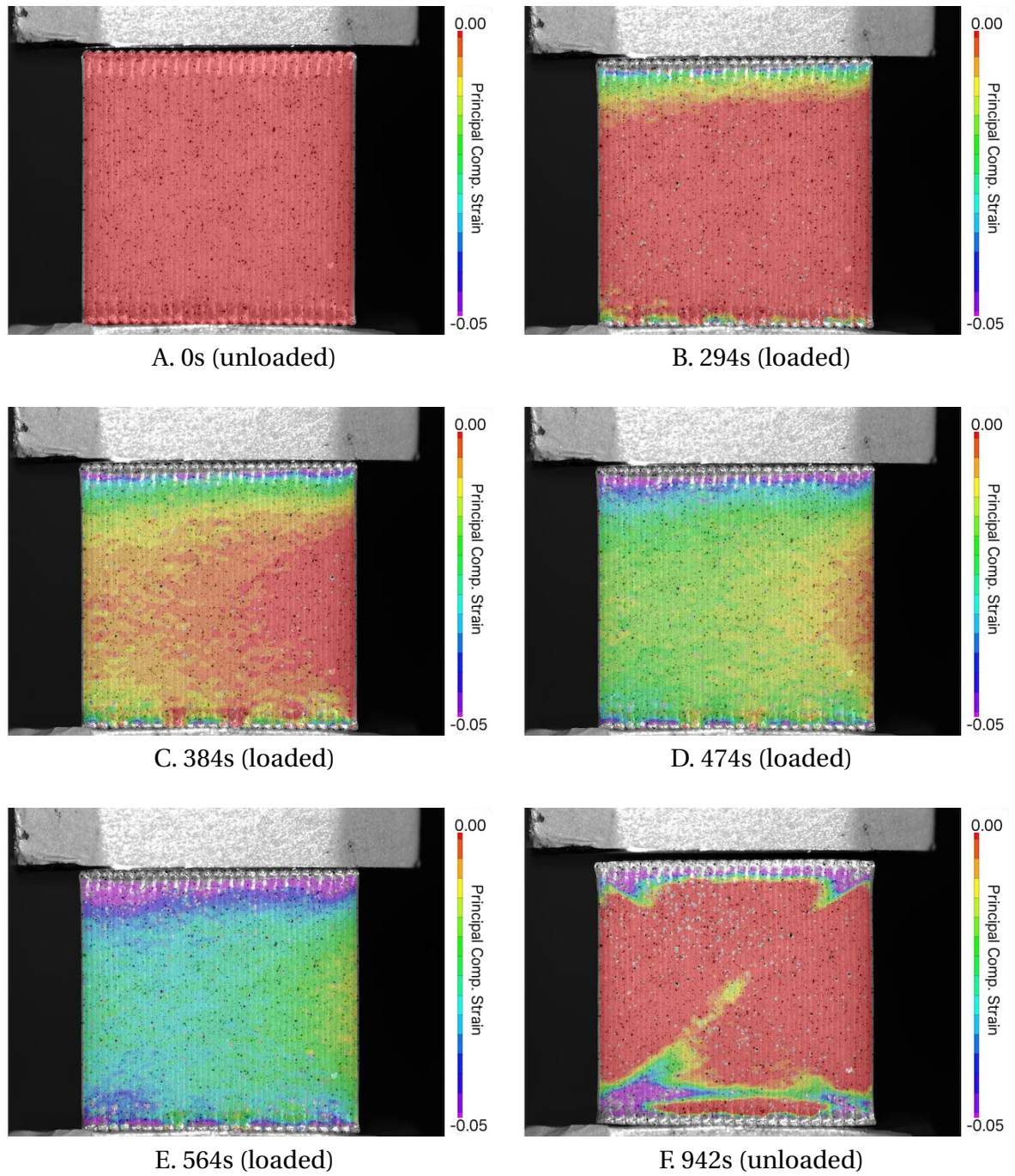
Figure 4.23. Axial DIC strain maps show the evolution of strain over time. The specimen is 0000E and it was loaded along the X axis

A. 0s (unloaded)

B. 324s (loaded)

C. 492s (loaded)

D. 654s (loaded)

E. 780s (loaded)

F. 828s (loaded)

G. 918s (loaded)

H. 942s (unloaded)
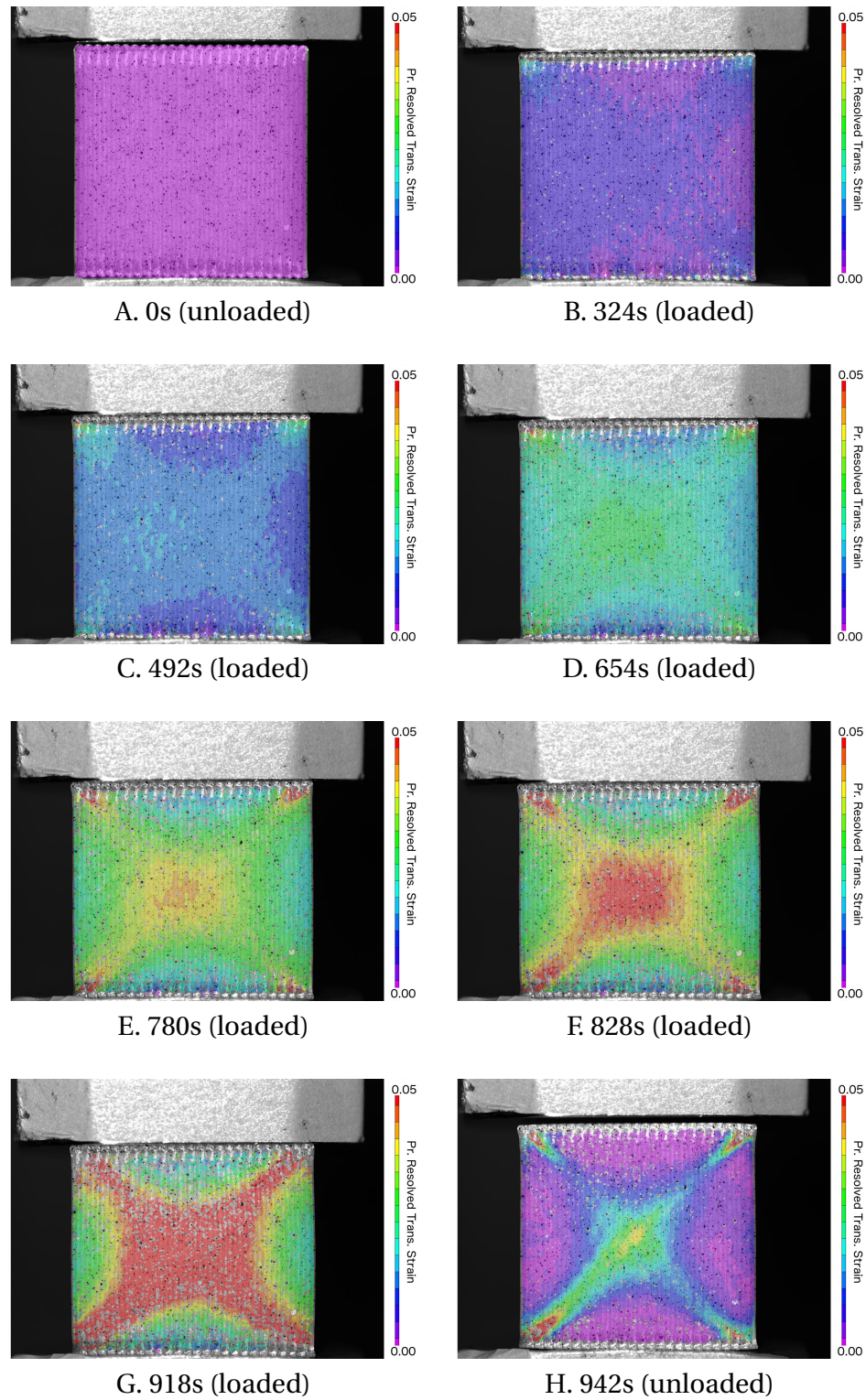
Figure 4.24. Transverse DIC strain maps show the evolution of resolved tensile strain in the FDM specimen. The specimen is 0000E and it was loaded along the X axis

center of the specimen. The strain is lower on the right and left edges than in the vertical center. The strain variations at the left and right edges have a radial distribution that forms semi-circles.

A. 0s (unloaded)

B. 160s (loaded)

C. 280s (loaded)

D. 390s (loaded)

E. 490s (loaded)

F. 550s (loaded)
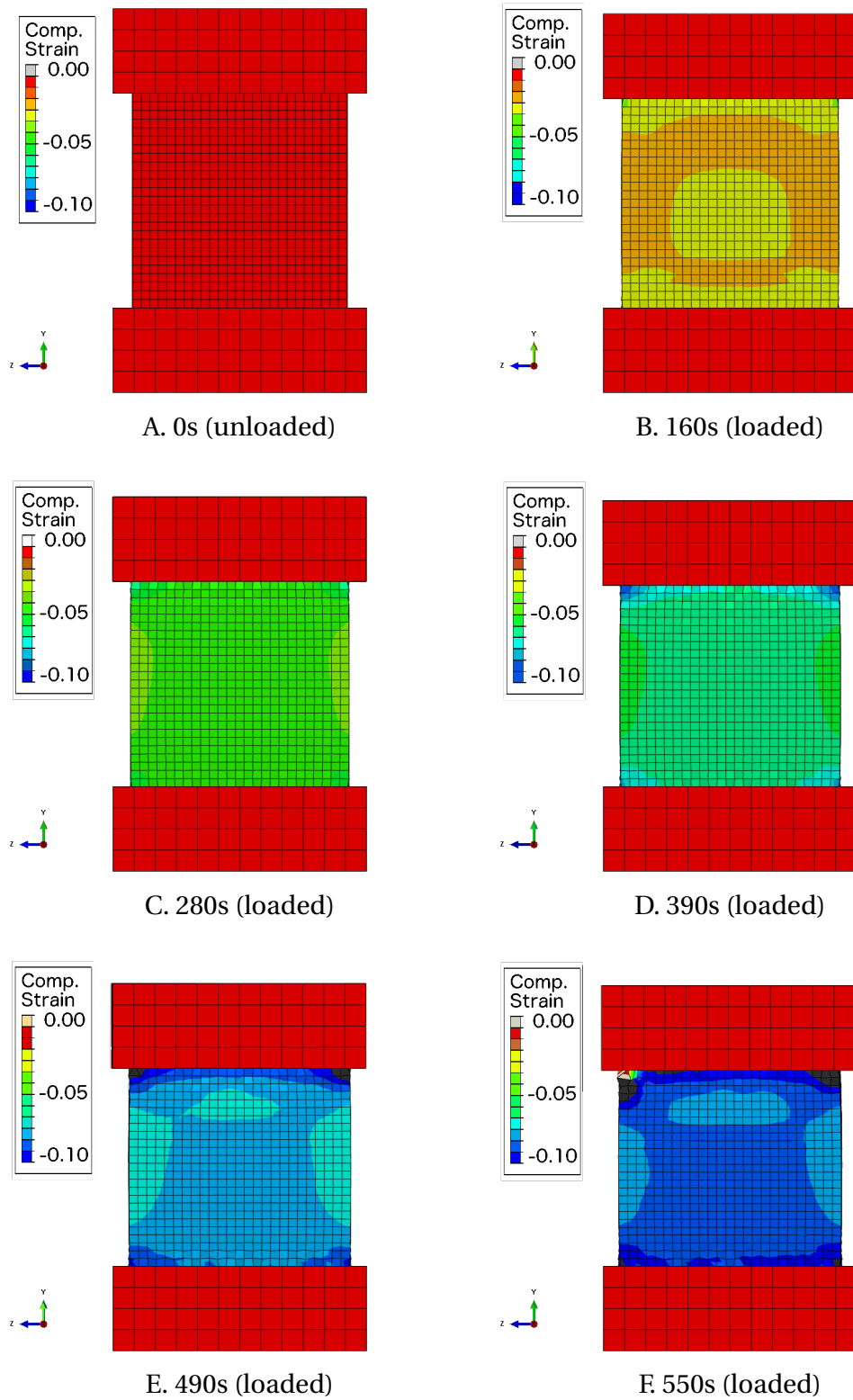
Figure 4.25. FEM strain maps show the evolution of strain over time

5 Discussion

The purpose of the discussion is to develop the comparison between the model and experimental results. The comparison is used to derive meaning about the FDM process and performance. Additionally, issues and problems from the project are brought up for the purpose of being thorough and exploring potential improvements.

5.1 Issues in Characterizing Mechanical Behavior of FDM Materials

5.1.1 Continuum Issues and Test Conditions

Since the goal was to obtain an elastic modulus, it was desirable to convert the DIC strain maps into stress-strain curves. This was only possible if the FDM part could be treated as a continuum material. When observing the mechanical behavior of FDM parts, a concerning matter was that the strain maps showed strain patterns with diagonal concentrations of strain. It was unknown if these strain variations would occur in continuum materials. As shown in figure 4.25, using FEM modeling identified that frictional constraints introduced during the compression testing were largely contributing to these strain patterns. The FEM strain maps also closely resembled the experimental strain

maps shown in figure 4.23. Both have concentrations of strain at the top and bottom edges. Also, the strain pattern on the right edge in both FEM and experimental is semi-circle shaped. In figure 4.23 E, the strain also appears to be concentrated along the vertical middle of the part. Therefore, the real data could be even closer to the FEM model if it was shifted to the right. Some real test conditions might have caused this shift to left, but were not captured in the FEM model conditions.

In addition to FEM, DIC analysis allowed us to analyze the validity of treating FDM parts as a continuum. As shown in figure 4.6, by changing the subset size and still measuring the same average strain, the DIC analysis showed that smaller subsets were representative of larger subsets. Therefore, the macroscopic part can be treated as a continuum of smaller volume elements.

5.1.2 Identifying the Linear Region

The stress-strain plots produced from compression testing of FDM specimens had a clear linear portion. The issue then became how to best calculate a modulus that represented the linearly elastic behavior of FDM parts. One method was to calculate a secant modulus. However, to calculate the secant modulus required a method for omitting the toe, which is the slope at the bottom of the stress-strain plot. The typical method as described in ASTM D695 for rigid polymers, is to find the point of inflection and treat everything before that as the toe. However, when testing, no spherical seating or high precision alignment tools were used. Therefore, the shape of the toe was very inconsistent and this inconsistency would be incorporated into the secant modulus measurement. A particular example of this inconsistency is the vertical toe that is observed in figure 5.1. This produces a modulus measurement greater than the bulk material and is

therefore assumed to be an artifact of the test. It also very different from the more commonly observed horizontal toe shown in figure 4.7. These large variations in the initial portion of the stress-strain curve would introduce errors into the final modulus measurement that would dominate the results. An alternative was to calculate the tangent modulus, which could be calculated at any point along the stress-strain plot and would avoid incorporating the toe. The tangent modulus would also be equal to the elastic modulus if it was calculated after the toe. Therefore, the tangent modulus was chosen as a precise measurement of mechanical response.

Identifying the start of the linear region was another challenge. Fortunately, the linear region always started at the same strain value. This was valid as long as the test setup was the same. This was noticed when the test setup was changed, including the compression platens, in order to accommodate the full-field lighting. It was noticed that the linear region started at different strains for the first test setup and for the second test
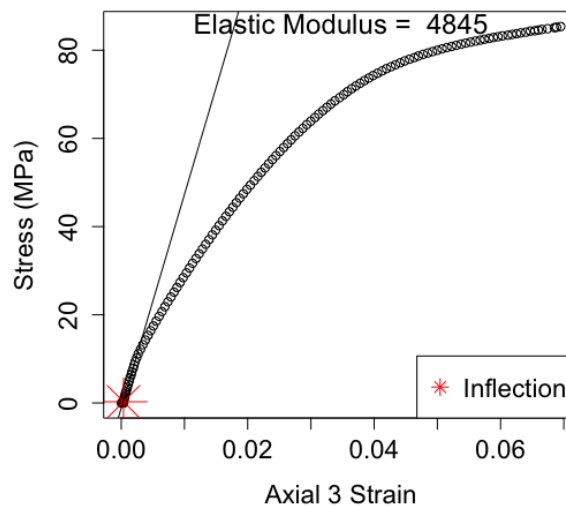
Figure 5.1. Stress-Strain Issues- Steep Slope: Seating and alignment issues can lead to anomalous results. The objective was finding where stress-strain data represented material behavior. In this image, the toe is vertical and therefore a point of inflection cannot be calculated.

setup. Therefore, it was likely that the toe was a function of the experimental setup and the start of linearity is when the specimen is loaded across the entire cross-sectional area.

5.2 Material Modeling

The material models in this project are based on the ideas of hierarchy and that structure determines properties. This leads to the idea that if nominal properties of an FDM mesostructure and the mesostructure of another FDM part are known, then the properties of the second mesostructure can be predicted. The nominal properties still need to be measured, but the structural data can be obtained from the CAD model used to define the FDM part. Defining the FDM part from the CAD model assumes that the filaments of the mesostructure are perfectly placed where the CAD model defined and that the process variables independently impact the structure.

5.2.1 Air Gap Volume Fraction

The volume fraction is fundamental to all of the models developed in this project. Two were developed: the air gap volume fraction and the raster angle volume fraction. The air gap volume fraction uses the idea that the filaments maintain the same shape and volume regardless of whether they are touching or spaced apart. Then, the ratio of filaments between different mesostructures can be determined from the width between filaments. The nominal mesostructure is defined as the structure with an air gap of 0mm and thus volume fraction is the ratio of the number of filaments in an arbitrary mesostructure to the nominal mesostructure. Additionally, the air gap volume fraction

model assumes that the error of filament placement in the real FDM part versus the CAD model is negligible.

When designing an FDM part in the Insight software, the software calculates the volume required to build that part directly from the CAD model. Interestingly, the software predicts that volume increases proportional to the raster angle[29]. This does not match the assumption that raster angle does not contribute to a change in volume of material used to print an FDM part. In figure 4.1, the experimental mass is compared to the mass model, which only depends on the air gap volume fraction and the addition of separate components. Since a constant density is assumed for filaments, a change in volume is directly related to a change in mass. A significant deviation from the mass model occurs at 0mm, when the raster angle is changed from 0° to 77°. This suggests that the raster angle does have an impact on the volume of the material printed. This implies that the air gap volume fraction, which accounts for the mass of material present in an FDM part, is not only a function of the air gap, but also raster angle. Interestingly, the effect of the raster angle on air gap volume fraction is inverse to the effect predicted by Insight software.The software predicted that volume of material used increases with raster angle, but the experimental results indicate the volume of material used is actually inversely proportional to the raster angle. However, this is only observed for specimens with an air gap of 0mm. For example, the change in mass due to raster angle is not observed at an air gap of 0.5mm. In fact, at this air gap, three different raster angles all produced FDM parts with similar masses as shown in figure 4.1. The study needs to be expanded to other air gaps to effectively capture the effect.

Since the air gap volume fraction was used in all models, it was essential to prove that it successfully worked. As shown in section 4.1, the mass model utilizing the volume fraction models was successful at predicting the density of the FDM cubes and demonstrates that the real mesostructure can be modeled directly from the CAD model and one real density measurement. This greatly reduces the amount of characterization work that has to be done since most of the information is contained directly in the CAD model. However, the 0mm case does indicate that the relationship is not perfect and that variations are present that differentiate the ideal CAD model with real FDM parts.

5.2.2 Stiffness Model Effectiveness

Besides predicting the mass, the stiffness model is very useful for application in FEM modeling of sheet metal forming processes. If the properties were known ahead of time, the amount of characterization and design trial and error can be reduced. This is how the model will improve the design of sheet metal forming tools made from FDM materials. The model is not perfectly accurate, but it does reveal important characteristics of FDM materials.

The stiffness model predicts properties at several length scales higher than the air gap volume fraction method. Important are the several different mesostructures present in the FDM part. The shell components have an air gap of 0mm and a raster angle of 0°, which is equal to the nominal mesostructure. These components do not change for the experiments and therefore do not contribute to a change in the model and the experimental results. The change in the tangent modulus observed in sections 4.4.1, 4.4.2, and 4.4.3, is due entirely to the fill. The mesostructure of the fill was changed by controlling the air gap and raster angle variables, which are represented on two of the

axes of the 3D plots. The change in mesostructure of the fill is what was used to evaluate the effectiveness of the model in predicting experimentally derived properties.

The stiffness model predicts that for a positive change in air gap, the tangent modulus will decrease according to a second order trend. This can be seen along the blue surface of the figures in section 4.4.1 or in the entire model shown in the figures of section 4.4.3. In all of the cases, the stiffness model over-predicted the tangent modulus. This implies that the tangent modulus is decreasing due to other factors. Although the causes in the X and Y directions were not proven in this project, a possible explanation for the Z axis model could be the layer interactions. For example, the 3D representation of the mesostructure in figure 5.2 shows that filaments that rotate over each other make less contact and therefore reduce the area, A_c, of load-bearing material. Another reason is that when there is a positive air gap and no raster angle, the filaments have to stack up directly on top of each other. Then, any small misalignment could lead to a moment that causes bending within the structure when a load is applied.

The raster angle volume fraction assumes that there is only one component that can be aligned in the direction of loading. If there are multiple sub-components, the volume fraction for aligned components is the inverse of the number of sub-components aligned with the loading direction. Therefore, the stiffness function predicts that with more unique orientations, there will be a significantly smaller amount of layers that can support the load. Therefore, the stiffness model predicts for a dramatic decrease with raster angle. Especially, small angles cause a big decrease in stiffness because they produce the most number of unique orientations. This can be seen throughout the space in the figures of sections 4.4.1 and 4.4.2. The raster angle region of the stiffness model under-predicted the tangent modulus with the assumption that layers not parallel to the
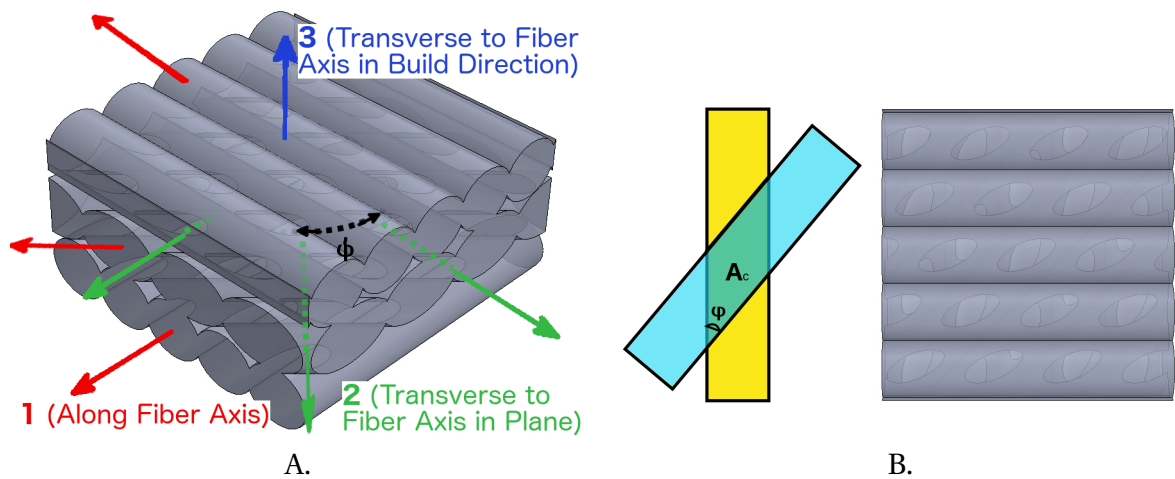
Figure 5.2. Mesostructure with 45° Raster Angle: The isometric view (A) demonstrated the different orientations of layers when a raster angle was introduced. The top view (B) showed the reduced area that joined two layers when a raster angle was introduced.

loading direction do not contribute to the model. This assumption is inaccurate for at least two reasons. One, since the filaments are rigidly adhered to the shells even when at an angle they would provide some stiffness. Additionally, layers at an angle build a grid with other layers and therefore contribute to the overall tangent modulus. This effect was not quantified in this project, but it must be present since the experimental data was stiffer than the model, which assumed these effects were negligible.

Another interesting case was the ability to add the tangent moduli of the shell and fill. This is most clearly highlighted when the model predicted a tangent modulus of 0MPa for the fill. Therefore, the only contribution came from the shell. The difference between the measured and predicted value was below 10% of the total tangent modulus. This indicated that the shell and fill could be considered to independently contribute to the tangent modulus.

5.2.3 Model Assumptions

All of the models made assumptions about the structure and behavior of FDM materials. In particular the structure was assumed to be ideal and unchanging. The properties of the filaments were assumed to stay constant and isotropic. The fusion zones between the filaments were neglected and filaments were assumed to have a uniform cross-section. Filaments made of different materials were assumed to have the same geometries and could be modeled with the same models developed for another material. Additionally, the CAD model was assumed to be an exact representation of the real FDM structure and filaments would be placed in the same location that the CAD model specified. The air gap volume fraction assumed that the only impact on the amount of mass in a material depended on the air gap process variable.

The raster angle volume fraction assumed that layers not in direct contact could be grouped into a single sub-component and have an impact on the stiffness equal to their mass relative to the rest of the layers. The raster angle volume fraction model also assumes that the layers not aligned with the direction of applied load are dead weight and do not contribute to stiffness in any way.

Finally, the homogenization and geometry model assumes that each component can be treated as a beam that interacts perfectly elastically with all other components. The geometry model assumes that the geometry from the CAD model perfectly represents the real geometry. All of the stress in the experimental data is also calculated with respect to the CAD model cross-sectional area definition.

5.2.4 Regression Analysis

In addition to comparing the experimental results with a model, a regression analysis was used to identify trends in the experimental data. When observing the experimental tangent moduli, the values seemed to follow the same trends regardless of material, as shown in section 4.4.4. This is a valuable observation because it means that any model only needs to be developed to account for changes in mesostructure. The nominal material properties can be incorporated in the mesostructure models to predict final properties.

The normalized plots, shown in figure 4.14, imply that the trends seen across all directions were in agreement with the trends predicted by the stiffness models. The regression analysis proved that the air gap has a significant impact on stiffness. Also it shows that the model was correct in predicting a positive trend between tangent modulus and raster angle. Although the trend is the same as the model, the regression analysis gave a much smaller weight to the raster angle and tangent modulus relationship. Therefore, if the air gap is positive, the raster angle will only slightly impact the the tangent modulus.

5.3 Damage

Cracking of the mesostructure is the dominant method for material to flow past itself in FDM materials. However, it was shown that there is certain non-recoverable strain immediately when the FDM part is loaded. This is most likely due to a more energy efficient packing of filaments being forced by the first compression. This plastic deformation was uniformly distributed across the FDM parts in cyclic plots, except for the

edges. However, the higher strain at the edges was attributed to the testing conditions, because they also showed up in the FEM model.

5.4 Application of the Results

Sheet metal forming was originally stated as the target for our project. Therefore, this section details how all the findings in this project can be used to design FDM tools for sheet metal forming applications. Sheet metal forming has a lot of costs associated with it, therefore cost reduction in FDM tool design and manufacturing is a prerogative. The FDM tool design process can be more efficient if computational models accurately predict the material properties and thus reducing the amount of costly (both in time on machines, and materials) experimental trial and error. However, if the capabilities of a tool are not known, then costly mistakes might be made. Also, if the capabilities are not known, it makes it harder to justify using the FDM tool for new applications.

6   Conclusions

This project developed a new hierarchical description of FDM materials that reduced the complexity of modeling all process variables and instead focused on treating the FDM part as an assembly of several mesostructures. The properties of each individual mesostructure were modeled using volume fraction approaches that relied on input directly from the CAD model used to design FDM parts. Defining the FDM part in terms of the CAD model reduces the amount of characterization needed to qualitatively predict its mechanical properties. Additionally, these models are the first step to developing stiffness models, which can accurately predict the properties of an FDM part. For sheet metal forming, accurately knowing the properties of FDM tools will reduce the costs associated with characterization or guessing the capabilities of an FDM tool.

A design of experiments was developed that covered the air gap and raster angle process variables, and a method for representing the mechanical response with a tangent modulus was developed. The methods for measuring the mechanical behavior of FDM parts were complicated by several test conditions, but these only served to reinforce the assumption that FDM parts can be modeled as continuum materials. The application of composite theory to the hierarchical structure of FDM materials indicates that the

smallest mesostructural feature of an FDM part, such as the layer fill, can be considered a representative volume elements. When these representative volume elements are added utilizing composite theory their combined properties represent that of the macroscopic FDM part.

The first model that was evaluated was the mass model, which is the most direct method of validating the air gap volume fraction model. It was accurate and proved that the CAD model can be used to model the real FDM part. This gives us confidence that any change in stiffness due to volume fraction will be accurately captured in the stiffness models. However, the assumption that the CAD model is a perfect representation of the FDM part was found to be false, since there were unexpected results in the mass model.

When used in the tangent modulus model, the volume fraction method consistently over-predicted the tangent modulus. This meant that the tangent modulus was negatively impacted by more than just volume. The tangent modulus also consistently under-predicted the tangent modulus at positive raster angles. This was because the impact of layers not oriented in the direction of loading were neglected in the model. However, from the experimental comparison to the model, it is clear that the layers do contribute to the overall tangent modulus. Additionally, a regression analysis proved that the relationships between the CAD model and the tangent modulus predicted by the theoretical model were correct. However, the regression analysis weighted the impact of the CAD model variables lower than the theoretical model.

Another aspect of the tangent modulus model, was to consider the fill and shell mesostructures as independent components. Each of these components had an effect

on the tangent modulus equivalent to its geometric proportion. This was not exhaustively validated in this project. However, the tangent modulus of several differently oriented shell mesostructure combined was validated. This proved that the macroscale FDM part can be considered a combination of multiple components and gave confidence in the developed methods.

Lastly, cyclic damage as well as fracture were qualitatively evaluated. When loaded elastically, the FDM part was shown to accumulate some plastic strain on the first cycle and then be perfectly elastic when loaded to the same stress on subsequent cycles. Additionally, fracture of an FDM part was shown to only occur locally. Typically, fracture occurred along the diagonal, which was due to testing conditions. This split the FDM part along a single localized shear band at 45 degrees to the loading direction. This resulted in most of the cube remaining undamaged as plastic deformation localized in the shear band.

Additionally, the findings in this project can be directly used to design FDM parts. For instance, the stiffness decreases faster with air gap in the fill than the volume fraction. Therefore, a stiffer part could be built with the same amount of material by not including a fill.

7   Suggested Future Research

7.1   Model Improvements

The model as it stands right now is based on a lot of assumptions. Instead of assuming that the CAD model and real structure are perfectly linked, more work needs to be done to study the effect of various process variables on the volume fraction of FDM materials. In particular this could be studied by improving upon the mass model proposed in this project. In particular, specimens with a particular air gap, but different raster angles could be examined. Then, the mass to raster angle relationship could be used to develop a more accurate volume fraction model.

Additionally, the raster angle models assumed that layers not aligned with the loading direction do not contribute to stiffness, but this was disproved by the experimental data. The current model sets a lower bound for stiffness and more work is needed to evaluate the additional impacts from other layers. This work would be mostly theoretical and could use the experimental data obtained in this project.

More experimental data is needed to validate a more general approach to the homogenization model. The current model can combine fill and shell components, but it does not extend to multiple components of the same volume as the fill. This would

involve testing a larger FDM parts that has many different mesostructures. The experimental data for several mesostructures was obtained in this project and could be used to predict the properties of a larger FDM part.

Lastly, the model needs to be expanded to three dimensions. This involves defining a stiffness tensor. This will be important for additional FEM modeling, which will be used to determine performance of FDM tools in sheet metal forming operations.

7.2 FDM Design Improvements

For the set of process variables tested in this project, the stiffness of the fill is shown to drop much more significantly than the volume fraction implies. Therefore, the user is getting less stiffness for the amount of material they are paying for. To improve this requires developing a method of reducing the weaknesses in the structure that produce the lower stiffness. Additionally, this project showed that the FDM part can be considered an assembly of multiple components. Therefore, one way to build a stiffer part would be to separate the desired FDM part into several components and add several stiff components where they are needed and leave sparse builds everywhere else. This could improve the stiffness of the part over the raster fill and also cost less time to print than a fully dense FDM part.

This same effect could also be achieved by changing the rasters per toolpath process variable. The shell in this project kept the high stiffness even when it was only three filaments thick. Therefore, changing the rasters per toolpath to three would essentially create an FDM part composed of high stiffness shells. This could help eliminate the layer effects that were theorized to reduce the stiffness beyond the volume fraction prediction.

Therefore, the stiffness in the Z direction could be comparable to the higher stiffness predicted by the stiffness model. However, it is uncertain if this design will help improve properties in the X and Y directions.

7.3 FDM Tool Improvements

The eventual goal is to predict the performance of an FDM tool in sheet metal forming. A particular project would be to obtain sheet metal forming prediction software and then use a stiffness tensor to predict the performance of an FDM tool. Another project would then make and test actual FDM sheet metal forming tools and evaluate if the prediction was accurate. In addition to stiffness, wear and failure of the FDM tool could be examined in other projects.

7.4 General Improvements

Damage in FDM part occurs before the onset plastic deformation. Small damage to the FDM parts could be detectable with DIC and this would be an important area to focus on to determine the life time of FDM parts.

Also, the the compression test for FDM parts needs to be standardized. Considering that FDM parts are anisotropic, cubic specimens could be useful due to the utility of cubes discussed in section 3.3.4.

Appendix A

MetaData

1 Ultem

Date	Spec	Group	ϕ	g	Ax. Comp.	Trans.	Mass	E_{exp}	E_{theory}	$E_{fillexp}$	$E_{filltheory}$	Material	E_{norm}
170426	0000C	0000	0.00	0.00	1	2	18.80	2923.54	2822.26	2987.13	2845.00	Ultem	1.03
170426	0000D	0000	0.00	0.00	1	2	18.85	2861.14	2822.26	2899.38	2845.00	Ultem	1.01
170426	0000E	0000	0.00	0.00	1	2	18.81	2825.04	2822.26	2848.88	2845.00	Ultem	0.99
170426	0000F	0000	0.00	0.00	1	2	18.81	2767.26	2822.26	2768.44	2845.00	Ultem	0.97
170426	0400B	0400	0.00	1.02	1	2	10.27	955.63	1361.24	468.01	948.33	Ultem	0.34
170426	0400C	0400	0.00	1.02	1	2	10.25	903.58	1361.24	407.70	948.33	Ultem	0.32
170426	0400D	0400	0.00	1.02	1	2	10.25	939.53	1361.24	449.32	948.33	Ultem	0.33
170426	0400E	0400	0.00	1.02	1	2	10.26	941.55	1361.24	451.66	948.33	Ultem	0.33
170426	0445A	0445	45.00	1.02	1	2	10.29	940.29	754.96	450.20	237.08	Ultem	0.33
170426	0445B	0445	45.00	1.02	1	2	10.28	916.28	754.96	422.39	237.08	Ultem	0.32
170426	0445C	0445	45.00	1.02	1	2	10.29	941.28	754.96	451.36	237.08	Ultem	0.33
170426	0445D	0445	45.00	1.02	1	2	10.29	939.78	754.96	449.61	237.08	Ultem	0.33
170426	0445E	0445	45.00	1.02	1	2	10.29	879.16	754.96	379.50	237.08	Ultem	0.31
170427	0000G	0000	0.00	0.00	2	3	18.85	2989.89	2684.32	3093.25	2666.00	Ultem	1.12
170427	0000H	0000	0.00	0.00	2	3	18.79	2483.66	2684.32	2392.64	2666.00	Ultem	0.93
170427	0000I	0000	0.00	0.00	2	3	18.84	2452.72	2684.32	2350.98	2666.00	Ultem	0.92
170427	0000J	0000	0.00	0.00	2	3	18.83	2997.30	2684.32	3103.78	2666.00	Ultem	1.12
170427	0000K	0000	0.00	0.00	2	3	18.84	2407.37	2684.32	2290.16	2666.00	Ultem	0.90
170427	0400F	0400	0.00	1.02	2	3	10.24	515.19	534.03	-21.03	0.00	Ultem	0.19
170427	0400I	0400	0.00	1.02	2	3	10.27	471.19	534.03	-69.98	0.00	Ultem	0.18
170427	0400J	0400	0.00	1.02	2	3	10.24	477.57	534.03	-62.89	0.00	Ultem	0.18
170427	0445F	0445	45.00	1.02	2	3	10.28	843.05	744.24	350.13	237.08	Ultem	0.32
170427	0445G	0445	45.00	1.02	2	3	10.29	925.48	744.24	445.24	237.08	Ultem	0.35
170427	0445I	0445	45.00	1.02	2	3	10.29	838.61	744.24	345.02	237.08	Ultem	0.31
170427	0445J	0445	45.00	1.02	2	3	10.29	878.82	744.24	391.31	237.08	Ultem	0.33
170428	0000L	0000	0.00	0.00	3	1	18.81	2295.52	2290.00	2297.59	2290.00	Ultem	1.00
170428	0000M	0000	0.00	0.00	3	1	18.84	2273.16	2290.00	2266.87	2290.00	Ultem	0.99
170428	0000N	0000	0.00	0.00	3	1	18.82	2334.22	2290.00	2350.82	2290.00	Ultem	1.02
170428	0000O	0000	0.00	0.00	3	1	18.85	2255.56	2290.00	2242.73	2290.00	Ultem	0.98
170428	0400K	0400	0.00	1.02	3	1	10.25	872.02	1143.16	416.12	763.33	Ultem	0.38
170428	0400L	0400	0.00	1.02	3	1	10.28	868.05	1143.16	411.07	763.33	Ultem	0.38
170428	0400M	0400	0.00	1.02	3	1	10.28	833.21	1143.16	366.83	763.33	Ultem	0.36
170428	0400N	0400	0.00	1.02	3	1	10.28	837.51	1143.16	372.28	763.33	Ultem	0.37
170428	0400O	0400	0.00	1.02	3	1	10.25	844.34	1143.16	380.96	763.33	Ultem	0.37
170428	0445K	0445	45.00	1.02	3	1	10.29	701.51	1143.16	200.33	763.33	Ultem	0.31
170428	0445L	0445	45.00	1.02	3	1	10.29	669.99	1143.16	160.66	763.33	Ultem	0.29
170428	0445M	0445	45.00	1.02	3	1	10.28	675.58	1143.16	167.69	763.33	Ultem	0.30
170428	0445N	0445	45.00	1.02	3	1	10.29	686.17	1143.16	181.03	763.33	Ultem	0.30
170428	0445O	0445	45.00	1.02	3	1	10.29	676.92	1143.16	169.38	763.33	Ultem	0.30
170501	0000P	0000	0.00	0.00	1	2	18.84	2862.55	2822.26	2901.36	2845.00	Ultem	1.01
170501	0445P	0445	45.00	1.02	1	2	10.28	950.13	754.96	461.62	237.08	Ultem	0.33

2 ABS

Date	Spec	Group	ϕ	g	Ax. Comp.	Trans.	Mass	E_{exp}	E_{theory}	$E_{fillexp}$	$E_{filltheory}$	Material	E_{norm}
161115	1A	1	76.82	1.02	3	1		540.17	972.93	98.98	649.67	ABS	0.28
161115	1B	1	76.82	1.02	1	2		819.12	665.40	474.61	297.32	ABS	0.39
161115	1B	1	76.82	1.02	2	3		737.40	674.93	369.07	297.32	ABS	0.33
161115	2A	2	45.00	0.51	2	3		902.75	643.37	561.44	261.25	ABS	0.40
161115	2B	2	45.00	0.51	1	2	10.15	936.63	633.80	612.21	261.25	ABS	0.45
161115	2B	2	45.00	0.51	3	1	10.15	671.33	1222.75	264.30	974.50	ABS	0.34
161116	3A	3	13.18	1.02	2	3	8.70	709.46	457.18	336.92	51.01	ABS	0.32
161116	3B	3	13.18	1.02	1	2	8.67	708.60	447.41	346.84	51.01	ABS	0.34
161116	3B	3	13.18	1.02	3	1	8.67	530.10	972.93	86.35	649.67	ABS	0.27
161116	4A	4	13.18	0.00	2	3		1415.50	548.01	1181.31	153.03	ABS	0.63
161116	4B	4	13.18	0.00	1	2	14.17	1534.29	538.34	1341.09	153.03	ABS	0.73
161116	4B	4	13.18	0.00	3	1	14.17	1433.84	1949.00	1253.04	1949.00	ABS	0.74
161116	5B	5	76.82	0.00	1	2	14.15	1598.79	1170.86	1422.79	891.97	ABS	0.76
161116	5B	5	76.82	0.00	3	1	14.15	1573.82	1949.00	1439.85	1949.00	ABS	0.81
161116	6A	6	45.00	1.27	2	3	8.25	741.28	544.69	373.55	149.29	ABS	0.33
161116	6B	6	45.00	1.27	1	2	8.27	742.11	535.01	385.42	149.29	ABS	0.36
161116	6B	6	45.00	1.27	3	1	8.27	519.98	900.82	73.65	556.86	ABS	0.27
161116	8A	8	0.00	0.51	2	3	10.14	428.96	411.42	19.52	0.00	ABS	0.19
161116	8B	8	0.00	0.51	1	2	10.03	729.81	1296.41	371.24	1045.00	ABS	0.35
161116	8B	8	0.00	0.51	3	1	10.03	824.94	1222.75	459.65	974.50	ABS	0.42
161116	9A	9	45.00	0.51	2	3		878.98	643.37	533.58	261.25	ABS	0.39
161116	9B	9	45.00	0.51	1	2	10.25	837.11	633.80	495.57	261.25	ABS	0.40
161116	9B	9	45.00	0.51	3	1	10.25	655.34	1222.75	244.07	974.50	ABS	0.34
170222	8E	8	0.00	0.51	2	3	9.89	429.61	411.42	20.25	0.00	ABS	0.19
170222	8H	8	0.00	0.51	3	1	9.91	721.77	1222.75	328.24	974.50	ABS	0.37
170224	9C	9	45.00	0.51	3	1	10.06	590.25	1222.75	161.95	974.50	ABS	0.30
170224	9D	9	45.00	0.51	3	1	10.02	567.55	1222.75	133.38	974.50	ABS	0.29
170224	9F	9	45.00	0.51	2	3	10.15	895.15	643.37	552.53	261.25	ABS	0.40
170224	9G	9	45.00	0.51	2	3	10.10	891.25	643.37	547.95	261.25	ABS	0.40
170224	9H	9	45.00	0.51	2	3	10.10	936.92	643.37	601.65	261.25	ABS	0.42
170224	9I	9	45.00	0.51	1	2	10.02	837.57	633.80	496.10	261.25	ABS	0.40
170224	SE	S	0.00	0.00	3	1	16.03	1928.44	1949.00	1920.77	1949.00	ABS	0.99
170224	SF	S	0.00	0.00	1	2	16.03	2025.56	2107.99	1979.23	2090.00	ABS	0.97
170224	SG	S	0.00	0.00	2	3	16.03	2250.93	2233.59	2273.79	2250.00	ABS	1.00
170224	SH	S	0.00	0.00	3	1	16.02	1970.38	1949.00	1978.39	1949.00	ABS	1.01
170224	SI	S	0.00	0.00	1	2	16.02	2156.43	2107.99	2155.61	2090.00	ABS	1.03

Appendix B

Preparation of this document

This document was prepared using pdfLaTeX and other open source tools. The (free) programs implemented are as follows:

- LaTeX implementation:

  MiKTeX

  http://www.miktex.org/

  TeXLive

  https://www.tug.org/texlive/

  MacTeX

  https://tug.org/mactex/

- Bibliographical:

  BibTeX

  http://www.bibtex.org/

  Zotero

  https://www.zotero.org/

Complete References

[1] L. Villalpando, H. Eiliat, and R.J. Urbanic. An Optimization Approach for Components Built by Fused Deposition Modeling with Parametric Internal Structures. *Procedia CIRP*, 17:800–805, 2014.

[2] Ismail Durgun. Sheet metal forming using FDM rapid prototype tool. *Rapid Prototyping Journal*, 21(4):412–422, June 2015.

[3] Hydroforming with FDM Tooling. Application Brief, Stratasys.

[4] L. Li, Q. Sun, C. Bellehumeur, and P. Gu. Composite Modeling and Analysis for Fabrication of FDM Prototypes with Locally Controlled Properties.pdf. *Journal of Manufacutring Processes*, 4(2):129–141, 2002.

[5] JosÃľ F. RodrÄśÌĄguez, James P. Thomas, and John E. Renaud. Design of Fused-Deposition ABS Components for Stiffness and Strength. *Journal of Mechanical Design*, 125(3):545, 2003.

[6] B. Huang and S. Singamneni. Raster angle mechanics in fused deposition modelling. *Journal of Composite Materials*, 49(3):363–383, February 2015.

[7] Xingchen Liu and Vadim Shapiro. Homogenization of material properties in additively manufactured structures. *Computer-Aided Design*, 78:71–82, September 2016.

[8] JosÃľ F. RodrÃŋguez, James P. Thomas, and John E. Renaud. Mechanical behavior of acrylonitrile butadiene styrene fused deposition materials modeling. *Rapid Prototyping Journal*, 9(4):219–230, October 2003.

[9] A. Bagsik, V. SchÃűppner, and E. Klemp. FDM part quality manufactured with Ultem* 9085. In *14th International Scientific Conference on Polymeric Materials*, volume 15, 2010.

[10] Taylan Altan and A. Erman Tekkaya. *Sheet metal forming: fundamentals*. ASM International, 2012.

[11] L. Fourment, J. L. Chenot, and K. Mocellin. Numerical Formulations and Algorithms for Solving Contact Problems in Metal Forming Simulation. *International Journal for Numerical Methods in Engineering*, 46:1435–1462, 1999.

[12] D. H. Mueller and H. Mueller. Experiences using rapid prototyping techniques to manufacture sheet metal forming tools. In *Proc. ISATA Conference, Dublin*, volume 9, 2000.

[13] Chil-Chyuan Kuo and Ming-Ren Li. Development of sheet metal forming dies with excellent mechanical properties using additive manufacturing and rapid tooling technologies. *The International Journal of Advanced Manufacturing Technology*, August 2016.

[14] Babapelumi Ebun Ayodele. *Modeling of FDM 3D Printing for Improved Performance*. Master of Science Thesis, Texas A&M University, Kingsville, TX, August 2015.

[15] Gaurav Shah and Arpan Shah. Investigation of the Effect of Fused Deposition Process Parameter on Compressive Strength and Roughness Properties of Abs-M30 Material. 2016.

[16] J. P. Thomas and J. F. RodrÃŋguez. Modeling the Fracture Strength Between Fused-Deposition Extruded Roads. In *Proceedings of the 11th Solid Freeform Fabrication Symposium*, pages 16–23, 2000.

[17] J. F. Rodriguez, J. P. Thomas, and J. E. Renaud. Maximizing the strength of fused-deposition ABS plastic parts. In *Proc. Solid Freeform Fabrication Symposium, Austin, TX*, pages 335–42, 1999.

[18] Brian Graybill. *Development of a Predictive Model for the Design of Parts Fabricated by Fused Deposition Modeling*. Master's Thesis, University of Missouri-Columbia, May 2010.

[19] S.F. Costa, F.M. Duarte, and J.A. Covas. Estimation of filament temperature and adhesion development in fused deposition techniques. *Journal of Materials Processing Technology*, 245:167–179, July 2017.

[20] FDM Best Practice: Creating Variable Density Parts.

[21] G. R Liu and S. S Quek. *The finite element method: a practical course*. 2014. OCLC: 962031770.

[22] Zhong-Yi Cai, Shao-Hui Wang, Xu-Dong Xu, and Ming-Zhe Li. Numerical simulation for the multi-point stretch forming process of sheet metal. *Journal of Materials Processing Technology*, 209(1):396–407, January 2009.

[23] Keith R. Symon. *Mechanics*. Addison-Wesley world student series edition. Addison-Wesley, Reading, Mass., 3. ed edition, 1980. OCLC: 256162382.

[24] Masud Chaichian, Ioan Merche§, and Anca Tureanu. *Mechanics: an intensive course*. Springer, Berlin, 2012. OCLC: 845976761.

[25] F. Baumgart. Stiffness- an unknown world of mechanical science? *Injury*, 31:14–84, May 2000.

[26] A. Sherif El-Gizawy, Shan Corl, and Brian Graybill. Process-induced properties of fdm products. *Proceedings of The ICMET*, 2011.

[27] W. Voigt. Ueber die Beziehung zwischen den beiden Elasticitãď'tsconstanten isotroper Kãűrper. *Annalen der Physik*, 274(12):573–587, 1889.

[28] A. Reuss. Berechnung der Flieã§grenze von Mischkristallen auf Grund der Plastizitãď'tsbedingung fãijr Einkristalle . *ZAMM - Zeitschrift fãijr Angewandte Mathematik und Mechanik*, 9(1):49–58, 1929.

[29] Manu Srivastava, Sachin Maheshwari, and TK Kundra. Experimental Evaluation of FDM Process for Model Material. *International Journal of Scientific & Engineering Research*, 5(11), November 2014.

[30] S. H. Masood, W. Rattanawong, and P. Iovenitti. Part Build Orientations Based on Volumetric Error in Fused Deposition Modelling. *The International Journal of Advanced Manufacturing Technology*, 16(3):162–168, February 2000.

[31] Josãľ F. Rodriguez Matas. *Modeling the mechanical behavior of fused deposition acrylonitrile-butadiene-styrene polymer components*. Doctoral Dissertation, University of Notre Dame, July 1999.

[32] H. Li, G. Taylor, V. Bheemreddy, O. Iyibilgin, M. Leu, and K. Chandrashekhara. Modeling and characterization of fused deposition modeling tooling for vacuum assisted resin transfer molding process. *Additive Manufacturing*, 7:64–72, July 2015.

[33] Nur Saaidah Abu Bakar, Mohd Rizal Alkahari, and Hambali Boejang. Analysis on fused deposition modelling performance. *Journal of Zhejiang University-SCIENCE A*, 11(12):972–977, December 2010.

[34] Luis Fernando Villalpando Rosas. *Characterization of Parametric Internal Structures for Components Built by Fused Deposition Modeling*. Master's Thesis, University of Windsor, 2013.

[35] Kshitiz Upadhyay, Ravi Dwivedi, and Ankur Kumar Singh. Determination and Comparison of the Anisotropic Strengths of Fused Deposition Modeling P400 ABS. In David Ian Wimpenny, Pulak M. Pandey, and L. Jyothish Kumar, editors, *Advances in 3D Printing & Additive Manufacturing Technologies*, pages 9–28. Springer Singapore, Singapore, 2017. DOI: 10.1007/978-981-10-0812-2_2.

[36] C.S. Lee, S.G. Kim, H.J. Kim, and S.H. Ahn. Measurement of anisotropic compressive strength of rapid prototyping parts. *Journal of Materials Processing Technology*, 187-188:627–630, June 2007.

[37] Miquel Domingo-Espin, Josep M. Puigoriol-Forcada, Andres-Amador Garcia-Granada, Jordi LlumÃă, Salvador Borros, and Guillermo Reyes. Mechanical property characterization and simulation of fused deposition modeling Polycarbonate parts. *Materials & Design*, 83:670–677, October 2015.

[38] Behzad Rankouhi, Sina Javadpour, Fereidoon Delfanian, and Todd Letcher. Failure Analysis and Mechanical Characterization of 3d Printed ABS With Respect to Layer Thickness and Orientation. *Journal of Failure Analysis and Prevention*, 16(3):467–481, June 2016.

[39] Farzad Rayegani and Godfrey C. Onwubolu. Fused deposition modelling (FDM) process parameter prediction and optimization using group method for data handling (GMDH) and differential evolution (DE). *The International Journal of Advanced Manufacturing Technology*, 73(1-4):509–519, July 2014.

[40] Michael Dawoud, Iman Taha, and Samy J. Ebeid. Mechanical behaviour of ABS: An experimental study using FDM and injection moulding techniques. *Journal of Manufacturing Processes*, 21:39–45, January 2016.

[41] Anoop Kumar Sood, R.K. Ohdar, and S.S. Mahapatra. Parametric appraisal of mechanical property of fused deposition modelling processed parts. *Materials & Design*, 31(1):287–295, January 2010.

[42] Vedansh Chaturvedi. *Parametric Optimization of Fused Deposition Modeling using Response Surface Methodology*. PhD thesis, National Institute of Technology Rourkela, 2009.

[43] V. Vijayaraghavan, A. Garg, Jasmine Siu Lee Lam, B. Panda, and S. S. Mahapatra. Process characterisation of 3d-printed FDM components using improved evolutionary computational approach. *The International Journal of Advanced Manufacturing Technology*, 78(5-8):781–793, May 2015.

[44] L.M. Galantucci, F. Lavecchia, and G. Percoco. Study of compression properties of topologically optimized FDM made structured parts. *CIRP Annals - Manufacturing Technology*, 57(1):243–246, 2008.

[45] Antonio Lanzotti, Marzio Grasso, Gabriele Staiano, and Massimo Martorelli. The impact of process parameters on mechanical properties of parts fabricated in PLA with an open-source 3-D printer. *Rapid Prototyping Journal*, 21(5):604–617, August 2015.

[46] Standard Test Method for Tensile Properties of Plastics. Technical report, ASTM International, 2014.

[47] Standard Test Method for Tensile Properties of Polymer Matrix Composite Materials. Technical report, ASTM International, 2014.

[48] Standard Test Method for Compressive Properties of Rigid Plastics. Technical report, ASTM International, 2015.

[49] Petrina C. Potts, Li Ma, Stephen M. Graham, and Matthew A. Adler. Repeatability and reproducibility of compression strength measurements conducted according to ASTM E9. Technical Report NIST TN 1679, National Institute of Standards and Technology, September 2009. DOI: 10.6028/NIST.TN.1679.

[50] Standard Test Methods of Compression Testing of Metallic Materials at Room Temperature. Technical report, ASTM International, 2009.

[51] Michael Albert Sutton, Jean-JosÃ' Orteu, and Hubert W. Schreier. *Image correlation for shape, motion and deformation measurements: basic concepts, theory and applications.* Springer, New York, N.Y, 2009. OCLC: ocn227916898.